


Spring August 2014

## OPTICAL AND SCANNING PROBE STUDIES OF ISOLATED POLY (3-HEXYLTHIOPHENE) NANOFIBERS

Mina Baghgarbostanabad  
*Physics*

Follow this and additional works at: [https://scholarworks.umass.edu/dissertations\\_2](https://scholarworks.umass.edu/dissertations_2)

 Part of the [Condensed Matter Physics Commons](#), [Optics Commons](#), and the [Physical Chemistry Commons](#)

---

### Recommended Citation

Baghgarbostanabad, Mina, "OPTICAL AND SCANNING PROBE STUDIES OF ISOLATED POLY (3-HEXYLTHIOPHENE) NANOFIBERS" (2014). *Doctoral Dissertations*. 51.  
<https://doi.org/10.7275/zgxp-5b07> [https://scholarworks.umass.edu/dissertations\\_2/51](https://scholarworks.umass.edu/dissertations_2/51)

This Open Access Dissertation is brought to you for free and open access by the Dissertations and Theses at ScholarWorks@UMass Amherst. It has been accepted for inclusion in Doctoral Dissertations by an authorized administrator of ScholarWorks@UMass Amherst. For more information, please contact [scholarworks@library.umass.edu](mailto:scholarworks@library.umass.edu).

OPTICAL AND SCANNING PROBE STUDIES OF ISOLATED  
POLY (3-HEXYLTHIOPHENE) NANOFIBERS

A Dissertation Presented

by

MINA BAGHGARBOSTANABAD

Submitted to the Graduate School of the  
University of Massachusetts Amherst in partial fulfillment  
of the requirements for the degree of

DOCTOR OF PHILOSOPHY

May 2014

Department of Physics

© Copyright by Mina Baghgarbostanabad 2014

All Rights Reserved

OPTICAL AND SCANNING PROBE STUDIES OF ISOLATED  
POLY (3-HEXYLTHIOPHENE) NANOFIBERS

A Dissertation Presented

by

MINA BAGHGARBOSTANABAD

Approved as to style and content by:

---

Michael D. Barnes, Chair

---

Mark Tuominen, Member

---

Anthony Dinsmore, Member

---

Todd Emrick, Member

---

Rory Miskimen, Department Head  
Department of Physics



## DEDICATION

To my family, and the love of my life.

## ACKNOWLEDGMENTS

I would like to acknowledge the support and friendship of the members of the Barnes group, without their help I would not have come this far. I would like to thank Austin J. Cyphersmith for teaching me the basics and getting me on my feet. I'd like to thank Joelle A. Labastide for her help and all the valuable scientific discussions that we have had together since I joined the group. Special thanks goes to my advisor Mike Barnes for the training, the encouragement, and the guidance over the past four years. His unwavering support has brought me to this stage in my career and life, and will propel me to the next stage.

I would like to thank our collaborators in the Emrick's group, the Hayward's group, and the DV's group for their expertise in synthesis of the materials explored in this work.

I'd like to thank my thesis committee, Profs. Dinsmore, Tuominen, and Emrick for their time and invaluable input over the course of my graduate career.

Great thanks go to my dear family for their vital support through my entire life.

## ABSTRACT

### OPTICAL AND SCANNING PROBE STUDIES OF ISOLATED POLY (3-HEXYLTHIOPHENE) NANOFIBERS

MAY 2014

MINA BAGHGARBOSTANABAD, B.S., AMIRKABIR UNIVERSITY OF  
TECHNOLOGY, TEHRAN, IRI

M.S., TEHRAN UNIVERSITY, TEHRAN, IRI

Ph.D., UNIVERSITY OF MASSACHUSETTS AMHERST

Directed by: Professor Michael D. Barnes

Plastic electronics have an essential role in the future technologies owing to their compelling characteristics such as light weight, biocompatibility, low cost fabrication, and tunable optoelectronic properties. However, the performance of polymer-based devices strongly depends on the efficiency of exciton formation and dynamics that are themselves strongly sensitive to polymer molecular packing and structural order. Therefore, the current challenge in achieving high efficiency is establishing a correlation between molecular packing and exciton coupling.

P3HT nanofibers represent an attractive platform for studying optical and electronic properties of exciton coupling because their nominal (highly crystalline) internal chain packing structure is known. A combination of wavelength-, time-, and polarization- resolved photoluminescence imaging on isolated nanofibers made of P3HT with varying molecular weight (from 10 to 65 kDa) has revealed a transition in dominant exciton coupling from primarily interchain (H-aggregation) for low molecular weight nanofibers, to predominantly intrachain (J- aggregation) coupling for high molecular weight nanofibers. Based on nanofiber width measurements from TEM imaging, the

driving force for this transition appears to be folding of individual polymer chains within the lamellae, resulting in enhanced chain planarity and reduced torsional disorder.

In addition, it is shown that mechanically and chemically robust functionalized poly-(3-hexylthiophene) (P3HT) nanofibers can be made via chemical cross-linking. Dramatically different photophysical properties are observed depending on the choice of functionalizing moiety and cross-linking strategy. It is shown by a variety of photophysical metrics that by controlling the size of the cross-linking agent relative to alkyl side chain length, exciton coupling in P3HT nanofibers can be controlled, either by including a relatively large linker, which reduces inter-chain coupling, or alternatively using a linker of comparable length to the lamellar spacing which minimally perturbs the aggregate structure.

KPFM measurements have revealed an interesting dependence of surface potential contrast (SPC) with P3HT nanostructure morphology. These results indicate that changes in the structural order are positively correlated with HOMO level energies in structures with effective one-dimensional excitonic coupling (high molecular weight regime), and are negatively correlated in effectively two-dimensional structures (low molecular weight regime). Moreover, it is recognized that the cross-linked aggregates show optical and electronic properties that are analogous to solvated chains because of their perturbed interchain coupling. We believe the results presented in this thesis provide new insights into polymer morphology “design rules” for optimizing OPV device performance.

# TABLE OF CONTENTS

	Page
ACKNOWLEDGMENTS .....	v
ABSTRACT .....	vi
LIST OF TABLES .....	x
LIST OF FIGURES .....	xi
CHAPTERS	
1- BACKGROUND .....	1
1-1 Conjugated polymer-based photonics .....	1
1-2 Fundamental excitation in organic polymers: Exciton .....	2
1-3 Polymer photophysics within the framework of H/J aggregates .....	4
1-3-1 Photophysics of isolated molecules vs. molecule assembly .....	5
1-3-2 Holstein- type aggregate Hamiltonian.....	7
1-4 Crystalline poly (3-hexylthiophene) nanofibers.....	15
2- OPTICAL PROBING AND TUNING TWO-DIMENSIONAL EXCITON	
COUPLING IN POLY(3-HEXYLTHIOPHENE) NANOSTRUCTURES .....	19
2-1 Physics of P3HT nanofibers within H/J- aggregate framework.....	21
2-1-1 Probing two-dimensional exciton coupling strength in P3HT nanofibers .....	22
2-1-2 Effective dimensionality of exciton in P3HT nanofibers.....	32
2-1-3 Conclusion: chain-folding effect on photophysics of P3HT nanofibers .....	36
2-2 Physics of P3HT nanoparticles within HJ-aggregate framework.....	38

3- CROSS-LINKED FUNCTIONALIZED POLY (3-HEXYLTHIOPHENE)	
NANOFIBERS WITH TUNABLE EXCITON COUPLING .....	44
3-1 Controlling cross- linking -induced structural perturbation in the cross -linked nanofiber via size of cross-linkage .....	45
3-2 Tailored exciton coupling in cross-linked functionalized P3HT nanofibers via solvent annealing .....	50
3-3 Conclusion .....	53
4- THE EFFECT OF POLYMET CHAIN CONFORMATION ON THE OPTOELECTRONIC PROPERTIES OF P3HT NANOSTRUCTURES: A KELVIN PROBE MICROSCOPY STUDY .....	55
4-1 Regioregularity and molecular weight effect on HOMO energy of P3HT .....	58
4-2 Correlation between P3HT chain conformation and HOMO energy level .....	62
4-3 Morphology-Dependent Surface Potentials in Cross-linked P3HT Nanostructures .....	66
4-5 Conclusion .....	69
5- NEAR FIRELD SCANNING OPTICAL MICROSCOPY & FUTURE WORK .....	72
REFERENCES .....	78

## LIST OF TABLES

Tables		Page
2-1	Polymer properties and lamellar thickness of different nanofiber families and proposed chain conformation for each family. Corrected MW values are calculated by applying multiplicative correction factor of 0.52 to the measured GPC value.....	30
2-2	PL Decay constants extracted from multiexponential fits of 13 kDa and 65 kDa PL decay dynamics shown in figure 2.12b.....	32

## LIST OF FIGURES

Figure	Page	
1-1	Schematic illustration of exciton energy levels with respect to conduction and valance bands. Exciton potential energy is less than the band gab and strongly depends on dielectric constant of the lattice.....	2
1-2	(a) Jablonski energy diagram illustrating electronic transitions between energy levels in an organic polymer. (b) Idealized wavelength resolved spectra of electronic transitions of a common conjugated polymer. Note that charge absorption spectrally overlaps with stimulated emission. (Reprinted from ref. 36)	3
1-3	(a) Absorption spectra of solvated P3HT chains and P3HT thin film with face-on structures (lamellae parallel to the substrate). (b) Chemical schematic of P3HT dimer presenting relevant intrachain (orange arrow) and interchain (green arrow) interactions.....	5
1-4	Diagrams for exciton band structure in molecular dimers with various geometrical arrangements of transition dipoles (Printed from ref. 20).....	6
1-5	(a) P3HT chain with five 3-hexylthiophene rings (unit cells) along with the ground state electronic configuration of each unit cells. (b) Ground state and three possible electronic configurations of each repeat unit cell. The associated nuclear potentials for vinyl stretching mode are also shown (Printed from ref. 22).....	7
1-6	Multiparticle basis set used to represent the $\widehat{H}_S$ Hamiltonian (Printed from ref. 22).....	9
1-7	Energy level structure of polymer aggregate in the strong EP coupling regime. The lowest energy exciton, $ J\rangle$ , occurs in the $v=0$ band which is capped by $ A_1\rangle$ exciton (Printed from ref. 26).....	11



1-8	Representative absorption and emission spectra in H- and J- aggregate. The 0-0 PL origin in H- aggregate is symmetry forbidden while it is the dominant radiative transition in J-aggregate (Printed from ref. 18).....	14
1-9	Chemical schematic (a) and energy diagram of frontier orbitals, HOMO and LUMO, (b) of Poly (3- hexylthiophene).....	15
1-10	Schematic of experimental system used for size correlated chemical microscopy. Multichannel emission path provides access to photoluminescence spectrum in energy, polarization, and time domain.....	18
2-1	Structural schematic of (a) P3HT nanoparticles and 3D P3HT/PCBM nanoparticle superlattice, and (b) nanofibers and 2D P3HT/CdSe nanorod composite via co-crystallization.....	19
2-2	Schematic illustration of (left) single P3HT chain in a good solvent (e.g., chloroform) and (right) self- assembly P3HT nanofiber in a marginal (e.g. toluene, or dichloromethane) solvent. The crystallographic axes are shown relative to nanofiber axes (Printed from ref. 56).....	21
2-3	Effect of solvent on dominant coupling in P3HT nanofibers. Lowering solvent quality enhances polymer chain planarity leading to stronger intrachain coupling as evidenced by an increase in the $A_{0,0}/A_{0,1}$ intensity ratio (Printed from ref. 58)...	22
2-4	PL (solid line) and absorption (solid dotted line) spectra of high MW P3HT nanofibers formed in anisole (A) and toluene (B) (Printed from ref. 53).....	23
2-5	(left) Temperature dependent photoluminescence emission origin ( $E_{0,0}$ ) and $I_{0,0} \setminus I_{1,0}$ PL intensity ratio of high molecular weight P3HT nanofibers. (Right) Schematic illustration of P3HT nanofiber packing modification as temperature and pressure increases (Printed from ref. 53).....	23

2-6	Representative photoluminescence images of nanofibers on cover glass made from (a) 13 kDa and (b) 65 kDa P3HT. Ensemble absorption spectra of suspended nanofibers in CF/DCM mixed solvent (c) and solid-state emission spectra of individual nanofibers (d) made from P3HT with a variety of molecular weights: 10 (black), 13 (red), 23 (yellow), 32 (green), 48 (blue), and 65 (purple) kDa. Arrows in panels c and d indicate changes in the spectral features as molecular weight is increased.....	24
2-7	Amorphous (dashed line) and crystalline (solid line) component of absorption spectra of corresponding P3HT nanofibers with various molecular weight shown in figure 2.6.....	25
2-8	(top) Free-exciton bandwidth (blue diamonds) and corresponding $I_{0-0}/I_{0-1}$ PL intensity ratios (red pentagon) from nanofibers of different P3HT molecular weights.....	26
2-9	(a) TEM image of single layer P3HT film along with schematic of its molecular packing. (Printed from ref. 64) (b) Schematic illustration of chain folding within the lamellae as molecular weight exceeds a critical value (Printed from ref. 56)...	28
2-10	Left: Representative TEM images of 10 kDa, 13 kDa, and 65 kDa P3HT nanofibers. Right: Normalized width histogram of P3HT nanofibers with high regiorigularity, and molecular weight ranging from 10 kDa to 65 kDa. Average nanofibers width is proportional to the contour length of low molecular weight polymers but level off at about 17 kDa when molecular weight exceeds 13 kDa due to chain folding above this critical molecular weight value.....	29
2-11	Molecular- weight-dependent nanofiber width (red squares) measured from TEM images and their corresponding polymer chains contour length (black circles). Chain contour lengths are calculated according to the corrected molecular weight (correction factor: 0.52). Molecular weight* is measured by GPC.....	30

2-12	(a) PL decay dynamics of P3HT nanofibers from different of molecular weight ranging from 10 kDa to 65 kDa. (b) PL decay dynamics of 13 and 65 kDa P3HT nanofibers that have strong H-aggregate and J-aggregate spectroscopic signatures, respectively, along with fits containing three exponentials. Measured instrument response is shown in filled gray.....	31
2-13	(a) Steady-state emission spectra of individual P3HT nanofibers: 13 kDa from CF/DCM (red circle), 65 kDa from CF/ DCM (purple circle), and 65 kDa from toluene (blue square). Black solid lines are model spectra consisting of a single progression of three Gaussians. Filled gray curve is the residual of the fitted model for 65 kDa NF from CF/DCM. (b) Emission polarization anisotropy of decay dynamics of corresponding P3HT nanofibers shown in (a). Positive M value corresponds to PL polarized along the chain backbone (transverse to nanofiber growth axis). (c) Graphic of P3HT nanofiber with 440 nm excitation polarization along c- axis and graphical illustration of PL polarization ellipse of exciton relative to c-axis vs. time. in nanofibers shown in (a) and (b).....	33
2-14	Schematic illustration of molecular weight-dependence of exciton effective dimensionality in P3HT nanofibers. In H-type nanofibers, 13 kDa with extended chain conformation, exciton expands in two dimensions while in J- type nanofibers, 65 kDa NFs with chain folded conformation, exciton is essentially one dimensional.....	36
2-15	(a) Photoluminescence image of individual P3HT nanoparticles. (b) and (c) height values and polarization contrast parameter of nanoparticles, respectively, overlaid on PL image. (d) Linear polarization anisotropy of single nanoparticle (solid black curve), along with the fit curve with and without exponential term (dotted red and solid red curves, respectively). (e) Scatter plot of modulation depth of nanoparticles shown in (a) vs. their height, and schematic illustration of internal structure of small and large nanoparticles.....	38
2-16	Measured absorption spectra of P3HT nanofibers in chloroform, chloroform/ toluene mixed solvent and toluene (top) and their corresponding amorphous and aggregate component (bottom).....	40

2-17	Free exciton bandwidth (blue) and crystal fraction (red) for different solvent compositions.....	42
2-18	Photoluminescence spectra of isolated nanofibers prepared from high- RR (98%) and low- RR (92%) P3HT under conditions of high- temperature (80°C) and low temperature (60°C).....	42
3-1	Structural schematic of diblock copolymer nanofiber, P3HT-b-P3ST cross-linked nanofiber, and P3HT-b-P3MT cross-linked nanofiber. The chemical drawing of corresponding diblock copolymers and cross-linkage are also represented.....	45
3-2	Absorption and emission spectra of 13kDa P3HT (red curves) and 15kDa diblock-copolymer P3HT-b-P3MT (black curves).....	46
3-3	Steady state absorption and emission spectra of (A) P3ST NFs and (B) P3MT NFs before (black) and after (red) cross-linking. Note the significant 40 nm blue-shift on the PL spectrum of the cross-linked P3MT nanofibers with respect to 0-0 origin of P3MT nanofibers despite their almost identical absorption spectra.....	47
3-4	PL Decay traces from 15 kDa P3ST (A) and P3MT (B) diblock-copolymer NFs before (black) and after (red) cross-linking. Note the disappearance of the fast decay component for the P3MT system after cross-linking.....	49
3-5	Transmission electron microscopy (TEM) images of different morphologies of cross-linked nanofibers: single cross- linked fibers, bundle of cross- linked fibers, and cross- linked sheets.....	51
3-6	Optical images of (a) P3HT –b-P3MT nanofibers in chloroform/dichloromethane mixed solvent and cross- linked P3HT-b-P3MT nanofibers in (b) mixed solvent and (c) The robust cross-linked hydroxyl nanofibers are not dissolved in chloroform and separate out onto the chloroform surface.....	51

3-7	(a) Solvent dependence on the room temperature emission spectra, and (b) PL decay dynamics of cross-linked P3MT nanofibers. PL spectra and decay curves from pre-cross-linked NFs are shown in black, post cross-linked suspended in 1:7 chloroform: dichloromethane (light red crosses), and chloroform (dark red triangles).....	52
4-1	Schematic illustration of kelvin probe force microscopy setup.....	56
4-2	Photoluminescence images of P3HT nanostructure cast from chloroform on cover glass with (a) 55% rra and 75 kDa MW, (d) 75% rr and 55 kDa MW, (g) 98% rr and 65 kDa MW, (j) 98% rr and 13 kDa MW. The corresponding topography (b, e, h, k) and surface potential (c, f, i, l) images of PL photos are shown on their right side.....	58
4-3	(a) PL spectra of P3HT nanostructures with different regioregularities and molecular weights: 55%rr and 75 kDa (black dashed line), 75% rr and 60 kDa (open black circles), 98% rr and 65 kDa (solid black line), and 98% rr and 13 kDa (solid red line). (b) The corresponding averaged measured surface potential of nanostructure in (a) as a function of regioregularity. The black and red squares denote the high and low molecular weights, respectively.....	60
4-4	Height and surface images of High molecular weight nanofibers (a,b) and low molecular weight nanofibers (c,d) cast on cover glass.....	63
4-5	Two- dimensional scatter plot of surface potential of low (a) and high (b) molecular weight P3HT nanofibers and nanowires and their height. In both graphs gray markers are drop-cast nanowires and colored markers are crystalline nanofibers. (c, d) The corresponding PL spectra of drop-cast nanofeatures and crystalline nanofibers with low and high molecular weights, respectively.....	64
4-6	Topography (a) and surface potential (b) images of cross-linked P3HT-b-P3MT nanofibers cast from CF/DCM representing various morphologies of cross-linked nanostructures such as fibers (F) and cloverleaf (CL) or sheets. (c) 2D Scatter plot showing the SP of cross-linked nanofibers (XNFs), cross-linked sheets (Xsheets) and 13 kDa P3HT nanofibers and their height.....	67

4-7	Surface potential and associated HOMO energy diagram of drop-cast nanowires (black squares), crystalline nanofibers (red diamond), and cross-linked nanostructures (brown diamond) as a function of molecular weight.....	69
5-1	Schematic drawing of an aperture near field scanning optical microscope. A typical microscope has an Al-Cr coated optical fiber with an aperture of 25 to 100 nm diameter at the point to generate a sub-wavelength light source used as the scanning probe. The probe will scan at a height of a few nanometers above the sample surface.....	73
5-2	Dual probe NSOM combined with upright and inverted optical microscope for multidimensional imaging in sub-wavelength scale.....	73
5-3	NSOM ansorption image and the corresponding spatially resolved transmission spectra from oligo thiophene film. The X-Y scale of the image shown in the inset is 6x6 $\mu m$ (Printed from ref. 112).....	74
5-4	(Left) surface height image of annealed P3HT thin film; (right) NSOM image of same region by confocal- detected Rayleigh scattering at 52 nm. The dips indicate absorption by crystalline domains.....	75
5-5	Left: 2D and 3D topography and optical images of P3HT nanofibers cast on glass. Right: (a) Line profile topography and corresponding backscattered signal of the line shown in 2D images. The dips in the NSOM trace correspond to the absorption by the fibrils. (b) Correlation plot of the P3HT nanofiber absorption versus their height.....	75

# CHAPTER 1

## BACKGROUND

### 1-1 Conjugated polymer-based photonics

Semiconducting polymers have been the subjects of great attention from numerous scientific researches for their usage as active layer materials in the next generation of electronics and advanced technologies. This interest is largely because their optical and physical properties can be tuned easily by manipulating polymer properties<sup>1</sup> including their substituent groups (e.g., side chain length, polymerization degree, end-function)<sup>2-5</sup>, as well as their low-cost fabrication, light weight, biocompatibility, flexibility, and ease of application over large surfaces through commercially-viable coating techniques.<sup>6-8</sup> The performance of semiconducting polymer based devices depends on the formation of electronic excited states (excitons).<sup>9</sup> In fact, optoelectronic performance of polymer aggregates is sensitive to the efficiency of exciton formation and dynamics that are themselves strongly sensitive to polymer molecular packing and structural order. Especially in polymer-based organic photovoltaics (OPVs), directional control over exciton migration within the active layer and efficient charge harvesting at the donor-acceptor interface represent important goals in achieving OPVs with improved power conversion efficiencies. Therefore, establishing a relationship between polymer molecular structure and optoelectronic properties through studying exciton coupling is essential in designing organic based electronic devices, and optimizing their optoelectronic properties and device efficiency.<sup>10, 11</sup> In this regard, spectroscopy of polymer aggregates provides a wealth of information about exciton formation, and dynamics including exciton migration, diffusion, dissociation, and recombination, and

offers insight into molecular packing within the investigated nanostructure. Accordingly, optical probing of organic assemblies is a primary step preceding device fabrication and characterization to optimize the polymer molecular packing for desired application.

## 1-2 Fundamental excitation in organic polymers: Exciton

The fundamental excitation in semiconductors is called an exciton- a bound state of electron and hole that are bound by coulomb potential energy  $-e^2/\epsilon r$ <sup>12</sup> where r is electron- hole distance and  $\epsilon$  is the appropriate dielectric constant (figure 1-1).<sup>12, 13</sup>

Dielectric constant of the lattice,  $\epsilon$ , indicates the screening effect of the background (e.g., neighboring atoms and existing free charges) on the potential energy of the exciton and plays an important role in determining its properties. In organic materials with typically small dielectric constant ( $\epsilon \approx 1.5 - 2$ ), the coulomb potential energy is strong and so electron and hole are tightly bounded and localized, giving rise to Frenkel-type excitons. The typical binding energy of Frenkel exciton is on the order of 0.1 to 1 eV and its radius (R), the electron- hole distance, is on the same order of unit cell.<sup>12</sup> On the other hand, excitons in inorganic semiconductors (for example CdSe) with large dielectric constant has a radius much larger than the interatomic distance and can extend over tens to

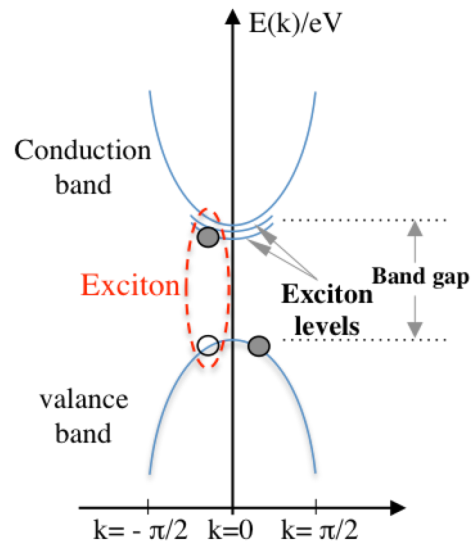


**Figure 1-1: Schematic illustration of exciton energy levels with respect to conduction and valance bands. Exciton potential energy is less than the band gab and strongly depends on dielectric constant of the lattice.**



hundreds of unit cells. This type of excitons is called Wannier- Mott excitons with binding energy of about 0.01 eV.<sup>14</sup>

The ground state of organic semiconductors is electrically neutral and has net spin zero. Molecules can be excited from the vibrationless ground state to the excited state in response to photon absorption and generate an exciton. As shown in Figure 1-2a, the fate of photogenerated excitons is influenced by a variety of different possible transitions.<sup>15</sup>

Excitonic states with net spin zero or one are referred as singlet (S) or triplet (T) states, respectively. Polaronic states referred as charge states (CS or D) are associated with the

free electrons in the excited states. The subscript

indicates series of states in each group; Upward pointing arrows show photon-induced excitations (e.g., ground-state

absorption), and gray wavy lines indicate non-radiative transitions that are accompanied by exciting

phonons or vibrational quanta. Downward pointing

arrows denote radiative relaxations, transitions that

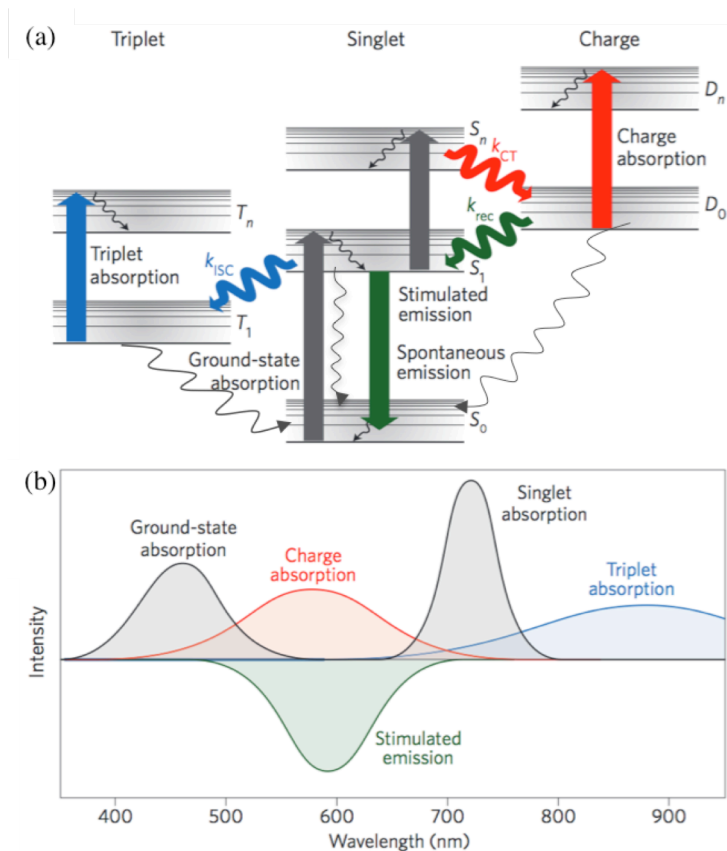


**Figure 1-2: (a) Jablonski energy diagram illustrating electronic transitions between energy levels in an organic polymer. (b) Idealized wavelength resolved spectra of electronic transitions of a common conjugated polymer. Note that charge absorption spectrally overlaps with stimulated emission. (Reprinted from ref. 36)**

occur from the bottom of the singlet-excited state ( $S_1$ ) to the ground state ( $S_0$ ) and are accompanied by photon generation. Population of triplet state with spin 1 by ground-state absorption is insignificant because electromagnetic radiation does not have any torque and therefore photons do not couple with the spin of electron. Therefore, triplet states can only be populated with low yield via intersystem crossing at a rate constant of  $K_{ISC}$ . The generated triplet-excitons either relax to the ground state via weak phosphorescence or excited to the higher triplet states via photon absorption that is referred as triplet absorption (blue arrow). In addition, hot excitons that are generated in the high-lying excited states ( $S_n$ ) by multiphoton transitions can give rise to either intra- or inter-chain charge separation<sup>16, 17</sup> with a charge-transfer rate constant  $K_{CT}$ , resulting in the formation of free charges. These free charges can recombine with rate constant  $K_{REC}$  to the singlet excited state, be photo-excited to the higher energy charge states, or nonradiatively decay to the ground states. Figure 1-2b shows the spectra of absorption and emission transitions typical of organic systems with associated energy ranges, also showing a large spectral overlap of charge absorption and stimulated emission.

### **1-3 Polymer photophysics within the framework of H/J aggregates**

In the molecule assembly two-dimensional exciton coupling leads to exciton diffusion along and across polymer chains. Exciton dynamic (e.g., migration, diffusion, dissociation, and recombination) in organic semiconductors is playing a key role in charge and energy transfer between conjugated segments. The efficiency of each process is strongly sensitive to the molecular packing and disorder of the system. Therefore the ability to tune exciton dynamics is an essential step in developing high-power organic optoelectronic devices.

### 1-3-1 Photophysics of isolated molecules vs. molecule assembly

In soft condensed matters, exciton formation is accompanied by nuclear relaxation that gives rise to coupling of dispersionless phonons to the electronic transitions. The exciton-phonon coupling through electron transition between ground state and the excited state,  $S_0 \rightarrow S_n$  or  $S_n \rightarrow S_0$ , is manifested as vibronic progression in both absorption and emission spectra; in many organic systems, the vibrational coordinate most strongly coupled to the electronic excitation is a vinyl stretch (e.g ring distortion) with typical energy of  $\approx 175$  meV ( $1450$  cm $^{-1}$ ).<sup>18</sup> The typical vibronic progression in the absorption and emission of isolated molecules has Poissonian distribution  $I_{0-\nu} \approx \lambda_0^{2\nu} \exp(-\lambda_0^2) / \nu!$ , where  $\lambda_0^2$  is electron-phonon coupling constant (also called Huang-Rhys factor) and  $\nu$  is the number of vibrational quanta coupled with electronic transition.<sup>19</sup>

This Vibronic progression is often distorted in close-packed molecular assemblies (figure 1-3a) due to competing interaction between molecules in aggregates along the polymer chain (intrachain coupling) and between neighboring chains (interchain

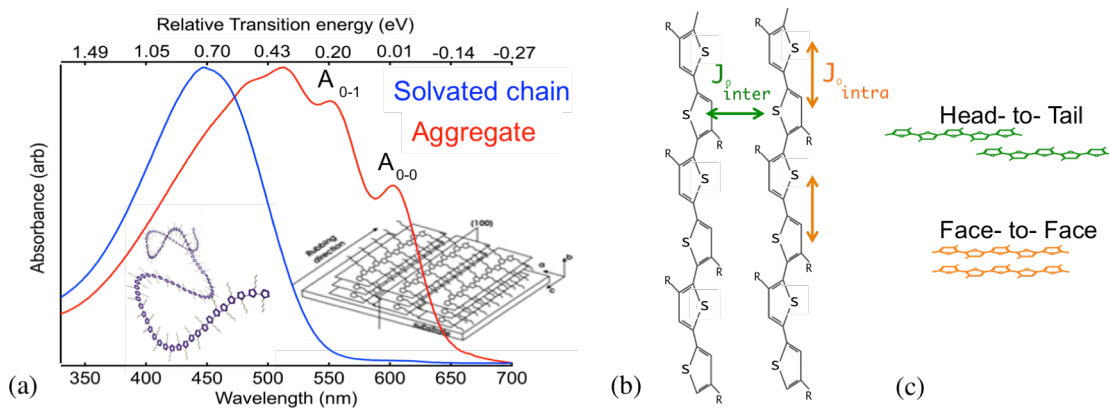


**Figure 1-3: (a) Absorption spectra of solvated P3HT chains and P3HT thin film with face-on structures (lamellae parallel to the substrate). (b) Chemical schematic of P3HT dimer presenting relevant intrachain (orange arrow) and interchain (green arrow) interactions.**

coupling) as was shown in figure 1-3b. Intrachain coupling promotes Wannier-Mott excitons, while interchain coupling promotes Frenkel excitons. Accordingly, photophysics of polymer aggregates takes into account exciton diffusion along and across polymer chains and does not follow Franck- Condon progression.

As illustrated in Figure 1-3c, the relative orientation of neighboring chains identifies two types of configurations: head-to-tail structures (J-aggregate) and face-to-face structures (H-aggregate) that favor intrachain and interchain couplings, respectively. Kasha's seminal study of the effect of aggregation on photoluminescence properties, from a purely electronic perspective, showed that side-by-side orientation of rod shape molecules results in blue-shifted absorption origin along with fluorescence quenching. In contrast, head-to-tail conformations lead to enhanced photoluminescence intensity and a spectral redshift. Figure 1-4 shows various geometrical arrangement of transition dipoles and their corresponding exciton band with allowed optical transitions.<sup>20</sup> Accordingly, the Franck-Condon vibronic progression characterizing absorption and emission spectra are affected differently by these two aggregate conformations. Hence, optical probe of

exciton dynamics and aggregate-induced deviation from Poissonian distribution of vibronic peak intensities will provide a wealth of information about the fundamental excitations

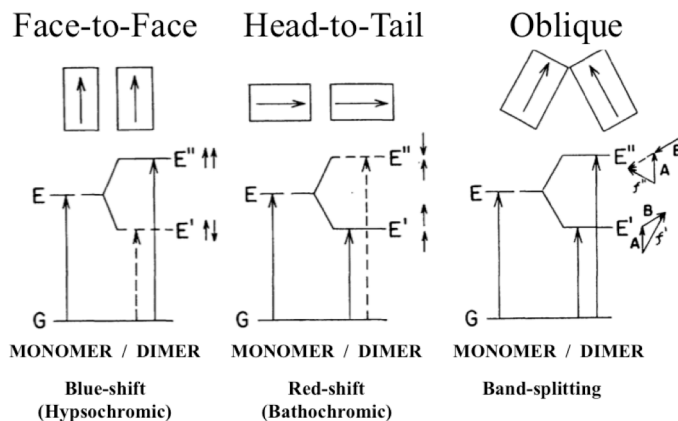


**Figure 1-4: Diagrams for exciton band structure in molecular dimers with various geometrical arrangements of transition dipoles (Printed from ref. 20).**

that are responsible for absorption and emission as well as molecular packing, structural order, the strength of exciton coupling with molecules, and the nature of disorder in the aggregates.<sup>21</sup> A detailed description of the theoretical framework used to describe exciton coupling in polymer aggregates is presented in the following section.

### 1-3-2 Holstein- type aggregate Hamiltonian

As it is depicted in figure 1-5a, each polymer chain in aggregate is presumed to contain N chromophores (unit cells, here thiophene rings) and is described as a one-dimensional semiconductor. Each unit cell in the vibronically excited state would contain either an electron/hole pair or a single charge giving rise to three possible excited electronic configurations ( $S_1$ ), as shown in figure 1-5b.<sup>22</sup> It is assumed that potential wells in both ground and excited states are harmonic with identical curvature.

The relative displacement of nuclear potential of vibronically excited unit cell ( $S_1$ ) with respect to its ground state ( $S_0$ ) is defined by Huang-Rhys factor ( $\lambda_0^2$ ).

The shifts in the nuclear potentials corresponding to cation ( $S_+$ ) and anion ( $S_-$ ) excitations are generally smaller, with the respective HR factors,  $\lambda_+^2$  and  $\lambda_-^2$ , typically less than  $\lambda_0^2$ .

As proposed by Spano, electronic excitations in organic

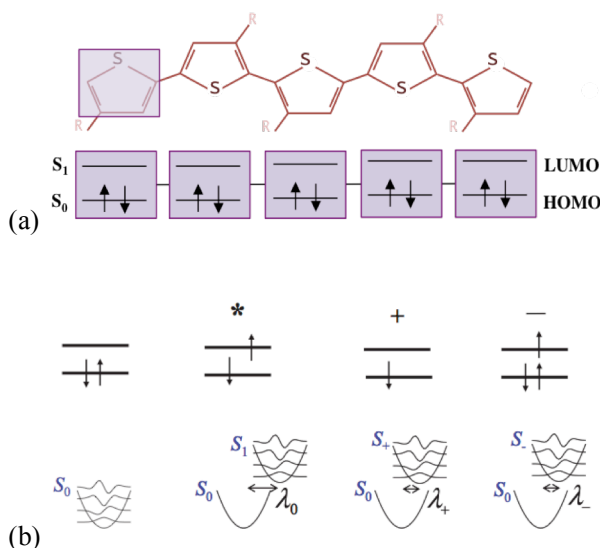


**Figure 1-5: (a) P3HT chain with five 3-hexylthiophene rings (unit cells) along with the ground state electronic configuration of each unit cell. (b) Ground state and three possible electronic configurations of each repeat unit cell. The associated nuclear potentials for vinyl stretching mode are also shown (Printed from ref. 22).**

polymers can be described as a vibronic excitation that is surrounded by a field of vibrational excitations.<sup>23</sup> These composite excitations are referred as Frenkel exciton polarons where polaron radius indicates spatial extent of vibrational distortion.

The Holstein-type Hamiltonian of the  $s^{\text{th}}$  chain in the aggregate has two components: electronic and vibrational components as represented, and reads<sup>24</sup>

$$\hat{H}_s = \hat{H}_{ele} + \hat{H}_{vib} \quad (1)$$

with

$$\hat{H}_{ele} = \varepsilon_e + \varepsilon_h + \sum_n (t_e c_n^+ c_{n+1} + t_h d_n^+ d_{n+1} + h.c.) + \sum_{n,r} V(r) c_n^+ c_n d_{n+r}^+ d_{n+r} \quad (2)$$

$$\hat{H}_{vib} = \hbar\omega_0 \sum_n b_n^+ b_n + \hbar\omega_0 \sum_n (\lambda_0 (b_n^+ + b_n) + \lambda_0^2) c_n^+ c_n d_n^+ d_n + \hbar\omega_0 \sum_{n,r \neq 0} (\lambda_- (b_n^+ + b_n) + \lambda_+ (b_{n+r}^+ + b_{n+r}) + \lambda_-^2 + \lambda_+^2) c_{n+r}^+ c_{n+r} d_{n+r}^+ d_{n+r} \quad (3)$$

Here, the subscript  $n$  denotes unit cell number in chain  $S$ . In the electronic part of the Hamiltonian,  $\varepsilon_e$  ( $\varepsilon_h$ ) is the energy of electron (hole) in the LUMOs (HOMOs);  $t_e$  ( $t_h$ ) is the transfer integral that connects LUMO (HOMO) orbitals of unit cells along the chain;  $c_n^+$  ( $d_n^+$ ) and  $c_n$  ( $d_n$ ) creates and annihilates electron (hole), respectively, in the LUMO (HOMO) level; and  $V(r)$  represents coulomb potential of e/h pair that are separated by  $r$  and is defined as

$$V(0) = -U \quad U > 0, \quad (4a)$$

$$V(r) = -\frac{V_1}{|r|} \quad V_1 > 0 \quad (4b)$$

Consequently, the required energy for creating an electron/hole pair in a unit cell is  $\varepsilon_e + \varepsilon_h - U$ , also  $U - V_1$  is the energy barrier for charge separation between neighboring unit cells.

The vibrational component of Hamiltonian originates from symmetric vinyl stretching mode with frequency  $\omega_0$ . Hence,  $\hbar\omega_0$  is the energy of symmetric vinyl stretching mode,  $\hbar\omega_0\lambda_0^2$  is nuclear relaxation energy, and  $\hbar\omega_0\lambda_0$  is exciton-phonon coupling energy. The

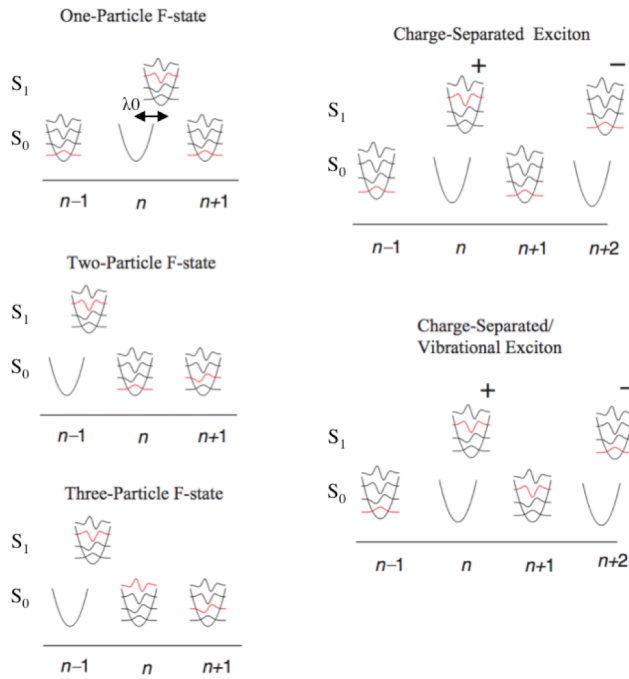


**Figure 1-6: Multiparticle basis set used to represent the  $\widehat{H}_s$  Hamiltonian (Printed from ref. 22).**

electron/hole pair or a single charge.

The  $\widehat{H}_s$  Hamiltonian is based on multiparticle states.<sup>25</sup> For the 1D semiconductor there are two basis types of excitations as depicted in figure 1-6:<sup>22</sup> Frenkel-like (F) excitation where the e/h pair is confined to a particular repeat unit, and charge-separated (CS) excitation in which the electron and hole reside on different repeat units. In the F-state a “particle” is defined to be the unit cell that is vibronically or purely vibrationally excited; For instance, one-particle excitation represents the simplest F-like excitation, when one unit cell is vibronically excited and the rest of unit cells are in the ground state with zero vibrational energy; whereas two-particle state is referred to be an excitation in which vibronic and vibrational excitons reside on two different unit cells.

$\widehat{H}_{vib}$  consists of three summation terms: the first term determines vibrational energy in the ground state where  $b_n^+$  ( $b_n^-$ ) creates (destroys) vibrational quantum in the ground state of nuclear potential well ( $S_0$ ); The last two summation terms account for vibrational energy in the excited state ( $S_1$ ) of unit cells that have either an

The  $\alpha^{\text{th}}$  eigenstate of the chain Hamiltonian can then be expanded in one- and two-particle states:<sup>26</sup>

$$|\psi^\alpha\rangle = \sum_{n(\nu)} c_{n(\nu)}^{(\alpha)} |n(\nu), s\rangle + \sum_{n(\nu)} \sum_{\hat{n}(\hat{\nu})} c_{\hat{n}(\hat{\nu})}^{(\alpha)} |n(\nu), s; \hat{n}(\hat{\nu}), s\rangle \quad (5)$$

Here,  $|n, s\rangle$  is F-like or CS-like excited state of  $n$ th unit cell in the  $S$ th chain and is represented as  $|n(\nu), s\rangle = c_{n,s}^+ d_{n,s}^+ |g\rangle \otimes b_{n,s}^{+\nu} |\nu\rangle$ , where  $|g\rangle$  denotes pure electronic ground state of  $S$ th chain and  $|\nu\rangle$  indicates vibrational state of the whole chain with all unit cells having zero vibrational quantum; and  $|n(\nu), s; \hat{n}(\hat{\nu}), s\rangle$  denotes two-particle excitation state.

A complete Hamiltonian is acquired by adding interaction Hamiltonian to the single chain Hamiltonian. Assuming that each chain efficiently interacts only with its two nearest neighbors, the complete Hamiltonian would be<sup>24</sup>

$$\hat{H}_{aggregate} = \hat{H}_s + \sum_{\acute{s}=s\pm 1} \sum_n J_{inter} (|n(\nu), \acute{s}\rangle \langle n(\nu), s|) \quad (6)$$

$J_{inter}$  indicates interchain coupling strength. It should be noted that the disorder is not considered in the above Hamiltonian.

In the absence of the disorder, one could treat the exciton coupling term in eq(6),  $\sum_n J_{inter} (|n(\nu), \acute{s}\rangle \langle n(\nu), s|)$ , as a perturbation and use single-particle approximation (where  $t_e, t_h$  are assumed to be negligible, and *exciton coupling*  $\ll \hbar\omega_0\lambda_0^2$ ) to calculate zero-order vibronic excitons in the wave-vector space that is defined as,<sup>26</sup>

$$|K(n, \nu, s)\rangle^0 = \sum_n \phi_{k,n} |n(\nu), s\rangle \quad (7)$$

Considering the cycling boundary conditions, which is the case in P3HT, the expansion coefficients is given by

$$\phi_{k,n} = N^{-\frac{1}{2}} \exp(ikn), \quad k = 0, \pm \frac{2\pi}{N}, \pm \frac{4\pi}{N}, \dots \quad (8)$$



where  $N$  is the number of chromophores in Sth chain. The corresponding (first-order) transition frequency  $\omega_k^{n(v)} = \varepsilon_e + \varepsilon_h + v\omega_0 + 2J_{inter} \cos(k) \langle o|v \rangle^2$  is a function of  $k$  and  $v$ ; where  $k$  denotes the wave vector of terminated energy level, and  $v$  is the number of vibrational quanta that is coupled to the electronic transition. Here  $|\langle o|v \rangle|^2$  represents vibrational overlap between vibrationless ground state oscillator wave function and shifted excited state oscillator wave function with  $v$  quanta. Figure 1-7 shows the approximate vibronic energy structure of the chain in the strong electron-phonon coupling regime (weak exciton coupling). The lowest and highest energy levels of the  $v$ th exciton band are  $\varepsilon_e + \varepsilon_h - U + v\omega - 2|J_{inter}| \langle o|v \rangle^2$  and  $\varepsilon_e + \varepsilon_h - U + v\omega + 2|J_{inter}| \langle o|v \rangle^2$ , respectively, with bandwidth proportional to  $W=4|J_{inter}|$ , where  $W$  is referred to as exciton bandwidth.<sup>26</sup>

In an H-type polymer aggregate ( $J_{inter} \geq 0$ ), the energy levels within the exciton band *increases* as  $k$  decreases from  $\pi$  to 0, where  $k=0$  characterizes a node-less symmetric energy band-structure and  $k=\pi$  illustrates antisymmetric band-structure. At

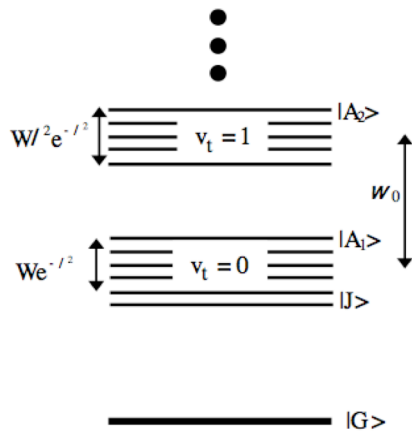


**Figure 1-7: Energy level structure of polymer aggregate in the strong EP coupling regime. The lowest energy exciton, |J>, occurs in the  $v=0$  band which is capped by |A<sub>1</sub>> exciton (Printed from ref. 26).**

zero temperature, all the electrons reside on the vibrationless ground state ( $k=0$ ). Therefore, based on momentum conservation principle only the nodeless symmetric exciton in  $v=0$  band of the excited state can be optically accessible, which is referred as |A<sub>1</sub>> exciton. The antisymmetric exciton, labeled a |J> exciton, is the lowest-energy exciton in H-

aggregate in  $v=0$  band and is responsible for emission at low temperatures.<sup>26</sup>

In aggregates with weak, but not negligible, intramolecular coupling (like P3HT), transport along the polymer backbone can be described as two-step electron-hole events involving neutral F-like excitons within a single unit cell. In such aggregates, the two summation terms of  $H_{ele}$  can be approximated by  $-(U+2J_{intra})$  with  $J_{intra}=-2t^2/(U-V_1)$ , assuming that  $t_e=t_h=t$ .  $J_{intra}$  represents the Frenkel exciton strength and is defined to be negative. This chain Hamiltonian is called the effective Frenkel Hamiltonian,  $H_{FS}$ . The Hamiltonian of aggregate is then given by sum of single chain Hamiltonians

$$\hat{H}_{aggregate} = \sum_s (\hat{H}_{Fs} + \sum_{\acute{s}=s\pm 1} \sum_n J_{inter} |n(v), \acute{s} \rangle \langle n(v), s|) \quad (9)$$

Including up to 3-particle Frenkel-like and charge-separated (CS) states and assuming periodic boundary conditions along the polymer backbone that includes  $N$  unit cells, all the eigenstates of the Hamiltonian can be described by two dimensionless wave vectors:  $k_{||} = 0, \pm \frac{2\pi}{N}, \pm \frac{4\pi}{N}, \dots, \pi$  along the chain and  $k_{\perp} = 0, \pi$  along the stacking axis. So the  $\alpha$ th eigenstate of each unit cell is now denoted as  $|\psi(k_{||}, k_{\perp}, \alpha) \rangle$  and has energy  $\varepsilon_{k_{||}, k_{\perp}, \alpha}$ , where eigenenergies increase as  $\alpha$  increases.<sup>24</sup> Because  $J_{inter}$  is taken to be positive, as in an H-aggregate, the lowest energy exciton is antisymmetric and is described by  $K_{||}=0$  and  $k_{\perp} = \pi$  and  $\alpha=1$ ,  $|\psi(0, \pi, 1) \rangle$ . The first excited state is capped by the nodeless symmetric exciton described by  $K_{||}=0$  and  $k_{\perp} = 0$ , and  $\alpha=1$ ,  $|\psi(0, 0, 1) \rangle$ .

Given the eigenstates of the aggregate, the dimensionless absorption  $A(w)$  and emission spectrum can be obtained using the following expression<sup>24</sup>

$$A(w) = \left(\frac{1}{\mu_0^2}\right) \sum_{\alpha} |\langle G|\mu|\psi(0, \pi, 1) \rangle|^2 W_{LS} \left(\varepsilon - \varepsilon_{k_{||}=0, k_{\perp}=\pi, \alpha=1}\right), \varepsilon = \hbar w \quad (10)$$

Absorption in aggregates is governed by symmetric exciton with excitonic energy defined as  $\hat{J}_{k_{\parallel}=0, k_{\perp}=0} = 2J_{intra} + 2J_{inter}$ , factor 2 indicates that each unit cell is interacting with its two neighboring cells along the chain and two cells on the adjacent chains as shown in figure 1.6b. Since  $J_{intra}$  and  $J_{inter}$  have opposite signs,  $J_{k_{\parallel}=0, k_{\perp}=0}$  can be either negative or positive. When electronic coupling is weaker than vibronic coupling, using eq (10)  $A_{0-0}/A_{0-1}$  ratio can be determined from perturbation theory as<sup>24</sup>

$$\frac{A_{0-0}}{A_{0-1}} \approx \frac{(1 - \frac{G(\lambda_0^2; 0) e^{-\lambda_0^2 J_{k_{\parallel}=0, k_{\perp}=0}}}{\hbar\omega_0})^2}{\lambda_0^2 (1 - \frac{G(\lambda_0^2; 1) e^{-\lambda_0^2 J_{k_{\parallel}=0, k_{\perp}=0}}}{\hbar\omega_0})^2} \quad (11)$$

where the vibronic factor is

$$G(\lambda_0^2; \nu) \equiv \sum_{\substack{u=0,1 \\ u \neq \nu}} \frac{\lambda^{2u}}{u!(u-\nu)} \quad \nu = 0, 1, 2, \dots \quad (12)$$

generally vibronic factor is positive, and for realistic HR factor we have ( $\lambda_0^2 \leq 3$ ),  $G(\lambda_0^2; 0) > G(\lambda_0^2; 1)$ . The absorption intensity ratio indicates that in the H- aggregates when excitonic energy is positive,  $J_{intra} < J_{inter}$ , the absorption intensity ratio is smaller than one. By contrast, when excitonic coupling energy is negative in aggregates with strong intrachain coupling,  $J_{intra} > J_{inter}$ , the intensity ratio is enhanced relative to  $1/\lambda_0^2$  representing J-aggregate characteristics.

The emission spectrum of the aggregate can also obtain from the given eigenstates using the expression

$$S(w) = \sum_{\nu=0,1,2,\dots} \langle I_{k_{\parallel}, k_{\perp}, \alpha}^{0-\nu} W_{LS}(\varepsilon - \varepsilon_{k_{\parallel}=0, k_{\perp}=\pi, \alpha=1} + \hbar\nu w_0) \rangle_T, \quad \varepsilon = \hbar w \quad (13)$$

Here,  $\mu$  is the dipole moment operator,  $\mu \equiv \mu_0 \sum_s \sum_n (c_{n,s}^+ d_{n,s}^+ + c_{n,s} d_{n,s})$  with  $\mu_0$  equal to  $S_0 \rightarrow S_1$  transition;  $|G\rangle$  is the vibrationless ground state. Also,  $W_{LS}$  is a transition line shape function chosen here to be peak-normalized Gaussian,  $W_{LS} = \exp\left(-\frac{w^2}{\Gamma^2}\right)$ , with the

line width  $\Gamma$  that reflects mainly inhomogeneous broadening. In the emission term,  $I_{k_{||},k_{\perp},\alpha}^{0-\nu}$  represents all transitions originating from the states on either lower, symmetric ( $K_{||}=0$  and  $k_{\perp} = 0$ ) or upper, antisymmetric ( $K_{||}=0$  and  $k_{\perp} = \pi$ ) exciton band and terminating on the ground electronic states with a total of  $\nu_t$  vibrational of quanta distributed over the  $N$  nuclear potentials  $S_0$ .

$$I_{k_{||},k_{\perp},\alpha}^{0-\nu} = \left(\frac{1}{\mu_0^2}\right) \sum_{\nu_1,\nu_2,\dots,\nu_N} |\langle \psi(k_{||},k_{\perp},\alpha) | \hat{\mu} | g; \nu_1, \nu_2, \dots, \nu_N \rangle|^2 \quad (14)$$

Accordingly, the 0-0 to 0-1 PL intensity ratio in the thermodynamic limit is given by,<sup>24</sup>

$$\frac{I_{0-0}}{I_{0-1}} = \frac{2e^{-\frac{2FJ_{inter}}{k_bT}}}{\lambda_0^2(1+e^{-\frac{2FJ_{inter}}{k_bT}})} \sqrt{\frac{4\pi F|J_{intra}|}{k_bT}} \quad N > \sqrt{4\pi\hbar\omega_0/k_bT} \quad (15)$$

where the simplified form of the band bottom curvature,  $\hbar\omega = F|J_{intra}|$  was used, with  $F$  defined as the Franck-Condon factor. This expression indicates that the PL intensity ratio scales as  $1/\sqrt{T}$ . Moreover, it illustrates the influence of interplay between interchain and intrachain coupling on the PL intensity ratio, increasing intrachain coupling elevates PL intensity ratio while enhanced interchain coupling reduces PL intensity ratio.

Figure 1-8 depicts the calculated absorption and emission spectra of P3HT aggregate from eqs (10) and (14), with  $J_{intra} < J_{inter}$ , representing J-aggregate-like behavior, and  $J_{intra} > J_{inter}$ , representing H-aggregate

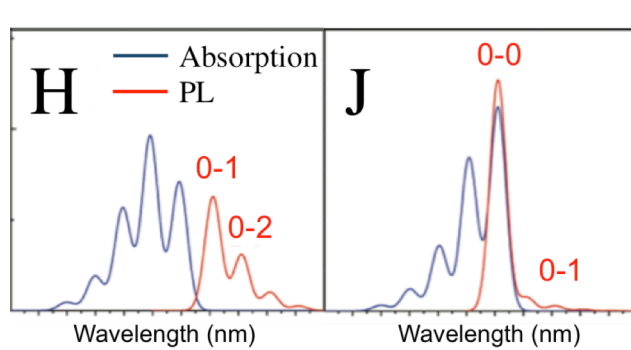


**Figure 1-8: Representative absorption and emission spectra in H- and J- aggregate. The 0-0 PL origin in H-aggregate is symmetry forbidden while it is the dominant radiative transition in J-aggregate (Printed from ref. 18).**

behavior. It clearly denotes that the dominant coupling (aggregate-type) in P3HT can be altered between H- and J-type aggregate due to the fact that intrachain (Frenkel) exciton and interchain (wannier) exciton coupling strengths are comparable to each other and both are sensitive to the structural disorder of the system. As a result, tuning the morphology can alter the photophysical properties of P3HT aggregate between H-dominant and J-dominant coupling. The manifestations of H- and (J)- aggregate properties are evident in 1) a decrease (increase) in the  $A_{0-0}/A_{0-1}$  absorption spectral ratio, and 2) an increase (decrease) in the  $I_{0-0}/I_{0-1}$  emission intensity ration with increasing disorder. Indeed, this inclusive theoretical study conducted by Spano and coworkers,<sup>22-24, 26, 27</sup> illustrates a vital excitonic picture of P3HT nanostructures, referred as HJ-aggregate framework. Accordingly, evaluating intensity ratio of vibronic progression of absorption and emission spectra of P3HT nanostructures within the HJ-aggregate framework one can assess molecular packing, structural order, the strength of exciton coupling, and the nature of disorder in the aggregates.

#### 1-4 Crystalline poly (3-hexylthiophene) nanofibers

Poly (3-hexylthiophene), P3HT, is perhaps one of the most studied organic polymers in the past decade due to its potential application in organic photovoltaic devices,<sup>28-30</sup> plastic light emitting diodes,<sup>31-33</sup> and field effect transistors.<sup>34-36</sup> It is a conjugated polymer of

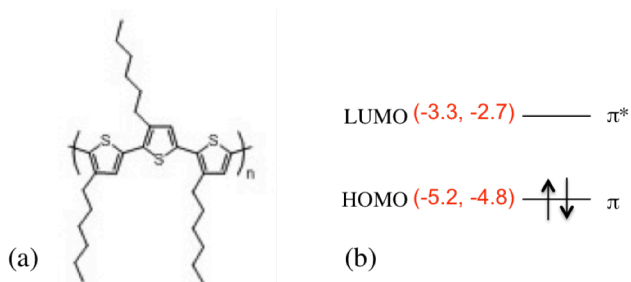


**Figure 1-9: Chemical schematic (a) and energy diagram of frontier orbitals, HOMO and LUMO, (b) of Poly (3-hexylthiophene).**

thiophene units substituted with hexyl chains in the '3'-position linked together at the 2, 5 positions with chemical structure as depicted in figure 1-9. It becomes conductive by removing or adding electrons to the conjugated  $\pi$ -orbital via doping. P3HT tends to self-assemble into lamellar sheets that can  $\pi$ -stack to form crystalline aggregate structures. This leads to two-dimensional exciton coupling: along the polymer chain and through  $\pi$ -stack direction. The extensive studies on structure and photoluminescence of semicrystalline pristine P3HT and composite P3HT/PCBM thin films indicate that optical properties of exciton coupling, charge mobility, and power efficiency conversion (PEC) in these films are rather intricate functions of polymer chain properties (molecular weight, regioregularity, polydispersity), as well as solvent and processing conditions.<sup>10, 37-47</sup> Therefore, these parameters can be manipulated to "tune" specific packing structures and couplings in which in turn directly affect optical and electronic properties of the P3HT structure in the active layer of devices. The question of interest to us is that what kind of couplings are present in P3HT aggregates, and how to tune coupling strength (eg. molecular weight, solvent processing, cross-linking, etc.) according to the priorities of the application. Chain folding has been suspected to be an important factor in determining electronic properties of P3HT aggregates, but there is little known about its photophysical consequences and how (chain folding) influences the strength of two dimensional excitonic coupling.

The intrinsic nanoscale structural heterogeneity of the films limits our ability to make a complete and quantitative correlation between their morphology and optoelectronic properties. Isolated P3HT nanofibers of an interesting experimental platform for study as the fundamental crystalline aggregate structure in poly- or semi-

crystalline films. Because their nominal internal chain packing structure is known. Isolated nanofibers also present well defined crystal axis orientations in the lab frame enabling polarization studies referenced to specific intra- or inter-chain directions.<sup>48</sup> Indeed, morphology dependence of exciton coupling and electronic properties in P3HT aggregates can be appreciated by investigating chain conformation impact on the optoelectronic properties of P3HT nanofibers. This can be achieved by optically probing single nanofibers that are self-assembled by  $\pi$ -stacked lamellar sheets in which polymer stem length corresponds to nanofiber width.

In this thesis, I have combined different single molecule spectroscopy methods with scanning probe techniques (AFM, KPFM, and NSOM), and transmission electron microscopy (TEM) to optically assess exciton coupling strength in nanofibers with different molecular weights and examine their electronic properties. Figure 1-10 shows the schematic of my experimental setup. Utilizing a multichannel emission path, I have conducted a systematic study on wavelength, time, and polarization-resolved single P3HT nanofiber photophysics as a function of polymer chain length.

Correlating the optical and electrical properties with nanofiber width unravels the impact of chain conformation on the strength and effective dimensionality of exciton coupling as well as HOMO energy level, and indicates how confinement influences the molecular packing and optoelectronic properties. The results of this in depth study suggest how the HOMO energy level and dimensionality of exciton coupling in P3HT nanofibers can be tuned by modulating chain conformation. Indeed, it indicates that the aforementioned design parameters affect optoelectronic properties through modification of chain conformation.

Moreover, cross-linking functionalized nanofibers is represented as a unique technique to make chemically and mechanically robust nanostructures through which exciton coupling strength and frontier energy levels in pre-formed aggregates can be further fine-tuned via cross-linkage size and solvent annealing.

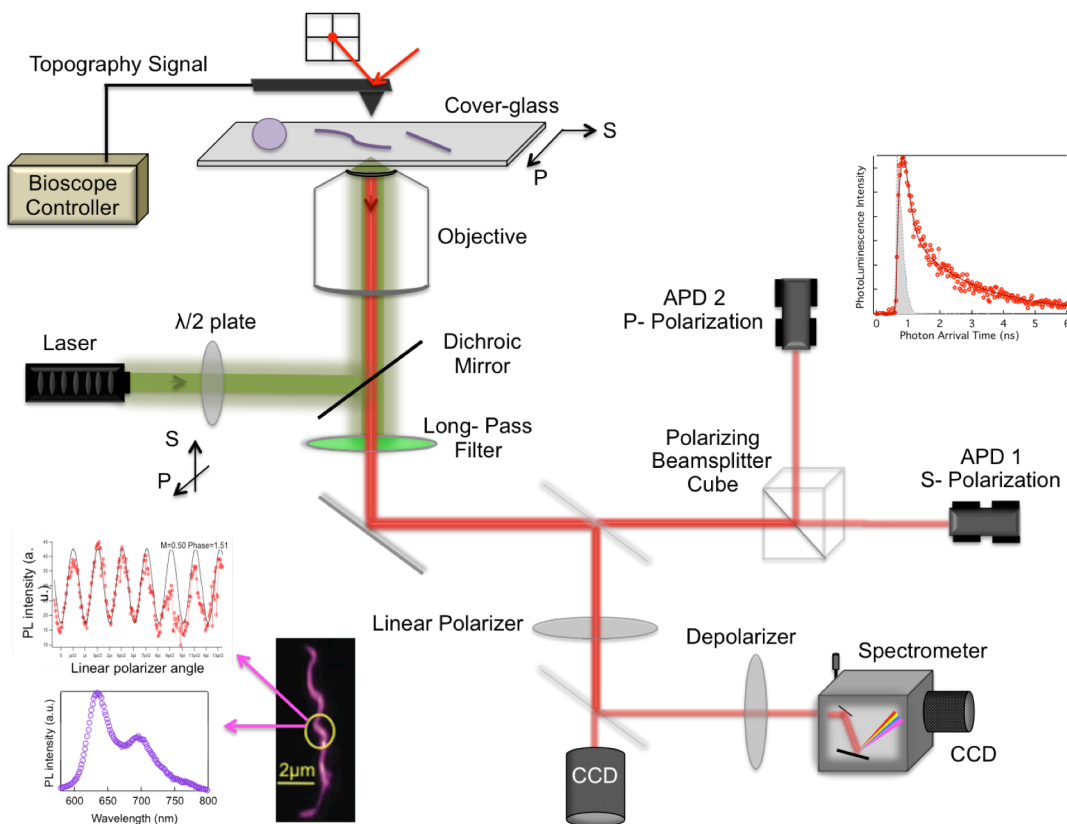


**Figure 1-10: Schematic of experimental system used for size correlated chemical microscopy. Multichannel emission path provides access to photoluminescence spectrum in energy, polarization, and time domain.**



## CHAPTER 2

### OPTICAL PROBING AND TUNING TWO-DIMENSIONAL EXCITON COUPLING IN POLY (3-HEXYLTHIOPHENE) NANOSTRUCTURES

Exciton generation, migration, and dissociation are key processes that play a central role in the design and operation of organic optoelectronic devices. These processes are quite sensitive to both short- and long-range structural order. Optical probes of molecular structure, polymer chain packing and exciton dynamics offer insights into relationship between aggregate structures and optoelectronic properties to engineer high performance organic based electronic devices.

Of the vast library of organic semiconductors developed over the past 30 years, poly-3-hexyl thiophene P3HT remains one of the most widely used, owing to its high charge carrier mobility.<sup>49</sup> Yet, despite extensive studies correlating structure with photoluminescence of semicrystalline P3HT films, intrinsic nanoscale structural heterogeneity complicates a complete and qualitative correlation between their

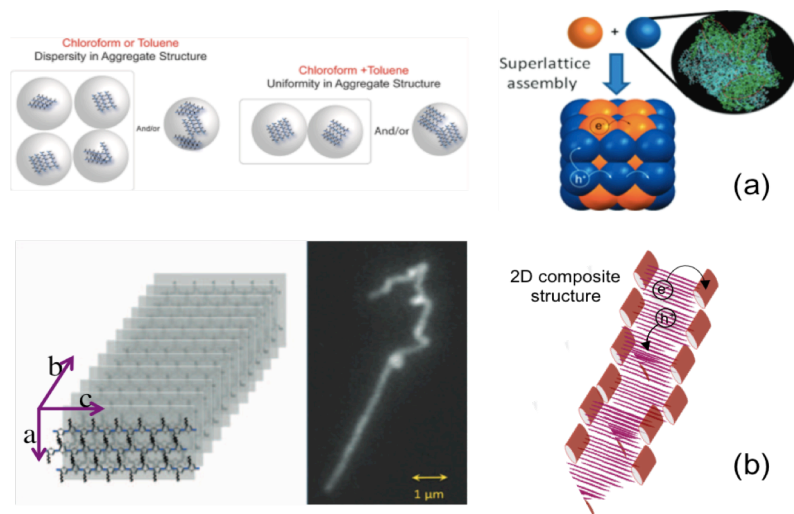


**Figure 2-1: Structural schematic of (a) P3HT nanoparticles and 3D P3HT/PCBM nanoparticle superlattice, and (b) nanofibers and 2D P3HT/CdSe nanorod composite via co-crystallization.**

morphology and optoelectronic properties.<sup>50, 51</sup> Isolated nanostructures (e.g. nanofibers, or nanoparticles) of P3HT offer a route toward disentangling these structural heterogeneities.<sup>52-56</sup> In particular, nanofibers represent an attractive platform for study because the nominal (highly crystalline) internal chain packing structure is known.<sup>48</sup> As shown in Figure 2-1 nanoparticles or nanofibers (or combinations) can be utilized as building blocks for assembling binary assemblies for organic photovoltaic active layers aiming to better control donor and acceptor domain size and interfacial contact to provide continuous and separate conduction path for electrons and holes (figure2-1).

In the first part of this chapter, I discuss experiments designed to probe the photoluminescence (PL) spectra and polarization dynamics of isolated, crystalline, high regioregular P3HT nanofibers as a function of polymer molecular weight ranging from 10 to 65 kDa. The effect of increasing molecular weight is manifested in distinctly different dominant coupling types: from H-type in the low MW regime, to predominant J-type in the high MW regime. The mechanism for this trend appears to be polymer chain folding as evidenced by TEM imaging, which reveals that nanofiber widths (transverse direction) take on a constant value for MW > 13 kDa. Picosecond time- and polarization-resolved PL dynamics show a clear transition from predominantly one-dimensional (J-type) coupling to two-dimensional coupling (both intra- and interchain) as MW is decreased. These effects can be explained within a structural picture in which high MW P3HT chains fold within the lamella resulting in enhanced chain planarity and possible loss of thiophene ring registration (slip-stacking) in the subsequent lamellar packing.

In the second part of this chapter I represent size correlated optical properties of P3HT nanoparticles with focus on how confinement influences structural order and

excitonic coupling. It appeared that in confined nanostructures where chain packing is frustrated both kinetically and spatially, the J-type coupling is primarily associated with minimum energy polymer packing, while H-type coupling is associated with higher-energy packed states.

## 2-1 Physics of P3HT nanofibers within H/J- aggregate framework

One-dimensional crystalline P3HT nanofibers form via self-assembly of polymer chains into lamellar sheets and subsequent  $\pi$ -stacking in marginal solvents.<sup>57</sup> Crystalline P3HT nanofibers have been studied extensively by electron microscopy and grazing incident wide angle x-ray diffraction; the crystallographic a, b, c-axes correspond to the vertical (alkyl chain), longitudinal ( $\pi$ -stack), and transverse (polymer backbone) dimensions, respectively (Figure 2-2).<sup>56-58</sup>

Two-dimensional exciton coupling in aggregates, intrachain (through-bond) and interchain (through-space) exciton couplings, results in exciton diffusion/migration along the intra-chain (polymer backbone, or c-axis) as well as the  $\pi$ -stack inter-chain direction.

The interplay between the inter- and intrachain couplings and thus effective dimensionality of exciton dynamics are controlled by molecular packing, which strongly depends on polymer properties, solvent, and processing conditions.

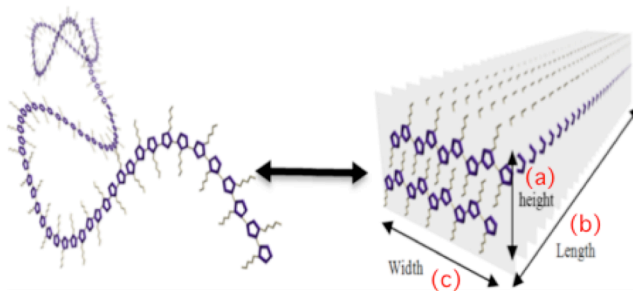


**Figure 2-2: Schematic illustration of (left) single P3HT chain in a good solvent (e.g., chloroform) and (right) self-assembly P3HT nanofiber in a marginal (e.g. toluene, or dichloromethane) solvent. The crystallographic axes are shown relative to nanofiber axes (Printed from ref. 56).**

### 2-1-1 Probing two-dimensional exciton coupling strength in P3HT nanofibers

Moule and coworkers studied the effect of solvent on formation kinetics of nanofibers and the strength of the exciton coupling by comparing the  $A_{0-0} / A_{0-1}$  intensity ratio in absorption for nanofibers prepared from different solvents.<sup>59</sup> Figure 2-3 shows the suspended- phase absorption spectra of P3HT nanofibers with high molecular weights (nominally 48 and 65 kDa) from different solvents. As implied by the HJ aggregate model developed by Spano, the increase in  $A_{0-0}/A_{0-1}$  intensity ratio with lowering solvent quality (i.e., a decrease in the Flory-Huggins parameter) indicates dominant J-type coupling (stronger intrachain coupling) along with higher chain planarity is associated with poorer solvent quality.

In addition, Grey and coworkers examined the effect of solvent on PL properties of isolated high MW nanofibers.<sup>54</sup> The solid- state photoluminescence spectra of high molecular weight nanofibers from anisole and toluene are depicted in figure 2-4. It shows that  $I_{0-0}$  to  $I_{1-0}$  PL intensity ratios of both nanofibers are larger than one, characteristic of

J-type aggregate, indicating dominant intrachain exciton coupling in high molecular weight nanofibers. Importantly, J-type P3HT aggregates are sensitive to seemingly minor changes in intrachain order such as temperature- and pressure- induced changes in

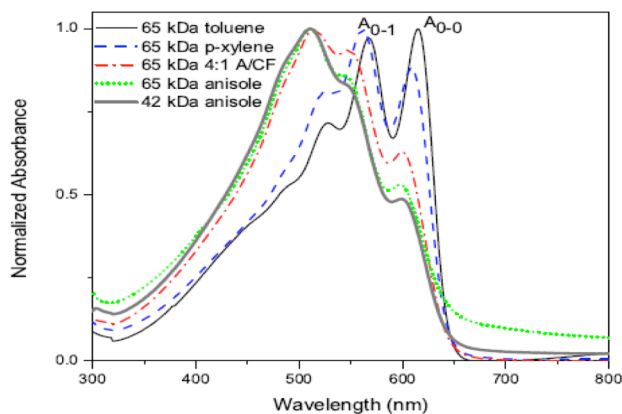


**Figure 2-3: Effect of solvent on dominant coupling in P3HT nanofibers. Lowering solvent quality enhances polymer chain planarity leading to stronger intrachain coupling as evidenced by an increase in the  $A_{0-0}/A_{0-1}$  intensity ratio (Printed from ref. 58).**

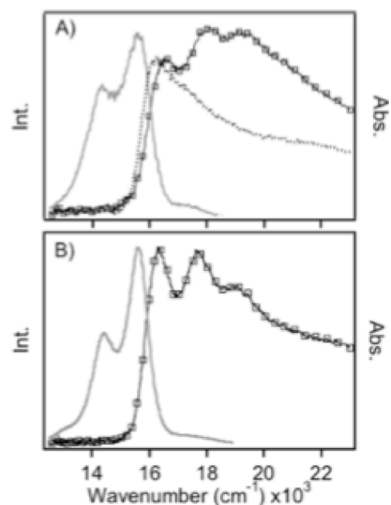


**Figure 2-4:** PL (solid line) and absorption (solid dotted line) spectra of high MW P3HT nanofibers formed in anisole (A) and toluene (B) (Printed from ref. 53).

their packing arrangement from a type I to type II configuration (figure 2-5(right)) causing the observed revolutions in both temperature- and pressure-dependent PL spectra.

While all of the aforementioned solubility, pressure, and temperature studies on nanofibers have been mostly conducted on high molecular weight (>48 kDa) P3HT, a wealth of new information can be achieved by photoluminescence studies of low

packing (NF volume). Increasing  $I_{0-0} / I_{1-0}$  PL intensity ratio from 1.5 at 4 K to about 2 at room temperature (figure 2-5(left)) and pressure dependent PL lifetime suggest a change in the nanofiber chain packing as temperature and pressure changes. It was proposed by Grey and coworkers that the P3HT alkyl side groups change

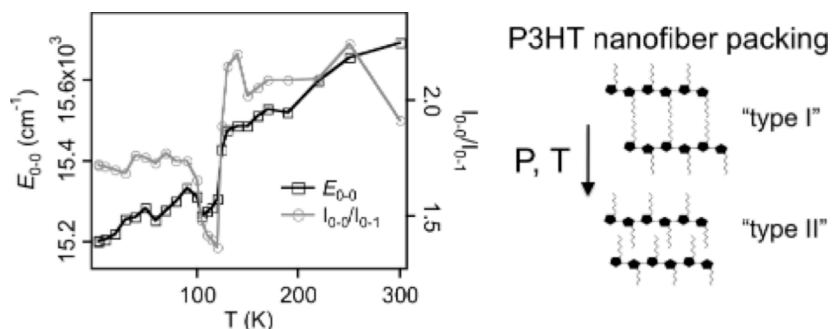


**Figure 2-5:** (left) Temperature dependent photoluminescence emission origin ( $E_{0-0}$ ) and  $I_{0-0} / I_{1-0}$  PL intensity ratio of high molecular weight P3HT nanofibers. (Right) Schematic illustration of P3HT nanofiber packing modification as temperature and pressure increases (Printed from ref. 53).

molecular weight nanofiber. Molecular weight study in P3HT thin films and spin-cast nanofibers indicated that charge carrier mobility increases by molecular weight up to a critical value and then levels off. This molecular weight-dependent behavior of charge carrier mobility is attributed to the chain conformation in the nanostructures; extended conformation in low Mn vs folded conformation in high Mn.<sup>60</sup> However, the origin of this remarkable dependence and photophysical consequences of conformational changes have not been identified yet. In what follows, I have studied chain conformation dependence of two dimensional exciton coupling in P3HT nanofibers with different

molecular weights aiming to explain the observed molecular weight dependent behavior in aggregates.

Figure 2.6a, b show representative PL images of single nanofibers from 13 and 65

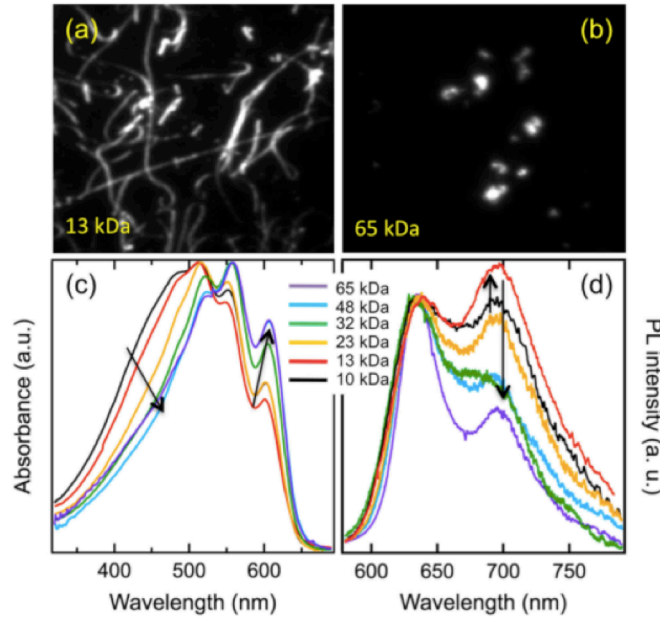


**Figure 2-6: Representative photoluminescence images of nanofibers on cover glass made from (a) 13 kDa and (b) 65 kDa P3HT. Ensemble absorption spectra of suspended nanofibers in CF/DCM mixed solvent (c) and solid-state emission spectra of individual nanofibers (d) made from P3HT with a variety of molecular weights: 10 (black), 13 (red), 23 (yellow), 32 (green), 48 (blue), and 65 (purple) kDa. Arrows in panels c and d indicate changes in the spectral features as molecular weight is increased.**

kDa P3HT respectively. Nanofibers (NFs) of high regioregular (98%) P3HT with different molecular weights (ranging from 10 to 65 kDa as measured by gel permeation chromatography (GPC)) were prepared by adding dichloromethane (DCM) to the well-dissolved P3HT in chloroform (CF) (0.2 mg/mL) for a final 1:7 volume ratio of CF to DCM, and samples were left at 0 °C in the dark overnight. The 10-48 kDa P3HT samples with 1.2 PDI were synthesized using standard Grignard Metathesis, and 65 kDa P3HT with 2.1 PDI was purchased from Aldrich and used as supplied.

Low MW P3HT nanofibers have significantly extended structure (up to tens of micrometers), while high MW P3HT nanofibers appear much shorter ( $\leq 1 \mu\text{m}$ ). Figure 2.6c shows steady-state ensemble absorption spectra of P3HT nanofibers (suspended in CF/ DCM mixed solvent) with different molecular weights. The absorption spectra of such suspensions contain contributions from both low-energy crystalline and a higher-energy amorphous P3HT; the contribution of the crystalline component can be extracted by subtracting the scaled measured absorption spectrum of well-dissolved P3HT in chloroform, which is peaked at 450 nm. All of the absorption spectra are normalized to their maximum values to better

represent the decrease (increase) of amorphous (crystalline) contribution to the spectrum as molecular weight increases. Figure 2-7 shows corresponding amorphous (dashed line) and crystalline (solid line) absorption components of nanofibers absorption

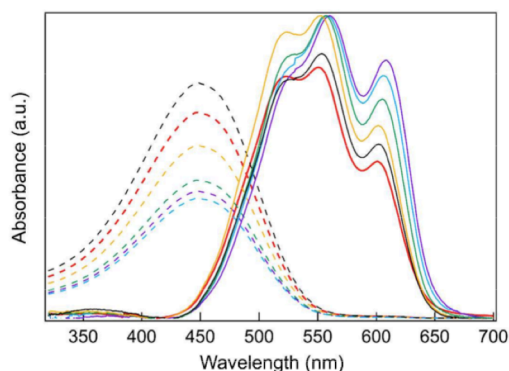


**Figure 2-7: Amorphous (dashed line) and crystalline (solid line) component of absorption spectra of corresponding P3HT nanofibers with various molecular weight shown in figure 2.6.**

spectra depicted in figure 2.6c. The nearly monotonic decrease in the contribution of amorphous absorption with increasing molecular weight is likely due to a decrease in solubility with molecular weight.

Within the weak interchain coupling framework model developed by Spano,<sup>27</sup> we can assess the strength of the interchain coupling in the P3HT nanofiber families through the simplified form of equation (11)

$$\frac{A_{0-0}}{A_{0-1}} \cong \left( \frac{1 - 0.24W/\hbar w_0}{1 + 0.073W/\hbar w_0} \right)^2 \quad (12)$$

where  $w_0$  is the frequency of the vibrational mode coupled to the electronic transition ( $w_0 \sim 170$  meV). Here, the strength of excitonic coupling between neighboring chains (free-exciton bandwidth,  $W$ ) is related to the ratio of the absorption origin and its first vibronic replica intensities,  $A_{0-0}/A_{0-1}$ . Figure 2-8 shows the free-exciton bandwidth (blue diamond) computed from eq 12 for different nanofiber families plotted as a function of molecular weight (as measured by GPC). Interestingly, the free exciton bandwidth of

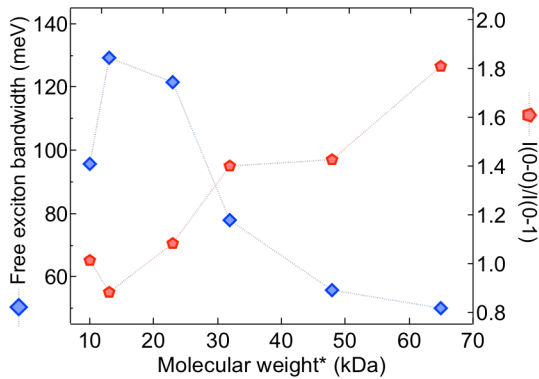


**Figure 2-8: (top) Free-exciton bandwidth (blue diamonds) and corresponding  $I_{0-0}/I_{0-1}$  PL intensity ratios (red pentagon) from nanofibers of different P3HT molecular weights.**

P3HT nanofibers increases from 95 to 130 meV as molecular weight is increased from 10 to 13 kDa and then decreases as molecular weight is increased to 65 kDa. This reveals that the interchain coupling strength does not change monotonically as molecular weight increases, and in



fact, it is maximum for NFs made with 13 kDa P3HT.

Figure 2-6d shows the wavelength resolved photoluminescence of individual P3HT nanofibers in the solid state normalized to their 0-0 PL peak intensities. Unlike the ensemble absorption, single nanofiber photoluminescence shows minimal (high- energy) contributions from free P3HT and produces purely crystalline emission spectra of P3HT nanofibers. Based on HJ aggregate model,  $I_{0-0}/I_{0-1}$  intensity ratio in the photoluminescence spectrum identifies the type and strength of the dominant excitonic coupling in P3HT aggregates including isolated nanofibers.<sup>24</sup> The  $I_{0-0}/I_{0-1}$  intensity ratio of each nanofiber family was measured by fitting its PL spectrum with a vibronic progression consisting of three Gaussian functions and was plotted as a function of molecular weight in Figure 2-8 (red pentagons). With a trend similar to absorption, the PL intensity ratios of NFs first decrease from 1 to 0.88 as molecular weight is increased from 10 kDa to the critical 13kDa value and then rise with molecular weight increase to 1.81 at 65 kDa. While the changes in the exciton bandwidth extracted from the absorption spectrum report only on changes in the interchain coupling strength, the extremum in the intensity ratio of the emission spectrum at critical molecular weight indicates a transition in the dominant excitonic coupling type from weak H-type to strong J-type coupling with increasing molecular weight. These spectroscopic results beg the question of what structural variations between the different molecular weight nanofibers drive the observed changes in exciton coupling type and strength.

Silva and coworkers have demonstrated that the intrachain coherence length is a dominant factor governing the electronic communication in films.<sup>61</sup> They indicated further that the two-dimensional excitonic coupling balance is sensitive to the chain

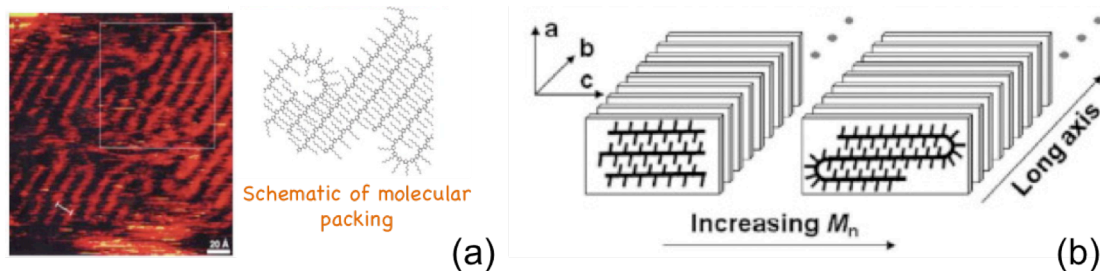


**Figure 2-9: (a) TEM image of single layer P3HT film along with schematic of its molecular packing. (Printed from ref. 64) (b) Schematic illustration of chain folding within the lamellae as molecular weight exceeds a critical value (Printed from ref. 56).**

planarity in the aggregate region, and that reduction of torsional disorder is associated with enhanced intrachain coherence length, thus reducing interchain excitonic coupling as evidenced spectroscopically by changes in intensities of electronic origin and vibronic sidebands. Several studies have reported that as molecular weight of the polymer chain exceeds a critical value, the folded conformation becomes energetically more favorable than the extended conformation;<sup>57, 60, 62-64</sup> which is consistent with Scanning tunneling microscopy (STM) evidence of polymer chain folding and side chain interdigitation in high molecular weight P3HT reported by Bauerle and coworkers (figure 2-9a).<sup>65</sup> Liu et al. demonstrated that single nanofibers are composed of a collection of single lamellar sheets, in which the lamellar thickness corresponds directly to the stem length (figure 2-9).<sup>57</sup> Therefore, TEM imaging of single nanofibers affords direct access to the stem length, which we have correlated with the photophysical changes to further probe the observed transition at 13 kDa molecular weight.

Figure 2-10 shows representative TEM images of individual extended P3HT nanofibers from 10, 13, and 65 kDa molecular weight from CF/DCM mixed solvent. The width of all the nanofibers in figure 2-6 are measured from the TEM images, normalized histogram of which are depicted in figure 2-10. Nanofiber average width and the standard

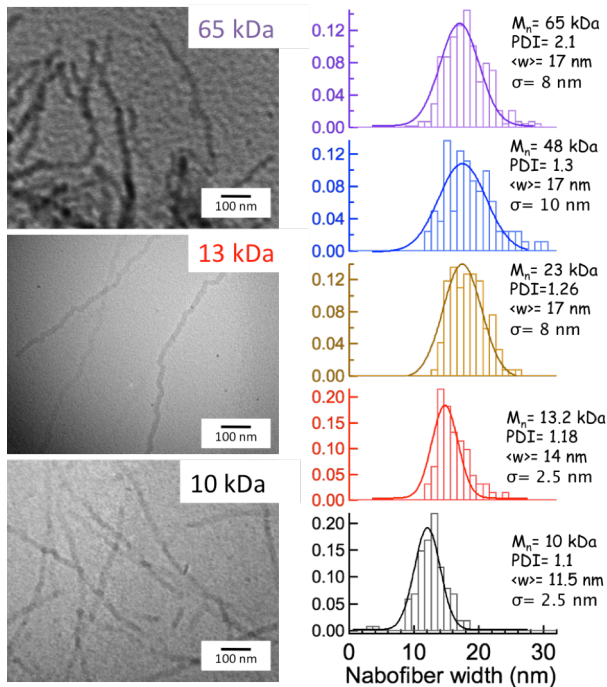


**Figure 2-10: Left: Representative TEM images of 10 kDa, 13 kDa, and 65 kDa P3HT nanofibers. Right: Normalized width histogram of P3HT nanofibers with high regiorigularity, and molecular weight ranging from 10 kDa to 65 kDa. Average nanofibers width is proportional to the contour length of low molecular weight polymers but level off at about 17 kDa when molecular weight exceeds 13 kDa due to chain folding above this critical molecular weight value.**

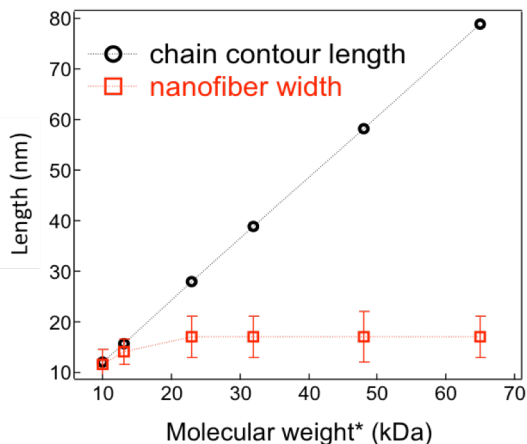
deviation are calculated by fitting normalized histograms with Gaussian function. Interestingly, the NFs average width increases by molecular weight up to 13 kDa and then levels off when molecular weight exceeds this value.

Figure 2-11 represents P3HT nanofiber widths (red squares) along with their corresponding chain contour length (black circles) as a function of molecular weight. As GPC is well-known to overestimate molecular weight determination for stiff-chain polymers, we apply a

multiplicative correction factor of 0.52, as determined by Holdcroft,<sup>66</sup> when calculating chain contour length. We observe excellent agreement between measured nanofiber width and chain contour length at low MW up to 13 kDa, and then the two curves diverge as MW exceeds 13 kDa. This observation is consistent with the previous study by Liu et al.<sup>57</sup> and clearly indicates the extended configuration of low MW chains and folded structure of high MW chains within the lamellae. On the basis of the TEM results, we conclude that the observed extremum at 13 kDa in the type and magnitude of exciton coupling inferred by spectroscopic measurement is associated with single-chain folding at

MW > 13 kDa.

Table 2-1 summarizes polymer properties and lamellar thickness of nanofiber families. The broadening of the average nanofiber width distribution (also indicated by error bar in figure 2-11) is probably due to polydispersity and edge effects in low MW nanofibers<sup>42</sup> and to heterogeneity in chain folding for high MW nanofibers.



**Figure 2-11: Molecular-weight-dependent nanofiber width (red squares) measured from TEM images and their corresponding polymer chains contour length (black circles). Chain contour lengths are calculated according to the corrected molecular weight (correction factor: 0.52). Molecular weight\* is measured by GPC.**

This critical 13kDa value marks the separation between two photophysically distinct molecular weight regimes. Below the folding threshold, the extended conformation of the chains allows for some flexibility in the polymer backbone

Molecular Weight GPC value	Polydispersity index GPC value	Molecular Weight corrected	Contour length calculated	Lamellar Thickness From TEM
10 kDa	1.1	5.2 kDa	12.1 nm	11.5 ± 3 nm extended
13 kDa	1.18	6.76 kDa	15.7 nm	14 ± 2.5 nm extended
*23 kDa	1.26	11.96 kDa	27.9 nm	17 ± 4 nm extended/folded
32 kDa	1.3	16.64 kDa	38.8 nm	17 ± 4 nm partial fold
48 kDa	1.3	24.96 kDa	58.2 nm	17 ± 5 nm single fold
65 kDa	2.1	33.8 kDa	78.8 nm	17 ± 4 nm double fold

**Table 2-1: Polymer properties and lamellar thickness of different nanofiber families and proposed chain conformation for each family. Corrected MW values are calculated by applying multiplicative correction factor of 0.52 to the measured GPC value.**

conformation, resulting in a high degree of torsional disorder, which limits intrachain coherence lengths. Therefore, interchain coupling is dominant in this regime. The observed increase in the strength of the H-coupling with increasing molecular weight in this regime is most likely due to a decrease in packing disruption (caused by the presence of noncrystallizable edge groups) as chain length increases.<sup>42</sup> For molecular weights larger than the 13 kDa threshold, interdigitation of side chains in the folded polymers limits the torsional disorder to increase the chain planarity.<sup>61</sup>

Both theory and experiment have indicated that exciton radiative decay rate of organic semiconductors mightily depends on the type of exciton coupling. J-type aggregates are known to be superradiant with notable short PL life- time compared with H- type aggregates that have low emission quantum yields and longer life- time. As a result, changes in chain planarity, inter- and intrachain coupling efficiency associated with polymer chain folding should strongly impact photoluminescence decay dynamics.<sup>56, 61, 67</sup> The measured PL decay curves from sum of single nanofibers with

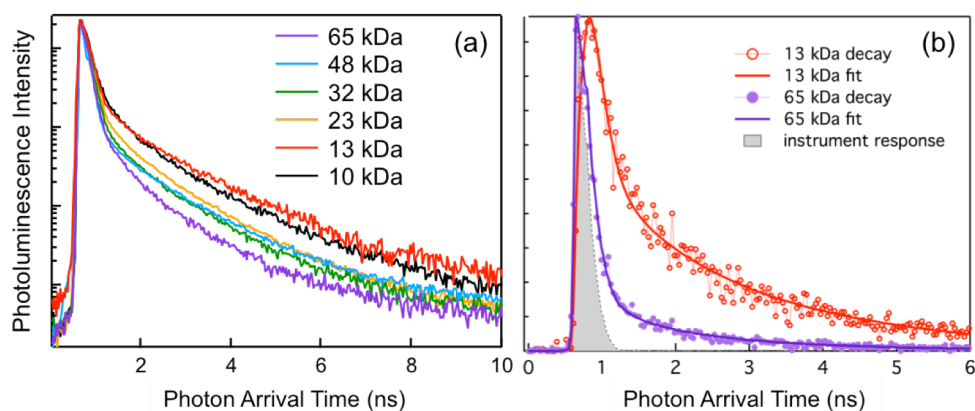


**Figure 2-12: (a) PL decay dynamics of P3HT nanofibers from different of molecular weight ranging from 10 kDa to 65 kDa. (b) PL decay dynamics of 13 and 65 kDa P3HT nanofibers that have strong H-aggregate and J-aggregate spectroscopic signatures, respectively, along with fits containing three exponentials. Measured instrument response is shown in filled gray.**

Decay Constant	13 KDa NF	65 KDa NF
$\tau_0$	N/A	Instrument Limited < 1ps
$\tau_1$	0.144 ns	0.205 ns
$\tau_2$	0.960 ns	1.04 ns
$\tau_3$	2.4 ns	2.4 ns

**Table 2.2: PL decay constants extracted from multiexponential fits of 13 kDa and 65 kDa PL decay dynamics shown in figure 2.12b.**

different molecular weights are shown in figure 2-12a. The nanofibers whose decays contributed to the sum can be fitted by multiexponential function. Table 2-2 summarizes the PL decay constants of 13kDa and 65 kDa nanofibers

and shows comparable decay dynamics in the 100 ps to nanosecond range for both extended and folded chains. For the higher Mn NFs, we observed a significant ultrafast decay component with a short time constant that was not resolvable with our instrumentation. Silva et al. recently reported a slight decrease in overall ultrafast (femtosecond) PL decay rate in P3HT films with increasing chain planarity (J-coupling).<sup>61</sup> However, such ultrafast processes are hidden in our measurements of isolated NFs. Transition dipole moment of P3HT chains are mostly parallel to their backbone, along c- axis or transverse to b-axis, therefore PL decay in isolated NFs is highly sensitive to excitation polarization (either polarized along the b- or a/c- direction); thus, this seeming disagreement could be attributed to polarization selection of crystalline domains within the film with random orientations in their study.

### **2-1-2 Effective dimensionality of exciton in P3HT nanofibers**

Figure 2-13 shows the combined effect of P3HT molecular weight and solvent processing on the H/J-aggregate character of the NFs as probed by wavelength-, time-, and polarization- resolved photoluminescence. The PL spectra were modeled as a single

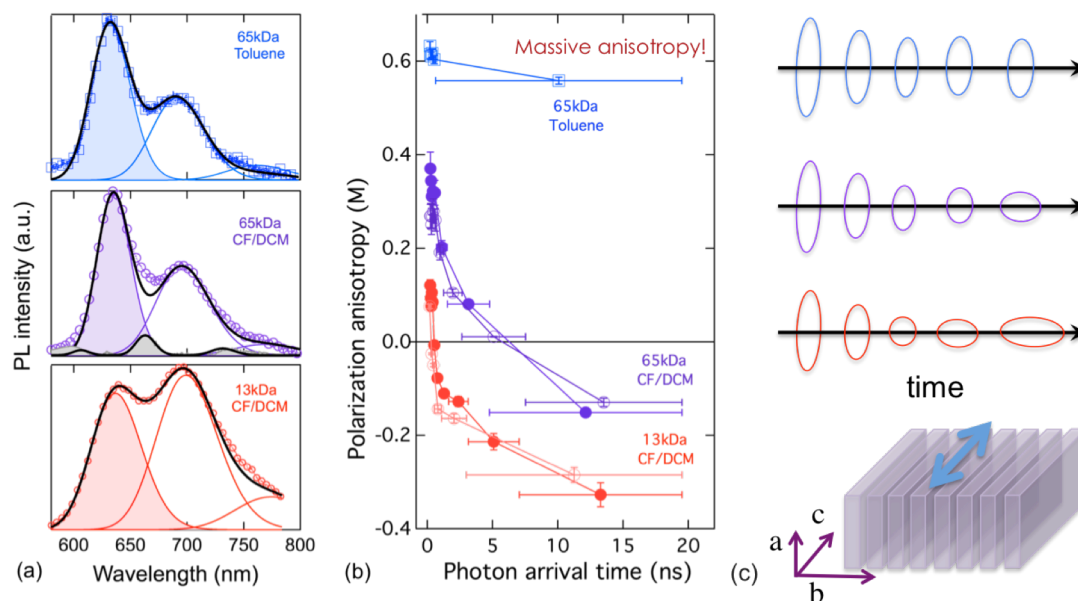


**Figure 2-13: (a) Steady-state emission spectra of individual P3HT nanofibers: 13 kDa from CF/DCM (red circle), 65 kDa from CF/DCM (purple circle), and 65 kDa from toluene (blue square). Black solid lines are model spectra consisting of a single progression of three Gaussians. Filled gray curve is the residual of the fitted model for 65 kDa NF from CF/DCM. (b) Emission polarization anisotropy of decay dynamics of corresponding P3HT nanofibers shown in (a). Positive M value corresponds to PL polarized along the chain backbone (transverse to nanofiber growth axis). (c) Graphic of P3HT nanofiber with 440 nm excitation polarization along c-axis and graphical illustration of PL polarization ellipse of exciton relative to c-axis vs. time, in nanofibers shown in (a) and (b).**

progression of three Gaussians separated by 170-177 meV, with electronic origin (0-0) transition energy, sideband intensities, and full width at half-maximum (fwhm) as adjustable parameters. The justification for allowing sideband fwhm to float as an adjustable parameter is that, within a two-particle approximation, only single-particle states are optically accessible from the (vibration-less) ground state and contribute to the 0-0 origin intensity, while sideband emission contains contributions from both single- and two-particle states.<sup>68</sup> This effect gives rise to a spectral dilation with sideband transition line widths that can be significantly larger than the origin. It is noteworthy that the low molecular weight H-type NFs (2-13a: red circle) have 0-1 sideband line widths that are about 11% larger than the origin. For 65 kDa NFs prepared from mixed solvent, the fit to

the measured PL spectrum using one vibronic progression (an ideal J-aggregate type) model is much poorer and its sideband line width is almost twice as large as that of 65 kDa toluene NFs; the residual (difference between measured and model J-aggregate spectrum) appears like a small H-type aggregate component in the PL spectrum (2-13a: filled gray curve). These subtle differences between 65 kDa NFs prepared from toluene and CF/DCM can be ascribed to the fact that although J-coupling is dominant in both high molecular weight NFs, the interchain coupling may still have a notable contribution to the emission for the mixed-solvent system.

This one-dimensional (mostly intrachain) versus two-dimensional (combined intra- and interchain coupling) behavior is further demonstrated in the polarization dynamics from the different NFs. Time- and polarization-resolved photoluminescence (TPRPL) spectroscopy can be used to disentangle intra- and interchain fluorescence processes in isolated NFs.<sup>67</sup> Using a polarized excitation pulse, we followed the time-evolution of the polarization anisotropy parameter,  $M$ , on a picosecond time scale by detecting PL photons tagged by time (relative to the excitation pulse) and polarization (parallel or transverse to the NF b-axis). Here  $M$  is defined as  $[N_{\text{trans}(t+dt)} - N_{\text{para}(t+dt)}] / [N_{\text{trans}(t+dt)} + N_{\text{para}(t+dt)}]$ , where  $N_{\text{trans,para}(t+dt)}$  are the numbers of detected PL photons polarized transverse and parallel to the NF b-axis at time  $(t + dt)$  relative to the excitation pulse. The polarization of 440 nm excitation was transverse to NF b-axis (NF growth axis). By our convention, a positive value of  $M$  corresponds to PL polarized mostly along the polymer chain axis (transverse to the NF b-axis).

As it was shown in figure 2-14b, for the 65 kDa NFs made from toluene, the polarization anisotropy parameter  $M$  was approximately constant ( $\pm 0.6$ ) over a time



scale of 20 ns. In contrast, both NFs made from mixed solvent (65 and 13 kDa) show an initial positive anisotropy, which decayed on a subnanosecond time scale giving a negative anisotropy (PL polarized mostly along the NF b-axis) at longer times. This behavior is qualitatively similar to previous reported observations where the fast decay in (positive) polarization anisotropy derives from picosecond decay of intrachain excitons, followed by relatively slow decay of interchain excitons.<sup>67</sup>

The picture that has emerged from these studies is that the initial branching ratio ( $M(\tau=0)$ ) of inter- and intrachain excitons is defined by the extent of H- and J-coupling in the NF and the mode of excitation (polarization parallel or perpendicular to the NF b-axis), and the time dependence in PL polarization anisotropy reflects the different decay rates of the inter- and intrachain species. An increase in the initial value of  $M$  as molecular weight increases indicates an increase in the relative contribution of intrachain coupling at high molecular weights, which is consistent with steady-state spectroscopic results. In both low and high molecular weight NFs made from CF/DCM mixed solvent, the electronic communication is still occurring with reasonable strength in both dimensions of the NF (they are still quasi 2D structures). However, while the inter- and intrachain coupling strengths are roughly balanced in the low molecular weight NF, they are very clearly skewed in the intrachain direction for the high molecular weight NF as a result of the folded chains. Comparing 65 kDa NFs made from CF/DCM mixed solvent with those made from toluene, the polarization contrast reveals a dramatic solvent effect, with the toluene-formed NFs appearing essentially one-dimensional.  $M(\tau)$  for the toluene NFs does not ever change sign and maintains a large positive polarization indicative of an overwhelming majority of intrachain state population. This observation is consistent with

the subtle changes in the spectra between high molecular weight NFs formed in CF/DCM mixed solvent and toluene. The change in the effective dimensionality between NFs formed via different methods from the same polymer may show that chain folding may possibly occur differently in different solvents, and so the coupling balance of folded chains is further affected by solvent choice and processing conditions. This change in the effective photophysical dimensionality is especially important to consider when engineering donor-acceptor interfaces in device active layers.

### 2-1-3 Conclusion: chain-folding effect on photophysics of P3HT nanofibers

Through a systematic study of wavelength-, time-, and polarization-resolved single nanofiber photophysics and correlation with polymer chain conformation, we have shown that the effective dimensionality of exciton coupling within the nanofiber, along its b- and c-axes, is reduced from quasi-2D (both intra- and interchain coupling) to quasi-

1D (almost exclusively intrachain coupling) as P3HT molecular weight is increased. TEM imaging of nanofibers presented here shows that the nanofiber width becomes constant above 13 kDa molecular weight, indicating that polymer chain folding becomes important as molecular weight exceeds this critical value. Thus, the

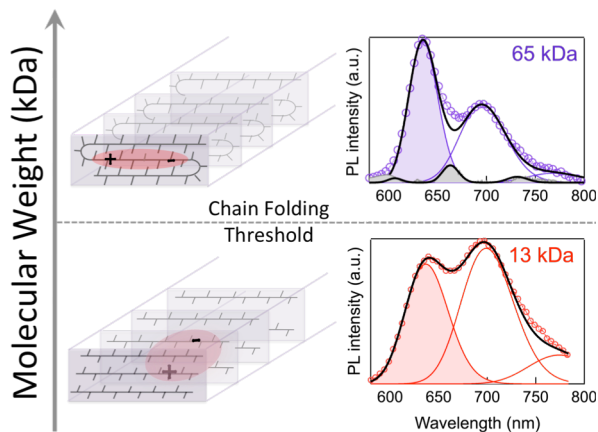


**Figure 2-14: Schematic illustration of molecular weight-dependence of exciton effective dimensionality in P3HT nanofibers. In H-type nanofibers, 13 kDa with extended chain conformation, exciton expands in two dimensions while in J- type nanofibers, 65 kDa NFs with chain folded conformation, exciton is essentially one dimensional.**

photoluminescence signatures of a transition from H- to J-type coupling with increasing molecular weight can be understood as a response to the increased planarization of P3HT backbones and possible misregistration of  $\pi$ -stacked thiophene rings in adjacent lamellar stacks (slip stacking) induced by chain folding within lamellae. Interestingly, the mixed dimensionality can be hidden by conventional PL spectral measurements as evidenced by the comparison of P3HT nanofibers of the same molecular weight (65 kDa) formed from CF/DCM versus toluene. Here, the emission spectra are very similar, and both indicate J-type excitonic coupling, however, the time evolution of polarization contrast are dramatically different, indicating a noticeable mixed H- and J-coupling for the mixed-solvent system.

As discussed in a recent review by Muthukumar and Briseno,<sup>63</sup> the existence of a polymer stem length threshold (folding threshold) has important consequences for crystal packing in all three dimensions. Small changes in the folding threshold could affect thiophene ring registration between adjacent lamellae and consequently  $\pi$ -stacking distance and coupling strength, which greatly affects both the interchain communication and the chain planarity. The predicted consequences of folding threshold changes closely resemble previously observed solvent effects, and therefore, we suspect that the molecular weight folding threshold is solvent-specific. A systematic molecular weight study to determine folding thresholds in different solvents would be ideal for confirming this hypothesis; however, the crystallization of low molecular weight P3HT into nanofibers in different solvents and under many processing conditions is not trivial due to drastic increase in the solubility of low Mn versus high Mn polymers in most solvents. Further computational studies on solvent-dependent molecular weight folding thresholds

and associated crystal- structure-dependent excited state dynamics could provide valuable new insights that are not easily accessible by experiment.

## 2-2 Physics of P3HT nanoparticles within HJ-aggregate framework

P3HT nanoparticles are formed using miniemulsion method by injecting solvated P3HT polymer in organic solvent into an aqueous surfactant solution, followed by sonication, and finally removing the organic solvent by heating. Unlike 1D- crystalline P3HT nanofibers that are formed by well-oriented  $\pi$ -stacked lamellae where extended or folded chains are transverse to

NF growth axis, chain packing in nanoparticles, especially with high molecular weight polymers, is frustrated both kinetically (by trapping into metastable configuration) and spatially where nanoparticle surface curvature might be important. This results to size-dependent internal (aggregate) structure of nanoparticles.

Figure 2-15a shows photoluminescence image of well-separated P3HT nanoparticles on coverglass

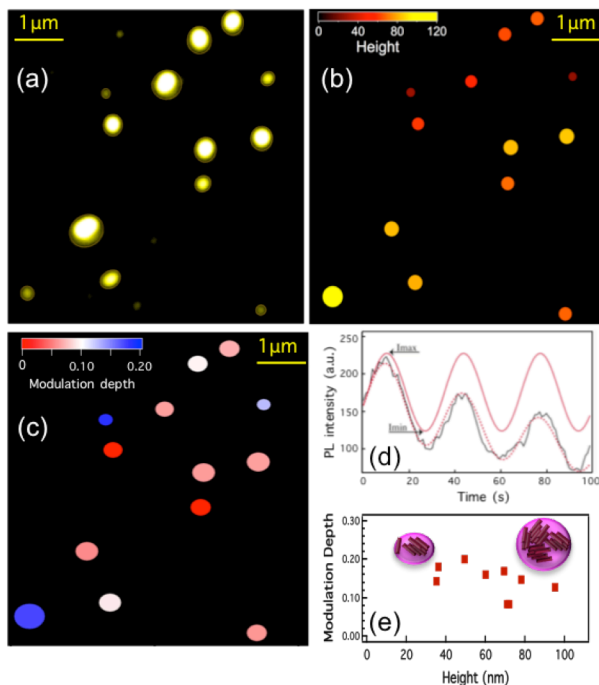


**Figure 2-15: (a) photoluminescence image of individual P3HT nanoparticles. (b) and (c) height values and polarization contrast parameter of nanoparticles, respectively, overlaid on PL image. (d) Linear polarization anisotropy of single nanoparticle (solid black curve), along with the fit curve with and without exponential term (dotted red and solid red curves, respectively). (e) Scatter plot of modulation depth of nanoparticles shown in (a) vs. their height, and schematic illustration of internal structure of small and large nanoparticles.**

that are formed in chloroform and cast from aqueous solution. Size of nanoparticles was measured by simultaneous AFM scanning and was overlaid on the PL image in figure 2-15c indicating a quite large variation in the size of nanoparticles ranging from 40 nm to 120 nm. It also shows that there is no correlation between nanoparticles size and their emission quantum yields.

Molecular transition dipole moment of P3HT chains is parallel to the chain backbone, so the average dipole moment of NPs is representative of chains orientation in their internal structure. The average dipole moment is measured by excitation polarization anisotropy experiment. PL intensity of individual NPs is acquired as the excitation polarization is rotated. The obtained intensity trajectory is then fitted by eq 2 to calculate modulation depth ( $M = (I_{max} - I_{min}) / (I_{max} + I_{min})$ ) as shown in figure 2.15d,

$$F(x) = I_{max}(1 + M \cos^2(Cx + D)) \times \exp(-kx) \quad (13)$$

exponential term is multiplied to exclude NPs photobleaching in measuring polarization contrast parameter (M). The calculated modulation depth of each nanoparticles overlaid on the PL image in figure 2-15c ranges from 0 to 0.2. The scatter plot in 2.15e depicts correlation between modulation depth value and NPs size. The average modulation depth value of NPs is about 0.15 with large nanoparticles (with 80- 100 nm diameter) contributing to the lower tail of M distribution. The overall small value of M indicates that NPs comprise randomly oriented semicrystalline grains. The reason that large nanoparticles contribute to the lower tail of M distribution could be that they consist of multiple semicrystalline regions randomly oriented and surrounded by amorphous polymers, whereas small NPs might consist of most likely one or two semicrystalline

domains surrounded by amorphous component as schematically illustrated in figure 2-15e.

In order to assess molecular packing order and exciton coupling strength in confined polycrystalline P3HTnanoparticles, we examined photophysics of P3HT nanoparticles formed in different solvent, chloroform, toluene, and chloroform/toluene mixed solvent. Figure 2-16a shows the absorption spectra (normalized to the absorbance of the 0-2 vibronic transition) for an aqueous suspension of nanoparticles formed from 0.5 wt % P3HT in chloroform, toluene, and mixed solvent. The TEM measurements show that all three nanoparticle families have round shapes.<sup>55</sup> Similar to nanofibers and thin films absorption spectra, the measured absorption spectra are composed of two parts: a high- energy region that is attributed to amorphous P3HT chains, and a low energy

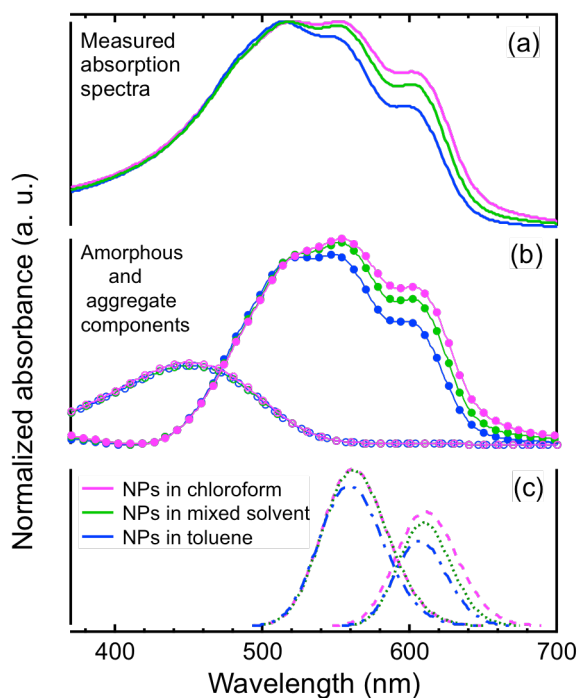


**Figure 2-16: Measured absorption spectra of P3HT nanofibers in chloroform, chloroform/ toluene mixed solvent and toluene (top) and their corresponding amorphous and aggregate component (bottom).**

region that carries the vibronic structure of aggregate P3HT within NPs. Given the fact that P3HT chains cannot be dissolved in aqueous solution and are encapsulated during droplet formation in aqueous surfactant solution indicates that the amorphous absorption is due to unaggregated chains within the nanoparticles, not from free P3HT in the suspension. It is interesting

to note that decreasing solvent quality does not affect the contribution of the amorphous component to the absorption spectra, but does appear to affect the  $A_{0-0}$  to  $A_{0-1}$  intensity ratio. From a decomposition of the absorption spectra into aggregate and amorphous components (by subtraction of an appropriately scaled amorphous P3HT absorption spectrum of a dilute P3HT solution in chloroform from the measured spectrum), we estimated the relative amounts of amorphous and crystalline material for each family of P3HT NPs (figure 2-16b). In P3HT thin-films and nanofibers the contribution of the aggregate component to the total absorption increases as the amorphous component decreases and both change with decreasing solvent quality.<sup>59, 69</sup> In contrast, the contribution of the amorphous and aggregate structural components of the nanoparticle appear to be completely insensitive to the choice of oil phase, but the aggregate contribution to the spectrum tends to decrease with decreasing solvent quality. This indicates the change in the quantum yield of the aggregate species due to the solvent-dependence of the crystal structure. Since NPs from different solvents are made with the same amount of polymer, we can infer that the percentage of unaggregated chains within NPs does not depend on solvent quality. Thus the solvent quality affects the aggregate absorption through changing the crystalline order and not the actual amount of the aggregated chains.

The aggregate spectrum of each nanoparticle families are fitted by a set of Gaussian functions in which relative peak intensities (Huang- Rhys factor), relative peak positions (intramolecular vibration energy), and linewidth (structural inhomogeneity) are treated as adjustable parameters. The Gaussian distribution of absorption origin and its first replica are shown in figure 2.16c. The calculated free-exciton bandwidth  $W$ , using

eq12, presented in Figure 2-17 shows that the average value of  $W$  increases with decreasing solvent quality, however the distribution of  $W$  values is large for both chloroform and toluene formed nanoparticles, and narrow for the mixture. It

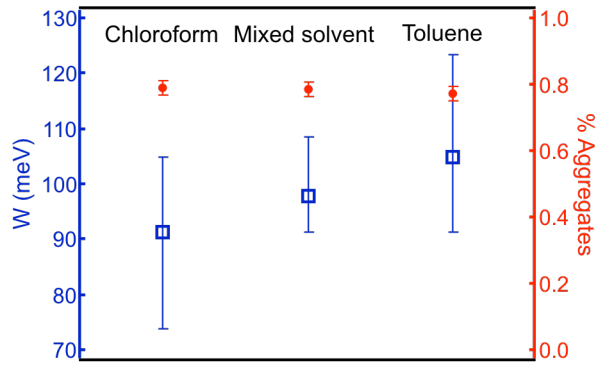


**Figure 2-17: Free exciton bandwidth (blue) and crystal fraction (red) for different solvent compositions.**

is noteworthy that these values of  $W$  lie somewhat in between values seen in P3HT thin-films, although the trend with solvent quality is opposite to that seen in thin films.<sup>69</sup>

Figure 2-18 shows examples of photoluminescence spectra from isolated nanoparticles prepared from

P3HT of different regioregularity (98% vs 92%) with similar molecular weight (31 kDa vs 40 kDa for the lower regio-regular P3HT). It is clear that the spectral composition of P3HT nanoparticle luminescence is almost indistinguishable from that of nanofibers, indicating common structural origins. In this example, a higher

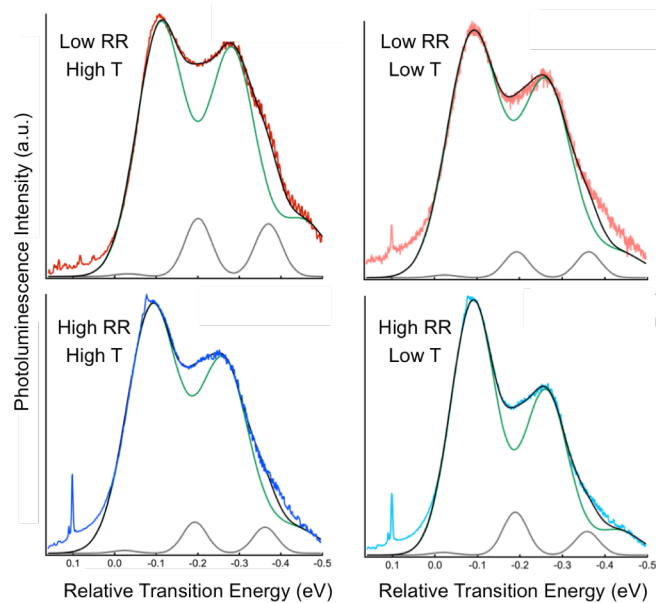


**Figure 2-18: Photoluminescence spectra of isolated nanofibers prepared from high- RR (98%) and low-RR (92%) P3HT under conditions of high-temperature (80°C) and low temperature (60°C).**



temperature is used to drive off the low-boiling solvent, and therefore trapping the polymer in non-equilibrium chain-packing structures. Both spectra show the spectral signatures of H and J aggregate photoluminescence, although the H-type contributions appear to be highly sensitive to regioregularity and processing conditions. In this example, the lower rr nanoparticle gives much stronger PL intensity in the -0.15 to -0.35 eV energy range identified with H-aggregate luminescence, with a smaller origin Stokes shift compared with the corresponding electronic origin for the higher regioregular P3HT nanoparticles. Under conditions of lower temperature self-assembly, the PL spectra indicate more J-like spectral character implying an internal chain-packing structure more closely approximating a minimum energy structure rather than a kinetically trapped state. In these examples, the PL spectra appear more J-like; the H-components of the spectra are still present, but are broadened and significantly attenuated in terms of intensity. Thus, it appears that the J-type coupling is primarily associated with minimum energy polymer packing, while H-type coupling is associated with higher-energy packed states.

## CHAPTER 3

### CROSS-LINKED FUNCTIONALIZED POLY (3-HEXYLTHIOPHENE)

#### NANOFIBERS WITH TUNABLE EXCITONIC COUPLING

The solution-based assembly of crystalline P3HT nanofibers opens new possibilities for controlled inter-facing with n-type materials or surfaces, removes the need for post deposition processing of active layers (i.e., annealing), and can give robust nanostructures of controlled electronic properties.<sup>53, 70-72</sup> However, the inherent fragility of these nanowire assemblies (held together by weak van der Waals interactions) is a key limitation, as it makes transfer, mixing, and resuspension in different solvents problematic. Recently, several groups have explored chemical cross-linking as a means to generate mechanically robust, stable structures for incorporation in solar and optoelectronic devices.<sup>72-74</sup> Polymer cross-linking has been shown to stabilize power conversion efficiencies by minimizing effects of phase-separation in thermal annealing steps of active-layer film preparation.<sup>75</sup> For nanofibers, preserving the pristine aggregate ( $\pi$ -stacking) structure and associated intermolecular coupling is seen as essential for efficient long-range charge-transport.<sup>76, 77</sup> Recently, Park and Grey have shown how to transfer J-aggregate nanofibers encapsulated amphiphilic copolymers for transfer/manipulation in different solvent environments.<sup>78</sup> Emrick and co-workers showed that chemical cross-linking of diblock-copolymer nanofibers formed in solution results in mechanically robust, solvent-agile structures that can be cast, resuspended, and/or mixed with a variety of dopants for optoelectronic applications.<sup>72</sup> Of specific interest here is the extent to which cross-linking perturbs the crystalline aggregate, and how different cross-linking strategies might be used to tune electronic properties via

programmed starting materials and linking agents. Here, we address the question of how different chemical cross-linking affects exciton coupling in isolated nanofibers.

### 3-1 Controlling cross-linking-induced structural perturbation in the cross-linked nanofiber via size of cross-linkage

We started with preformed crystalline nanofibers from two different copolymers of similar molecular weight (15 kDa) and molar block ratio (4:1 P3HT/P3XT monomer ratio) in solution: poly-(3-hexylthiophene)-block-poly(3-methanoltiophene) (P3HT-b-P3MT) and poly(3-hexylthiophene)-block-poly-(3-hexylthioacetate thiophene) (P3HT-b-P3ST). Both diblock copolymers were synthesized in the Emrick's group. P3HT-b-P3MT nanofibers were cross-linked by addition of hexylmethylene diisocyanate (HDI), while P3HT-b-P3ST nanofibers were cross-linked via removal of the acetate and oxidation to form disulfide bonds. For simplicity, we identify each diblock copolymer

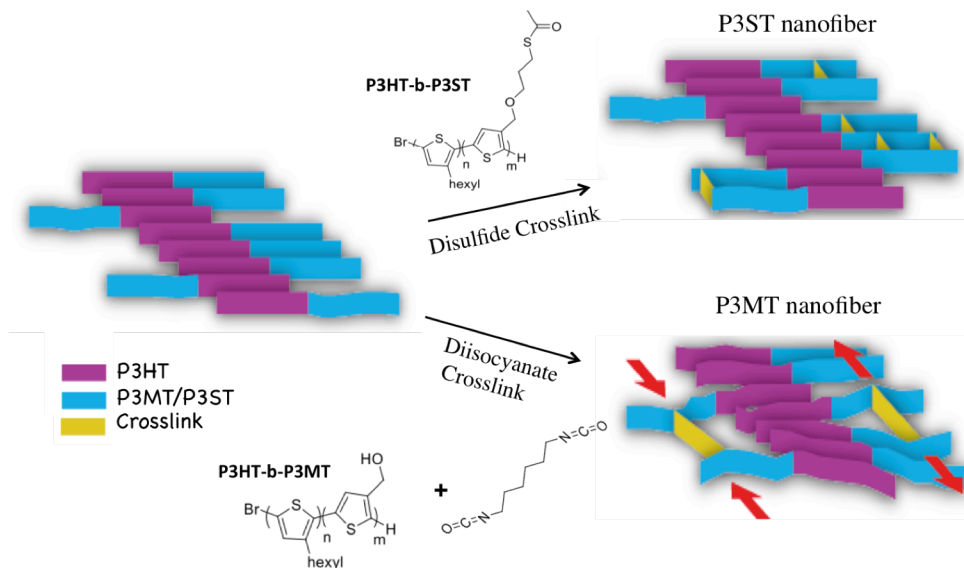


**Figure 3-1: Structural schematic of diblock copolymer nanofiber, P3HT-b-P3ST cross-linked nanofiber, and P3HT-b-P3MT cross-linked nanofiber. The chemical drawing of corresponding diblock copolymers and cross-linkage are also represented.**

nanofiber family by their polymer functional group: hydroxyl nanofibers (P3MT) and thiol nanofibers (P3ST).

Figure 3-1 shows a schematic of diblock copolymer nanofibers along with the two cross-linked nanofiber families and chemical drawing of the corresponding monomer structures and cross-linking agents used in this study.

Low molecular weight polymers were chosen to minimize the possibility of chain folding within the lamellar sheets that occurs when polymer molecular weight exceeds the critical value 13 kDa. Therefore, P3MT and P3ST functional blocks attached to the end of P3HT chains are unlikely to be present in the fiber core, and only decorate its exterior. Thus, cross-linking the nanofibers composed of lower molecular weight polymer avoids potentially deleterious defects associated with higher molecular weight systems.

In addition, it is unlikely that the minority block of the copolymer has any intrinsic effect on the electronic structure, as solution phase measurements of absorption and emission of solvated single diblock-copolymer chains show virtually no change as compared to solvated pristine P3HT, although the chemical modifications of the side

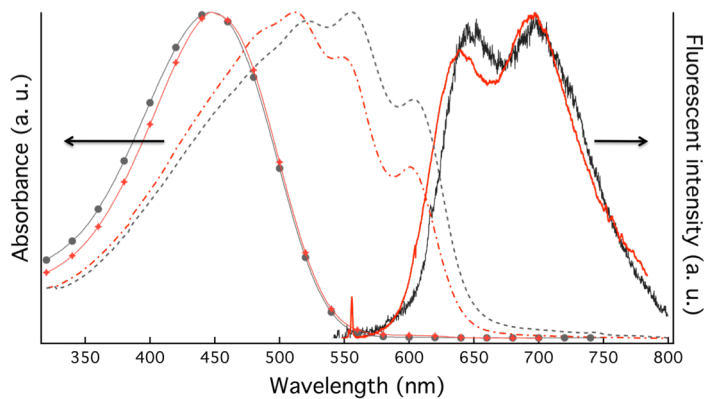


**Figure 3-2: Absorption and emission spectra of 13kDa P3HT (red curves) and 15kDa diblock-copolymer P3HT-b-P3MT (black curves).**

chains can be seen in IR absorption. Figure 3-2 shows absorption and emission spectra of 13 kDa P3HT (red curves) and 15kDa diblock-copolymer P3HT-b-P3MT (black

curves). Solution phase absorption spectra of solvated P3HT and P3HT-b-P3MT chains in chloroform (circled red line and circled black line, respectively) are almost identical indicating that the minority block does not apply any alternation into the electronic structure of P3HT-b-P3MT chains as compared to pristine P3HT polymer. Both solution phase absorption spectra of P3HT and P3HT-b-P3MT nanofibers represent dominant H-aggregate coupling in both nanostructures. However, solid-state emission spectrum of P3HT nanofibers (solid red) with 0-0/0-1 PL intensity ratios less than one signifies slightly stronger interchain electronic coupling compared to that of P3HT-b-P3MT nanofibers emission spectrum (solid black).

Figure 3-3 shows the steady state suspended-phase UV-vis absorption and solid-state photoluminescence spectra of P3MT and P3ST diblock copolymer nanofibers before and after cross-linking. Both diblock copolymer nanofibers have absorption spectra similar to pristine P3HT nanofibers of similar molecular weight. Prior to cross-linking,

the 0-0/0-1 intensity ratios in absorption are characteristic of a weakly coupled H-aggregate.<sup>68</sup> In photoluminescence, the emission spectrum for the P3ST system is essentially unchanged before and after cross-linking, indicating a minimal structural perturbation of the aggregate structure. In contrast, the emission spectra from P3MT

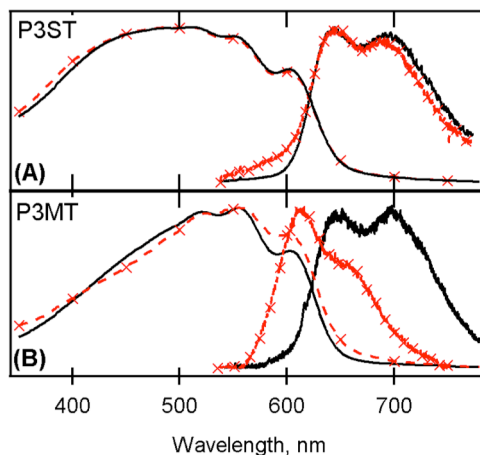


**Figure 3-3: Steady state absorption and emission spectra of (A) P3ST NFs and (B) P3MT NFs before (black) and after (red) cross-linking. Note the significant 40 nm blue-shift on the PL spectrum of the cross-linked P3MT nanofibers with respect to 0-0 origin of P3MT nanofibers despite their almost identical absorption spectra.**

nanofibers change dramatically after cross-linking. The polymer chain packing structure appears significantly altered, as evidenced by a change in the 0-0/0-1 intensity ratios from about 1 to 1.4 and a blue shift of 40 nm in the spectral origin. It should be also noted that the apparent electronic origin at 610 nm for the cross-linked P3MT nanofibers is significantly lower in energy than the corresponding electronic origin of solvated P3HT chains (580 nm), but higher in energy than that in the aggregated film (650 nm). This shift is comparable to that observed for single P3HT chains suspended in a thin film of UHMW polyethylene,<sup>79</sup> despite being in a dense physical aggregate of several hundred nanometers-micrometers in length.

The line shape of the emission spectrum of cross-linked P3MT nanofibers introduces the question of whether interrupted aggregation has changed the dominant chromophore coupling from H to J-type, or simply eliminated any H-type aggregate by perturbing interchain communication. In the latter case, the interchain excitonic coupling would be weakened by the change in the spacing between adjacent polymer chains followed by an increase in the torsional disorder which would cause the PL spectral line shape to look like a J-type aggregate with a much smaller Stokes shift. On the other hand, cross-linking has a negligible effect on the steady state spectra of diblock copolymer P3ST nanofibers, leading us to conclude that cross-linking by oxidation of thiols to disulfide bonds generates minimal structural perturbation and instead locks in the highly aggregated nanofiber structure without causing major interruption in interchain electronic communication.

In the H/J aggregate model, this observed increase in the 0-0 peaks for the P3MT nanofibers implies that the intrachain bandwidth is now larger relative to the interchain

bandwidth.<sup>24</sup> The observed increase in the PL intensity is also likely a result of a relatively larger reduction in the interchain coupling, consistent with the blue-shift in the origin luminescence. If the inter-chain coupling is reduced, then the spectral separation between the higher-energy absorbing state and the lower-energy emitting state caused by interchain coupling is also reduced, causing a blue shift in the emitting state as the band narrows. This picture is also consistent with the observed reduction in the Stokes shift upon cross-linking. While intrachain disorder is likely increased (in the P3MT system) due to a disruption in  $\pi$ -stacking, these measurements show that the associated reduction in the intrachain bandwidth is smaller than the reduction in the interchain bandwidth.

Figure 3-4 shows a comparison of time-resolved PL from the two families of pre- and

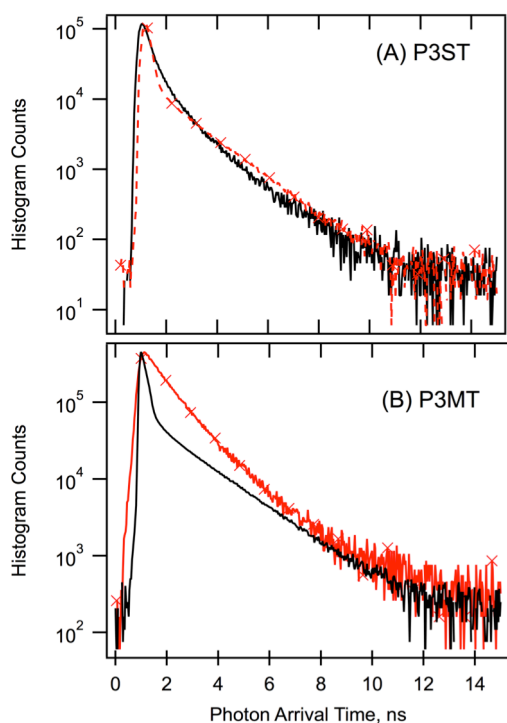


**Figure 3-4: PL Decay traces from 15 kDa P3ST (A) and P3MT (B) diblock-copolymer NFs before (black) and after (red) cross-linking. Note the disappearance of the fast decay component for the P3MT system after cross-linking.**

post-cross-linked diblock copolymer nanofibers. One of the most striking features of the time-resolved photoluminescence of the P3MT cross-linked system is the complete absence of the fast PL decay component, suggestive of disruption of crystalline packing in the nanostructure. In this case, the PL kinetics closely resemble that of isolated P3HT chains in chloroform solution or regiorandom P3HT despite physical aggregation into dense bundles of nanofibers. For

the cross-linked P3ST nanofibers, a minimal effect on the fast PL decay transient indicates yet again that there is no significant change in inter-molecular coupling upon cross-linking. The observed slight decrease in lifetime at very short times might reveal a small increase or a subtle change in electronic coupling.

A fast PL decay component is regarded as one of the characteristic signatures of highly ordered pristine P3HT aggregates and nanofibers, however the mechanism(s) underlying this process remain unclear.<sup>53, 56, 71, 79, 80</sup> In previous measurements in our laboratory, we observed that the fast PL decay was highly polarized along the crystallographic c-axis (transverse to the nanofiber long axis), suggestive of a correlation with a high degree of intra-chain order in these systems. This is supported by measurements on high molecular-weight P3HT nanofibers formed via a thermal crystallization in toluene, which show PL spectra characteristic of J-aggregates as a result of their emission and absorption spectra, which display this extremely fast decay mechanism.<sup>56</sup> Thus, we conclude that the disappearance of the fast decay component in the P3MT cross-linked nanofibers is likely a consequence of the interruption of intra-chain order.<sup>79,71</sup>

### **3-2 Tailored exciton coupling in cross-linked functionalized P3HT nanofibers via solvent annealing**

Cross-linking extended functionalized P3HT nanofibers results in wide variety of morphologies as shown in TEM images in figure 3-5. These extended structures are maintained through resuspending cross-linked nanostructures in different solvents including chloroform, which is a good solvent for P3HT and non-cross-linked P3HT nanostructures are rapidly dissolved in it (figure 3-6). However, the robust cross-linked



hydroxyl nanofibers are not dissolved in chloroform and separate out onto the chloroform surface as shown in 3-5c.

Despite preserved morphological structure during resuspension process, the structural order and therefore exciton coupling strength have been modified. Figure 3-7

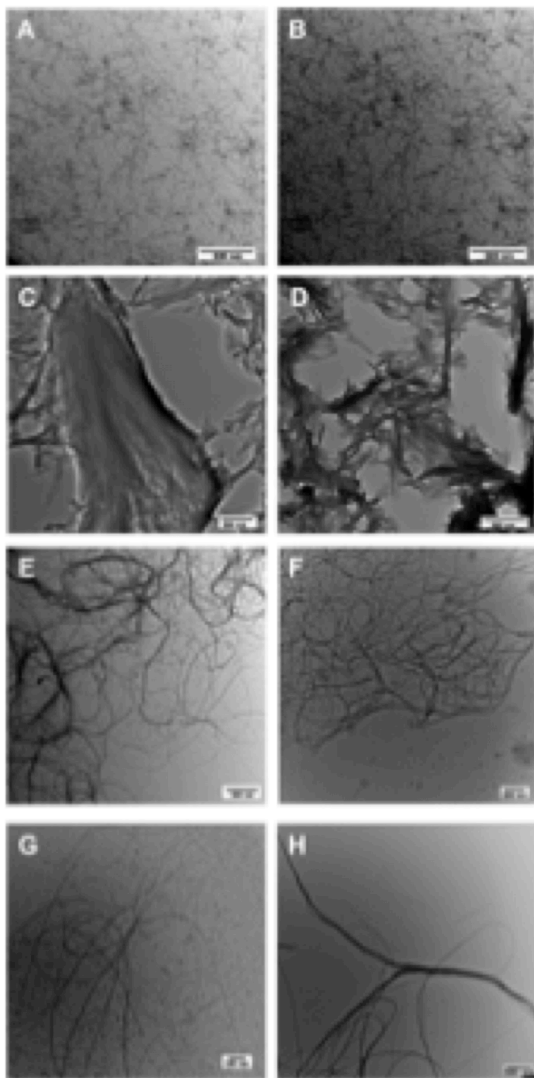


**Figure 3-5: Transmission electron microscopy (TEM) images of different morphologies of cross-linked nanofibers: single cross-linked fibers, bundle of cross-linked fibers, and cross-linked sheets.**

shows the photoluminescence spectra of P3MT nanofibers before cross-linking (in 1:7 CHCl<sub>3</sub>: DCM), after cross-linking (in 1:7 CHCl<sub>3</sub>: DCM), and after cross-linking with solvent exchanged for chloroform (a good solvent for P3HT). Resuspending non cross-linked di-block copolymer nanofibers in chloroform dissolves the nanofiber completely,

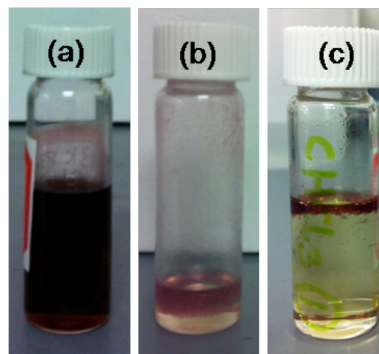


**Figure 3-6: Optical images of (a) P3HT – b-P3MT nanofibers in chloroform/dichloromethane mixed solvent and cross-linked P3HT-b-P3MT nanofibers in (b) mixed solvent and (c) The robust cross-linked hydroxyl nanofibers are not dissolved in chloroform and separate out onto the chloroform surface.**

returning the emission to a 580nm electronic origin. In contrast, PL spectra of cross-linked P3MT nanofibers show not only that aggregation remains in chloroform, but also that suspension in a chloroform bath and subsequent re-casting into a thin film causes an increase in planarity relative to suspension in chloroform-dichloromethane mixed solvent (1:7 volume ratio) evidenced by a 20nm red shift of the PL electronic origin (Figure 3-7a). We believe this structural relaxation is caused by relief of strain imposed originally by cross-linking of non-adjacent block copolymer molecules. Suspension in a good solvent (like chloroform) may allow individual chains to move around within the constraints of their cross-linking to find a thermodynamically more favorable shape, which results in a longer mean conjugation length and resultant spectral red-shift in PL. This effect indicates that the structure within the cross-linked system can still be manipulated somewhat by post-processing, without dissolving the aggregate entirely. This is consistent with the picture of the cross-linked aggregate as a system mechanically constrained only on one edge (the P3MT block side), while the rest of the polymer can still move about. This view is supported by observation of the absorption spectrum of

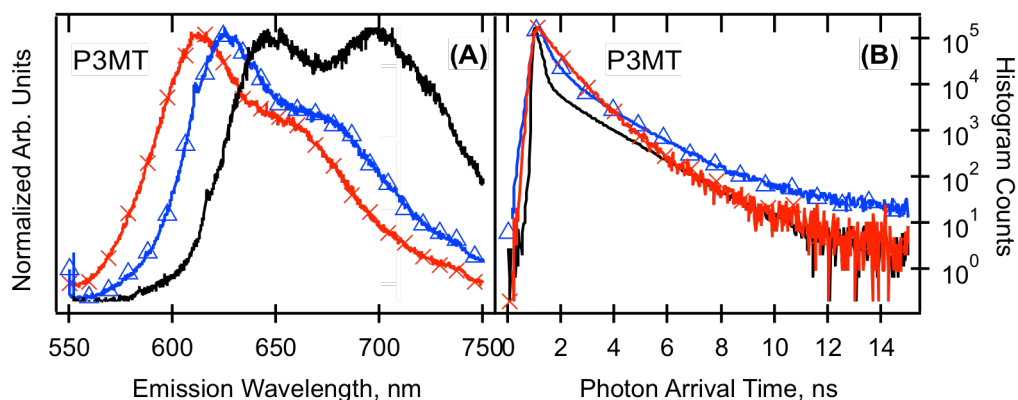


**Figure 3-7: (a) Solvent dependence on the room temperature emission spectra, and (b) PL decay dynamics of cross-linked P3MT nanofibers. PL spectra and decay curves from pre-cross-linked NFs are shown in black, post cross-linked suspended in 1:7 chloroform: dichloromethane (red crosses), and chloroform (blue triangles).**

suspended cross-linked P3MT nanofibers in chloroform, as it shows a strong amorphous component (450nm) despite few or no free polymer molecules in solution, as the liquid phase of the solvent around the cross-linked fiber bundles remains completely colorless. Time-resolved PL transients of cross-linked P3MT show that this ‘solvent-annealing’ process reintroduces some level of inter-chain aggregation, as the fast component of the decay is restored almost completely (Figure 3-7b).

### **3-3 Conclusion**

Interestingly, although the suspended-phase absorption spectra of both nanofiber families before and after cross-linking are identical, the nanofiber photoluminescence spectra show a strong dependence on the choice of linker and solvent, where the changes in the 0-0 origin and relative intensities of vibronic sidebands indicate significant variations in exciton coupling. In the cross-linked P3MT nanofibers, time-resolved photoluminescence reports the absence of a fast PL decay component usually associated with crystallinity, in contrast to cross-linked P3ST nanofibers. The observed differences in photophysical properties between the two cross-linked nanofiber families are mostly owing to the size of the cross-linkage: In the case of P3MT, the cross-linking group that connects polymer chains is longer than the combined hexyl groups of the P3HT structure. Therefore, the linker could react with methoxy groups on the P3MT block on either adjacent or non- adjacent sheets, resulting in a combined pushing or pulling on the P3HT blocks that disrupt the crystalline packing, thereby weakening both intra- and interchain exciton couplings. In contrast, for the P3ST system, the spatial extent of the cross-linker is commensurate with the inter-lamellar spacing, resulting in a mild (if detectable) perturbation in the P3HT aggregate structure. These combined results demonstrate both

physical robustness and electronic tunability in this important class of nanoscale electronic materials.

We are currently exploring the use of intermediate-length linkers to reliably induce more subtle changes in coupling, rather than the gross differences reported above. The ability to lock in conjugated polymer structures of interest in photovoltaic devices before or during the mixing of donor and acceptor (or multiple donor, etc) without compromising nanostructure integrity represents a new and potentially useful tool for optimizing solar cell performance. This cross-linking process removes the need for all structures to be kinetically stable at every step during device fabrication - which may include immersion in several solvents, thermal annealing, and bombardment by reactive metal vapor for electrode deposition. We have also shown that the structures formed via cross-linking can be 'programmed' with particular levels of strain-induced disorder, and subsequently annealed via facile solvent processing. This may be useful for engineering cascades of aggregates without resorting to complicated chemical synthetic procedures, or modification of the surface or particular parts of the device with the introduction of small amount of solvent.

## CHAPTER 4

### THE EFFECT OF POLYMER CHAIN CONFORMATION ON THE OPTOELECTRONIC PROPERTIES OF P3HT NANOSTRUCTURES: A KELVIN PROBE FORCE MICROSCOPY STUDY

The performance of organic based photovoltaic devices depends on efficiency of three successive processes following light-induced exciton formation in donor components: exciton migration in the donor, charge separation at the donor-acceptor interface, and charge transfer across the interface. The exciton migration and charge separation efficiencies are strongly sensitive to the molecular packing of the donor.<sup>1</sup> However, the efficiency of the charge transfer crucially depends on the large area of donor-acceptor interface and the relative frontier energy levels of donor and acceptor. In fact, power conversion efficiency (PCE) of polymer solar cells is directly proportional to the difference between highest occupied molecular orbital (HOMO) level of electron donor component and lowest unoccupied molecular orbital (LUMO) level of electron acceptor.<sup>81</sup> Therefore accurate measurement and tuning frontier energy level of organic materials are necessary for assessing viability of new materials and optimizing device performance.<sup>2, 82</sup>

The HOMO energy level of P3HT is estimated to range between -5.2 and -4.8 eV, from an SCLC analysis of hole only thin film devices,<sup>83</sup> Cyclic voltammetry,<sup>84</sup> photoelectron microscopy,<sup>85</sup> ultraviolet and (angle-resolved) X-ray photoelectron spectroscopy (UPS and AR-XPS),<sup>86</sup> and kelvin probe force microscopy under either vacuum or ambient conditions.<sup>82, 87-89</sup> This disparity in the HOMO value of P3HT is attributed to the variation in the molecular packing that critically depends on polymer

properties and processing conditions. The HOMO value of P3HT thin films is shown to be a complicated function of regioregularity, molecular weight, and processing conditions such as annealing temperature, spin cast rate and so on.<sup>86</sup> This illuminates additional advantage of using nanostructures as building blocks of binary OPVs to thin film morphology. Given the insight on nanofibers molecular packing and chain conformation achieved by photoluminescence probes, we have utilized kelvin probe force microscopy to measure their surface potential aiming to address the question of how chain packing conformation in individual P3HT nanofibers and in general aggregates influences HOMO energy level.

Kevin Probe Force Microscopy (KPFM) is a scanning probe technique that measures the local surface potential contrast (SPC) between a metallized cantilever tip and sample.<sup>90</sup> It has been extensively utilized to measure the surface potential of organic nanostructures, and estimate the work function alternation of active layers at the donor-acceptor interfaces due to charge transfer<sup>88, 89, 91, 92</sup>. Figure 4-1 shows the schematic of KPFM setup. Here the electrostatic potential difference between tip and sample is

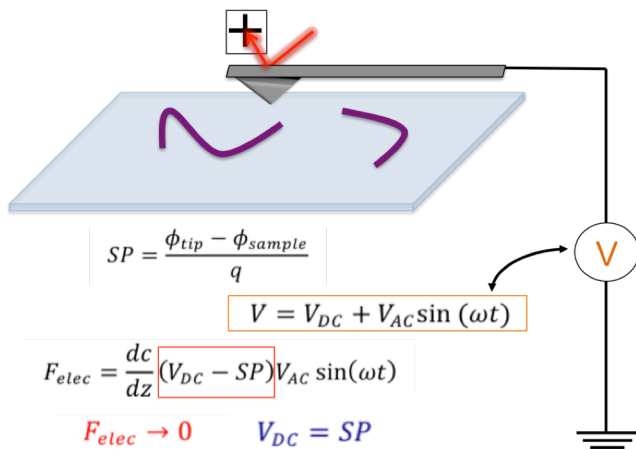


**Figure 4-1: Schematic illustration of kelvin probe force microscopy setup.**

approximately given by  $SP = \frac{\phi_{tip} - \phi_{sample}}{q}$ , where  $q$  is the charge constant and  $\phi_{tip}$  and  $\phi_{sample}$  are the work-functions of the tip and sample, respectively. In our imaging mode, the SPC is measured by applying an AC voltage and DC offset to the

cantilever tip to generate an oscillating electrostatic force between the tip and the sample. The feedback loop system provides a DC offset potential to match the surface potential that minimizes the electrostatic interaction between the tip and sample. The DC input that is used is recorded as the measured surface potential. Thus, the measured SPC can report quantitatively on the HOMO energy location of the sample, provided the work function of the tip is known. For P3HT nanostructures, KPFM can yield precise spatial maps of HOMO energies that can then be correlated with structural order implied from spectroscopic measurements.

I conducted KPFM measurements with an Asylum Research AFM and used MFP3D software to run the Kelvin probe module. All measurements were made in non-contact tapping mode, under ambient atmospheric conditions. The AFM probes were platinum coated silicon probes (ANSCM-PT) used as supplied by *App Nano* with tip diameter of 10nm. As typical in electrostatic force measurements, KPFM imaging employs a trace and retrace over a scan line to first obtain topography information, then lift and maintain a constant height above the sample surface to trace and retrace the same scan line to obtain SPC information. All imaging experiments used a 50 nm initial lift height (adjusted in the Nap mode settings in the MFP3D software); depending on the overlap between the trace and retrace scan lines of the surface potential image, the lift height was reduce to about 10-20 nm above the van der Waals attractive regime. Scan rates were also lowered to  $\approx 0.2$  Hz to improve the resolution of the CPD images by allowing the cantilever to settle on an accurate surface potential value.

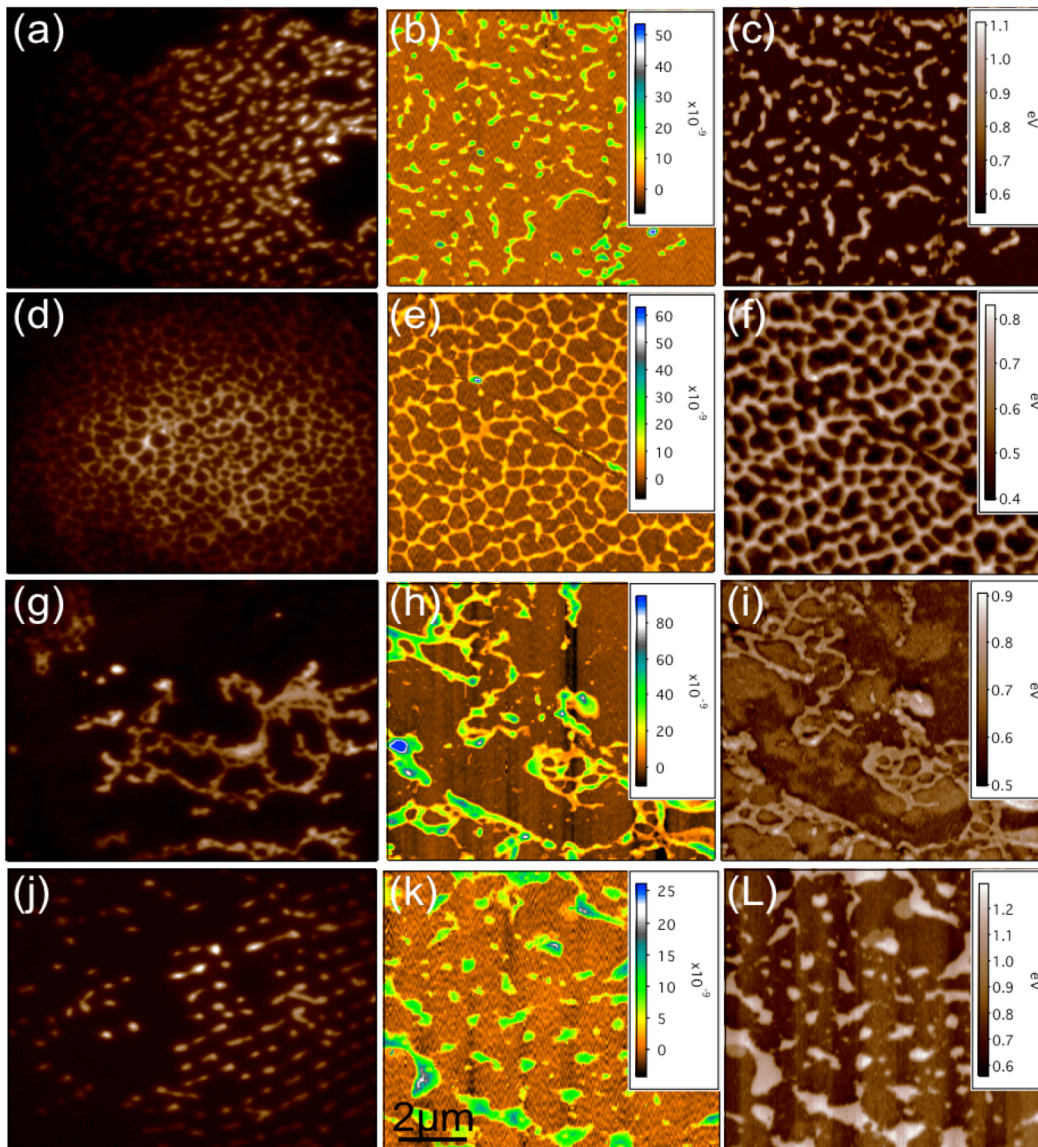


**Figure 4-2: Photoluminescence images of P3HT nanostructure cast from chloroform on cover glass with (a) 55% rra and 75 kDa MW, (d) 75% rr and 55 kDa MW, (g) 98% rr and 65 kDa MW, (j) 98% rr and 13 kDa MW. The corresponding topography (b, e, h, k) and surface potential (c, f, i, l) images of PL photos are shown on their right side.**

#### **4-1 Regioregularity and molecular weight effect on HOMO energy of P3HT**

Figure 4-2 shows photoluminescence images of extended P3HT nanostructures with various molecular weights and regioregularities: 55%rr and 75kDa (a), 75%rr and 55kDa (d), 98%rr and 65kDa (g), and 98%rr and 13kDa (j). The nanostructures are



formed by drop casting of highly diluted P3HT solution in chloroform (about  $5\text{mg l}^{-1}$ ) on cover glass.

We used cover glass as substrate to have optical access to structures from the bottom to correlate photophysical properties of these extended nanostructures with their size and their local surface potential. Prior to drop casting, a two-step cleaning treatment was performed on float cover glasses to remove both contamination and any possible stray charges off the substrate.<sup>93</sup> The float glasses were soaked in piranha solution, a mixture of sulfuric acid ( $\text{H}_2\text{SO}_4$ ) and hydrogen peroxide ( $\text{H}_2\text{O}_2$ ) with 1:1 volume ratio. After washing off the cover glasses by deionized water, it was soaked in dilute aqueous sodium hydroxide solution ( $\text{NaOH}$ ) for one minute to neutralize residual acidity and remove any charge residues off the surface. The float glass was then rinsed by deionized water and dried with air.

The topography and surface potential of nanostructures are represented next to their corresponding PL images in figure 4-2. Similar to the observations of Liscio and coworkers<sup>89</sup> we observed a network of nanowires. The 55%rr (regiorandom) and 75%rr (low regioregular) nanowires have height ranging from 3 to 20 nm (b and e) from drop-cast films. The 98%rr (high regioregular) P3HT nanowires' height is between 1 to 80 nm (h). The thickness of nanowires with high regioregularity (h) is not as uniform as the thickness of nanowires in (b) and (e). Drop casting of low molecular weight polymer with high regioregularity features nanostructures with various lateral sizes and height of 3 to 25 nm. However, surface potential images of nanostructures indicate a small variation in the SP value with the shape of nanostructures within each family. The average measured surface potential of floating cover glass is about  $0.6\pm 0.05$  eV.

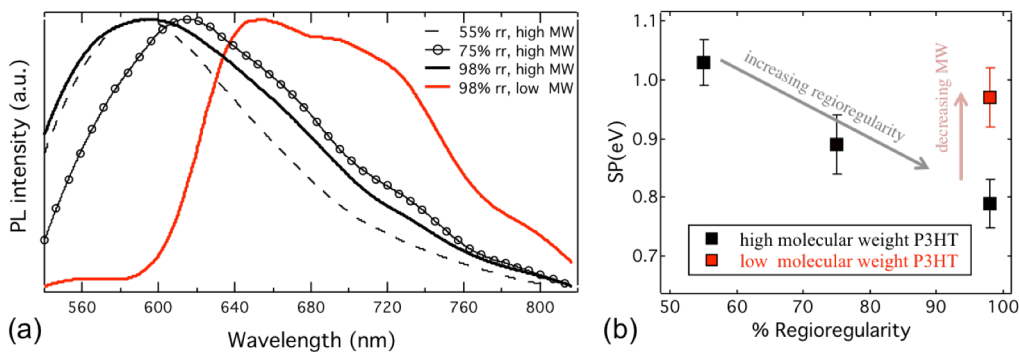


**Figure 4-3: (a) PL spectra of P3HT nanostructures with different regioregularities and molecular weights: 55%rr and 75 kDa (black dashed line), 75% rr and 60 kDa (open black circles), 98% rr and 65 kDa (solid black line), and 98% rr and 13 kDa (solid red line). (b) The corresponding averaged measured surface potential of nanostructure in (a) as a function of regioregularity. The black and red squares denote the high and low molecular weights, respectively.**

Figure 4-3a depicts corresponding photoluminescence spectra of P3HT nanostructures shown in figure 4-2. The broad PL spectra of high molecular weight drop-cast nanowires do not have any distinguishable vibronic features and resemble PL spectra of solvated P3HT chain in chloroform<sup>94</sup>. The maximum emission of these broad PL spectra is at 605, 580, and 580 nm in 55%rr, 75%rr, and 98%rr P3HT, respectively. Given the insight on molecular-dependence of chain conformation provided in Chapter 2<sup>95</sup>, we believe that long polymer chains in drop-cast nanowires are strongly entangled<sup>10, 45</sup> leading to the amorphous (largely disordered) microstructures. This leads to insignificant exciton coupling between molecules in high MW nanowires as is evident from broad PL spectrum peaked at 580nm. On the other hand, the PL spectrum of low molecular weight drop-cast nanowires (red solid line) is red shifted and develops a vibronic progression with PL origin at 640 nm indicating crystalline phase of their structures. The broad vibronic transition bandwidth is due to a large heterogeneity of the nanowire structures. It indicates that the short chains are not entangled<sup>45</sup> and loosely

packed in lamellae leading to the semicrystalline morphology in the drop-cast low-MW nanowires.

Even though the PL spectra of high-MW nanowires (amorphous features as indicated by PL spectra) with random, low, and high regioregularity are quite identical, their surface potential is strongly sensitive to the regioregularity as it is depicted in figure 4-3b. It is interesting that the surface potential of amorphous features reduces from 1.05 eV to 0.8 eV as regioregularity of long chains increases from 55% (rra) to 98% (high-rr). The HOMO energy level of nanofeatures can be calculated by subtracting the work-function of the kelvin probe tip from the measured SP value,  $\text{HOMO} = \text{SP}_{\text{measured}} - \text{WF}_{\text{tip}}$ . It shows that the observed decrease in the SP value with increasing regioregularity is associated with decreasing HOMO energy level of high-rr amorphous nanofeatures. Indeed, considering the similar PL spectra of random, low-rr, and high-rr amorphous nanofeatures, the regioregularity-induced shift in HOMO energy level might be attributed to subtle differences in the structural order of amorphous nanofeatures. Regiorandom chains (half- random mixed with head-to-head and head-to-tail) tend to irregularly pack and suffer a large torsional disorder with inter-chain spacing of about 4-4.5 °A measured from wide angle X-ray diffraction patterns at room temperature.<sup>10, 96</sup> Increasing regioregularity improves self-organization of chains by keeping chains backbone within the lamellar sheets via  $\pi$ - $\pi$  stacking. This results in lower inter-chain spacing of high-rr nanowires, 3.8°A, compared with rra-structures.<sup>1</sup> It is worth mentioning that the decrease in interchain spacing at high-rr nanofeatures enhances the transfer integral value along the chains and subsequently increases ionization energy measured via UPS and AR-XPS methods.<sup>86</sup> The increased ionization energy is equivalent to reduced HOMO energy level.

However, the alternation in interchain spacing might not be sufficient to recover the excitonic coupling in the amorphous nanostructures resulting in subtle changes in their wavelength-resolved spectrum with regioregularity.

On the other hand, decreasing molecular weight of high-rr polymer from 65kDa to 13kDa increases the SP value from 0.8meV to 0.96meV (red square in 4-3b). This rather unintuitive observation of elevated HOMO energy level in high-rr semicrystalline nanostructures is accompanied by an increase in structural order as evidenced by PL spectrum with emission origin at 640nm, red line in figure 4-3a. The enhanced HOMO level could be attributed to an alternation in the chain conformation from strongly disentangled chains, in high-MW amorphous nanostructures, to configuration in which each chains comprise of one or several planarized segments separated by additional coiled segments.<sup>47</sup> The striking changes in the HOMO of amorphous and semicrystalline nanostructures with molecular weight proves that chain conformation is a decisive factor in determining and tuning not only the exciton coupling strength<sup>95</sup> but also the frontier energy level of aggregates.

#### **4-2 Correlation between P3HT chain conformation and HOMO energy level**

To further understand how chain conformation in nanostructures affects the HOMO of P3HT, we conducted KPFM measurements on two extreme cases: low-MW crystalline nanofibers with extended chain conformation and high-MW crystalline nanofibers with fully folded conformation. This measurement will also indicate that to what extent the variation in crystalline order and the dominant exciton coupling alters HOMO energy level.

Figure 4-4 shows height and surface potential images of well-separated high-rr crystalline nanofibers with low- and high-MW, that are cast on piranha-treated cover glass. KPFM measurements (a and d) indicate lower average SP value for low-MW crystalline nanofibers

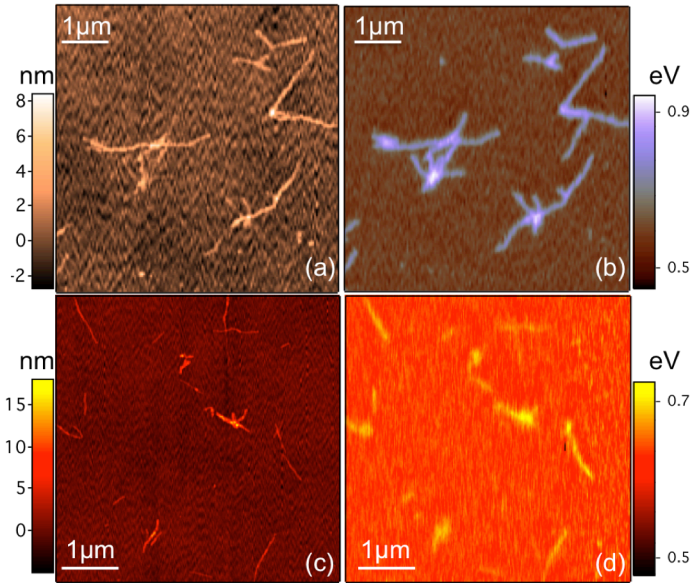


**Figure 4-4: Height and surface images of High molecular weight nanofibers (a,b) and low molecular weight nanofibers (c,d) cast on cover glass.**

of about  $0.66 \pm 0.03$  as compared with high-MW crystalline nanofibers with SP value of about  $0.85 \pm 0.07$ . The average width of 13 kDa and 65 kDa crystalline NFs are 14 and 17 nm, respectively, measured from the TEM images, shown in figure 2.10. We know that the tip convolution artefacts in SPM technique become critical when the lateral size of the investigated object is comparable to the tip diameter.<sup>97</sup> In fact, the measured surface potential of nanostructures in non-contact KPFM is a weighted average over so-called an effective area of the surface that is interacting with the tip through long-range electrostatic field. Thus, the kelvin probe signal is a linear convolution of an effective surface potential and microscope point spread function. The point-spread function can be calculated based on measuring the tip shape. Different deconvolution methods have been developed to reconstruct the KPFM images aiming to restore the actual SP value of the nanostructures.<sup>89, 98-100</sup> We realized that deconvolving the KPFM images in figure (b) and

(c) will only change the SP value of NFs from 5 to 10%, depending on their height, within each family. Therefore, the observed difference in the average SP value of about 200 meV between 13 kDa and 65 kDa crystalline nanofibers is concrete. It is quite surprising that decreasing molecular weight in solution-based crystalline nanofibers results in a decrease in the SP value, and thus lowers HOMO energy level, contradictory to the molecular weight-dependence of HOMO levels of drop-cast nanowires.

The surface potential of 13 kDa crystalline nanofibers and drop-cast 13kDa nanowires are compared at various heights in the 2D scatter plot of figure 4-5a. The scatter plot shows no obvious correlation between the SP value and the corresponding height in neither of the families. In addition, it indicates that the surface potential of crystalline nanofibers (red circles) has a narrow distribution with average value of 0.66

eV that is about 0.3 eV smaller

that the average surface

potential of its counterpart

(gray circles). Considering the

fact that short polymer chains

possess extended conformation

in lamellar sheets, fibrilizing

13kDa polymer chains in

chloroform/DCM mixed

solvent under thermal

equilibrium condition results in

chain planarization, superior

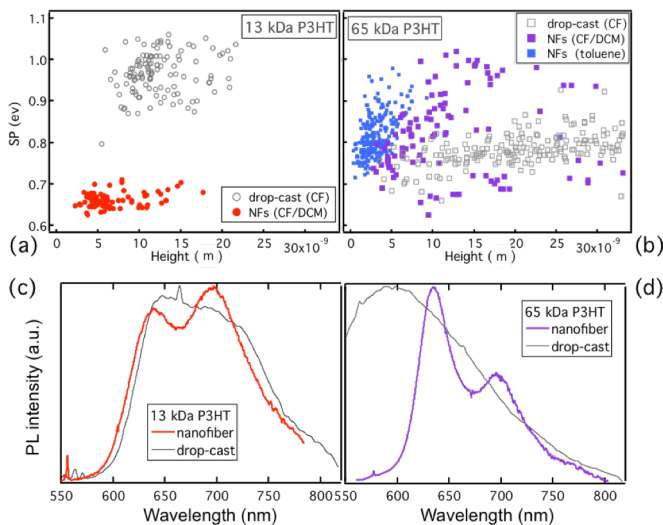


**Figure 4-5: Two- dimensional scatter plot of surface potential of low (a) and high (b) molecular weight P3HT nanofibers and nanowires and their height. In both graphs gray markers are drop-cast nanowires and colored markers are crystalline nanofibers. (c, d) The corresponding PL spectra of drop-cast nanofeatures and crystalline nanofibers with low and high molecular weights, respectively.**

molecular order, and thus strong interchain coupling as compared with drop-cast nanowires in which aggregation is driven by solvent evaporation. This is manifested as a decrease in the 0-0 to 0-1 PL intensity ratio and narrower vibronic transition bandwidth of 13kDa nanofibers relative to the PL spectrum of 13kDa drop-cast nanowires (figure 4-5c). Therefore, we surmise that in the low molecular weight regime modifying molecular packing order might recover thiophene ring registration in adjacent lamellae and improve intermolecular charge distribution. This results in the enhanced wave function overlap between their frontier orbitals leading to stronger interchain coupling, evidenced by a decrease in the 0-0 to 0-1 PL intensity ratio,<sup>101</sup> and reduced HOMO energy level.

Figure 4-5b shows 2D scatter plot of 65kDa crystalline nanofibers, formed from toluene (blue square) and CF/DCM mixed solvents (purple square), and 65kDa amorphous features (gray square). The scatter plot indicates that there is no correlation between the height and surface potential of high molecular weight features. Moreover, it shows that the 65kDa crystalline nanofibers have almost the same average SP value (about 0.81eV) that is about 0.02eV larger than that of the 65kDa amorphous nanofeatures. Size correlated PL spectroscopy study in chapter 2 showed that the high regioregular 65kDa nanofibers possess folded chains in the lamellar sheets with high order of chain planarity and have dominant J-aggregate coupling, where as high regioregular 65kDa nanofeatures comprise of strongly entangled chains that form aggregates with amorphous PL characteristics. However, in both folded and entangled conformation there would possibly be weak thiophene ring registration (slip-stacking) in the subsequent  $\pi$ -stacked lamellae. Therefore, enhanced chain planarization in crystalline NFs compared with amorphous nanofeatures would mostly develop transfer integral

between frontier orbitals of neighboring thiophene rings in the same chain and alter intramolecular charge distribution. This will strengthen intrachain exciton coupling, evidenced by large 0-0 to 0-1 PL intensity ratio and narrow transition bandwidth of 65kDa nanofibers (figure 4-5d). In addition, this appears to give rise to the minor increase (about 0.025 eV) in the HOMO level of 65kDa nanofibers with respect to 65kDa amorphous nanostructures.

It is quite interesting that improving molecular order in 13kDa and 65kDa P3HT nanostructures changes their surface potential, and effective position of HOMO, in opposite directions. In high-MW regime with either folded or entangled chain, modifying intramolecular charge distribution, which is dominant coupling, raises HOMO energy level. But, in low-MW nanostructures with comparable inter- and intramolecular coupling strength, intermolecular charge distribution appeared to be more sensitive to the structural order and reduces HOMO energy level. Indeed, our results show that the correlation between electronic properties and morphology strongly depends on the chain conformation in the aggregates.

#### **4-3 Morphology-Dependent Surface Potentials in Cross-linked P3HT Nanostructures**

Cross-linking P3HT chains of neighboring lamellar sheets has been suggested as a reliable method to produce mechanically and chemically robust nanostructures from preformed crystalline P3HT nanofibers.<sup>72</sup> However, the cross-linking induced structural perturbation of P3HT nanofibers results in a variety of different nanostructural morphologies, as shown by TEM images in figure 3-5. Here, I conducted KPFM measurements using P3HT-b-P3MT cross-linked nanostructures as prototype materials to



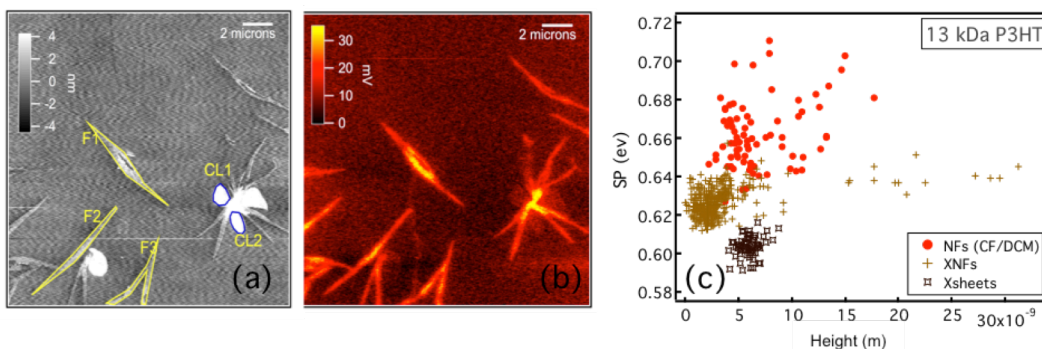


**Figure 4-6: Topography (a) and surface potential (b) images of cross-linked P3HT-b-P3MT nanofibers cast from CF/DCM representing various morphologies of cross-linked nanostructures such as fibers (F) and cloverleaf (CL) or sheets. (c) 2D Scatter plot showing the SP of cross-linked nanofibers (XNFs), cross-linked sheets (Xsheets) and 13 kDa P3HT nanofibers and their height.**

assess to what extent the cross-linking-induced structural perturbations affect the electronic properties such as surface potential.

Figure 4-6a and b show the topography and surface potential images of P3HT-b-P3MT cross-linked nanostructures on piranha treated cover glass. The topography image depicts a variety of different nanostructural morphologies including single or bundled cross-linked nanofibers (F), and “clover-leaf” sheets (CL). The corresponding surface potential contrast (SPC) image on the right shows spatial variation of SPC values along the NF axis in cross-linked fibers; higher SPC values are located in the center and lower SPC values are located near the edges. The color bar indicates the relative SP value with respect to cover glass with SP value of  $0.6 \pm 0.05$  eV. The SPC image also shows that the “clover-leaf” sheets have a near-zero surface potential (relative to glass). The 2D scatter plot of surface potential and height of the two designated features in figure 4-4a, cross-linked nanofibers (light brown) and cover-leaf (dark brown), is shown in figure 4-4c. For comparison we have included the pre cross-linked nanofibers (red circles) in the figure that illustrates an overall decrease in the surface potential of nanostructures through the cross-linking process. The strongly diminished interchain coupling evidenced by

wavelength- and time-resolved photoluminescence imaging (figures 3-3 and 3-4) accompanies the reduction in the SPC. The Bout group has reported similar morphology effects on electronic properties of oligothiophene nanostructures, in which the decrease in the local contact potential of nanostructures with different morphologies is attributed to the increase in the amount of energetic disorder in the aggregate.<sup>102</sup> They showed that subtle morphological changes in particle shape and molecular packing result in redistribution of charges within or between thiophene rings, and accordingly change the electronic properties. Correlating optical and electronic properties, they showed that the decrease in the SPC of nanostructures is associated with a decrease in interchain coupling strength. This is evidenced by the reduced 0-0 vibronic band intensity of the emission spectrum. Consistent with their study, monitoring cross-linking induced changes in the optical and electronic properties of P3HT nanofibers illustrates a full picture through which structural perturbation can be explained: interrupted lamellar spacing in cross-linked aggregates demolishes interchain coupling. This restricts the charge distributions mostly to individual extended chains in cross-linked nanostructures, in lieu of the two-dimensional (intermolecular and intramolecular) charge distribution seen in pre-cross-linked nanofibers. As a result, despite being in the aggregate, extended chains of cross-linked nanostructures do not effectively interact with each other and thus possess similar optical and electronic properties to solvated polymer chains. This is evident from their 30nm blue shifted PL origins (peaked at 610nm) and reduced SPC value from 0.66 in low-MW nanofibers to 0.62 eV. Assuming the tip work function to be 5.5eV places the nominal HOMO level of cross-linked nanofibers at -4.84eV. This value falls within the

range of reported HOMO energy level of solution phase P3HT in toluene and chloroform (between -4.84 to -5.2) determined from cyclic voltammetry measurements.<sup>103, 104</sup>

Moreover, the scatter plot reveals a morphology-dependence of surface potential, equivalently effective HOMO level, in cross-linked nanostructures. In fact, the average SPC value of cross-linked nanosheets is about 0.025eV, less than that of cross-linked nanofibers. The distinguishable electronic properties of different cross-linked morphologies is possibly due to the subtle variation in their molecular packing densities and indicates that their geometrical heterogeneity is correlated to heterogeneity on the molecular packing scale.

#### 4-5 Conclusion

KPFM measurements have revealed an interesting dependence of surface potential contrast (SPC) with P3HT nanostructure morphology. In comparing SPC of P3HT nanostructures with different molecular weights and regioregularities, we found that the correlation between the amount of disorder present in the aggregate and electronic properties strongly depends on the chain conformation in the aggregates. Figure 4-7 shows

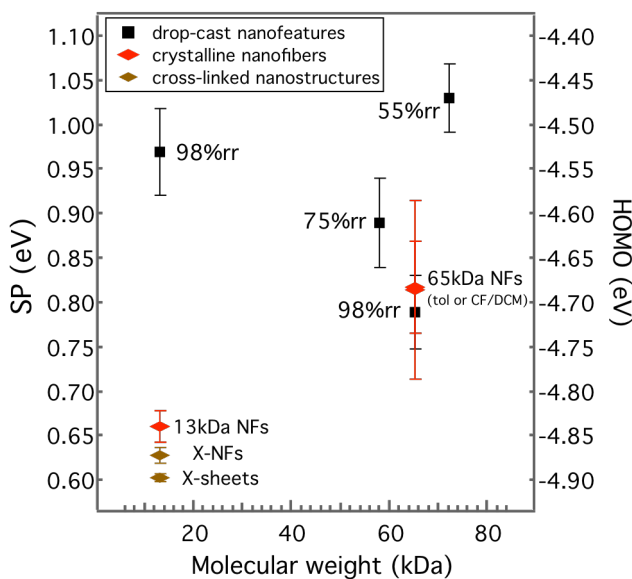


**Figure 4-7: Surface potential and associated HOMO energy diagram of drop-cast nanowires (black squares), crystalline nanofibers (red diamond), and cross-linked nanostructures (brown diamond) as a function of molecular weight.**

the SPC and the corresponding effective position of the HOMO levels of different nanostructures as a function of molecular weight. In the high molecular weight regime, nanostructures with high regioregularity have the lowest HOMO levels. Improving molecular order in the high molecular regime slightly elevates HOMO levels of the resultant structure, whereas enhanced molecular order in the low molecular weight regime results in a considerable decrease in the HOMO levels. Correlating PL properties with SPC measurements, we showed that the observed disparity in the correlation between morphology and electronic properties in the two regimes is due to the difference in chain conformation between the nanostructures: folded or entangled chain conformation in the high-MW vs. extended chain conformation in the low-MW regime. In the high-MW regime, interchain coupling within aggregates is negligible, possibly due to thiophene ring miss-alignment between adjacent lamellar sheets in p-stacks. This miss-alignment is possible for both entangled and folded conformations of long chains. Therefore, the difference in high-MW morphology between amorphous nanofeatures and crystalline nanofibers results in an improvement of the intramolecular charge distribution. On the contrary, within an extended chain conformation, inter- and intra-molecular coupling are comparable, and improving molecular order increases inter-molecular charge distribution more than its counterpart, as evidenced by changes in the PL spectra. These results indicate that changes in the structural order are positively correlated with HOMO level energies in structures with effective one-dimensional excitonic coupling, and are negatively correlated in effectively two-dimensional structures. Moreover, we recognized that the cross-linked aggregates show optical and electronic properties that are analogous to solvated chains because of their perturbed interchain coupling. We believe

the results presented in this chapter provide new insights into polymer morphology “design rules” for optimizing OPV device performance.

## CHAPTER 5

### NEAR FIELD SCANNING OPTICAL MICROSCOPY & FUTURE WORK

Resolution of diffraction- limited optical microscopy is a key constraint when studying nanostructures and inspecting high spatial resolutions. Light rays spread out when they propagate from point sources resulting in diffraction patterns at distances larger than light's wavelength. This reduces the resolution of a detector that is located in the far field, unless it is wide enough to collect all the diffracted light. Rayleigh criterion,  $d = 0.61 \frac{\lambda}{NA}$ , indicates that the minimum resolution (d) of far-field optical microscopes is determined by the wavelength of the incident light and by the numerical aperture (NA) of the condenser and objective lens of the system. Hence, utilizing the maximum aperture size ( $\sim 1.3$ - $1.4$ ) of modern objectives gives the resolution of around  $\frac{\lambda}{2}$  for a conventional optical microscope ( $\sim 200$ - $300$  nm resolution using visible light sources).

Near-field scanning optical microscope (NSOM) is a scanning probe microscopy method that combines atomic force microscopy and optical techniques in order to enhance Abbe's diffraction-limited resolution by utilizing evanescent field.<sup>105-107</sup> It is conceivably the most powerful SPM technique to investigate nanostructure surfaces with high spatial resolution without extreme specimen preparation requirements that are necessary for the other high-resolution SPM methods.

To go beyond the diffraction limit, NSOM employs the evanescent or non-propagating fields that exist within the couple of nanometers from the surface. The evanescent field contains high frequency spatial information of the surface and decays exponentially with distance from the surface. The basic principle of NSOM is based on having a sub-wavelength aperture ( $\approx 50$  nm) at the fiber tip apex and bringing the near-

field probe significantly closer ( $\approx 10$  nm) to the surface of interest. Thus, the illumination of the sample can be done within the near field of the light source. In that case the size of the features which can be imaged is limited primarily by the size of the aperture and not the wavelength of the light<sup>108</sup> (figure 5-1). Therefore, it overcomes the diffraction limit of traditional microscopy and achieves a higher resolution ( $>100$  nm).

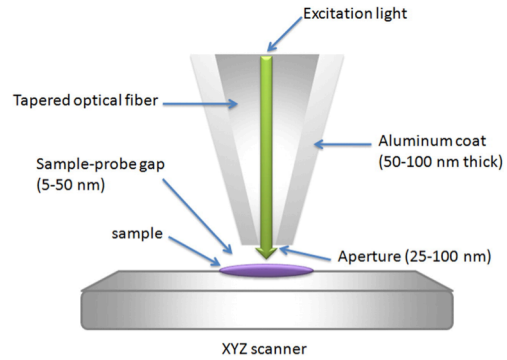


**Figure 5-1: Schematic drawing of an aperture near field scanning optical microscope. A typical microscope has an Al-Cr coated optical fiber with an aperture of 25 to 100 nm diameter at the point to generate a sub-wavelength light source used as the scanning probe. The probe will scan at a height of a few nanometers above the sample surface.**

Carrying out lateral scanning of the NSOM probe over the surface with either constant tip-sample separation or regulated distance using feedback mechanism one could attain the sub-wavelength resolution optical image which is correlated with the topography.

We are using the commercial NSOM, Nanonics Multiview 4000<sup>TM</sup> that could adapt up to four probes, each of which can image independently. Our NSOM setup (shown in figure 5-2) is supplied by two

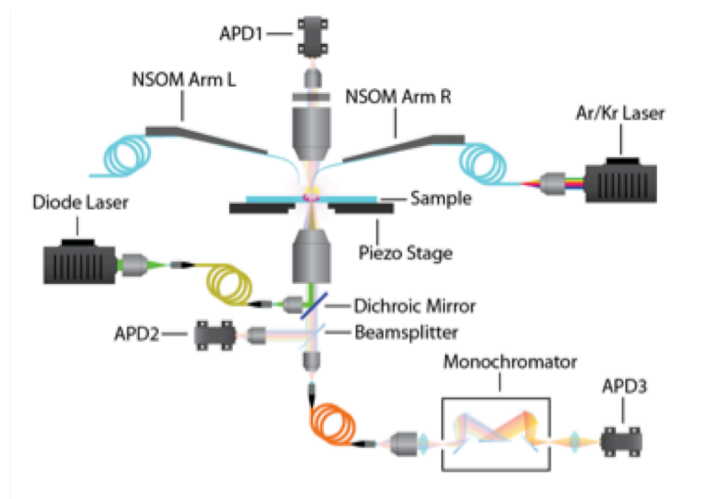


**Figure 5-2: Dual probe NSOM combined with upright and inverted optical microscope for multidimensional imaging in sub-wavelength scale.**

scanning probes and is combined by upright Nikon optical microscope and home-built inverted microscope. This allows us to combine topography with a variety of optical probes to investigate molecular packing structure, exciton dynamics, and physics of material interface in sub-wavelength scale.<sup>109-111</sup>

Using polarized near-field absorption probes, Kuehn and coworkers investigated local aggregated domains of thiophene oligomers by scanning a white-light NSOM probe over a semitransparent sample and collected the transmitted light in wide-field detected with an imaging spectrometer. Figure 5-3 shows the resulting NSOM image capturing the characteristic vibronic structure in the aggregate absorption with a spatial resolution of 75 nm. Additional polarized measurements provided insight into orientation of crystalline domains.<sup>112</sup>

Using a slightly different approach, I have inspected near-field absorption properties of P3HT films, using confocal-detected Rayleigh scattering from near-field excitation at 532 nm. Here we detect the attenuation in the far-field scattering signal at the NSOM probe wavelength. As shown in figure 5.4, because the absorption cross-section at 532 nm for amorphous P3HT is approximately an order of magnitude smaller than that of aggregated P3HT, confocal detected Rayleigh

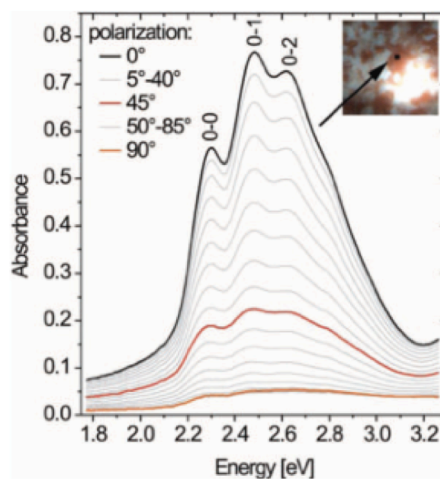


**Figure 5-3: NSOM absorption image and the corresponding spatially resolved transmission spectra from oligo thiophene film. The X-Y scale of the image shown in the inset is 6x6  $\mu\text{m}$  (Printed from ref. 112).**



scattering gives a very high contrast between amorphous and crystalline domains, as well as very strong extinction for crystalline nanostructures.<sup>113</sup>

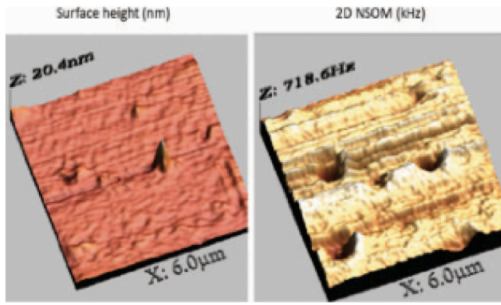


**Figure 5-4: (Left) surface height image of annealed P3HT thin film; (right) NSOM image of same region by confocal- detected Rayleigh scattering at 52 nm. The dips indicate absorption by crystalline domains.**

In addition to thin film, two different solutions of self-assembly P3HT nanofibers have been studied (Figure 5.5, left). Comparing their topography and NSOM images indicates a large attenuation of

relative backscattered intensity. Nanofibers' large absorption cross-section at 532 nm manifests homogeneous, high crystalline molecular structure of these nanofibers. It is worth to mention that correlating nanofibers' optical amplitude changes as a function of their height (figure 5-5, right (a)) reveals two different behaviors. Nanofibers of sample

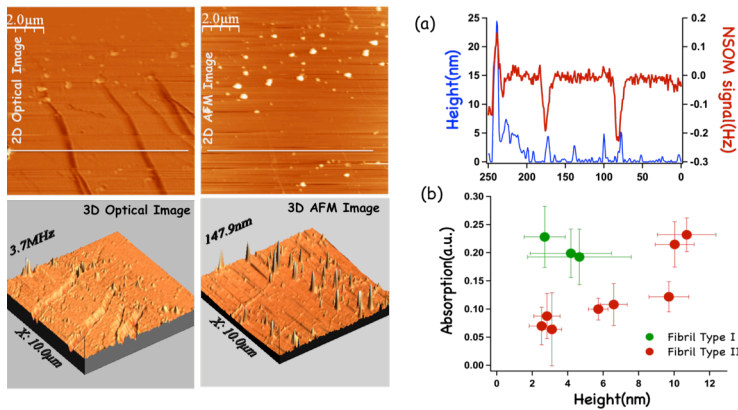


**Figure 5-5: Left: 2D and 3D topography and optical images of P3HT nanofibers cast on glass. Right: (a) Line profile topography and corresponding backscattered signal of the line shown in 2D images. The dips in the NSOM trace correspond to the absorption by the fibrils. (b) Correlation plot of the P3HT nanofiber absorption versus their height.**

two have almost the same average height, but nanofibers in sample one have different average height (figure 5-5, right (b)). Moreover, the absorption of nanofibers in sample one increases with height while nanofibers in sample two

show a weak inverse correlation between height and absorption. These effects could be related to different stacking orientations and internal structures of the nanofibers in two samples. Although more careful experiments are required to investigate the origin of the observed performance, the current preliminary results proves the idea of measuring single nanofiber absorption cross-section by detecting the attenuation of backscattered laser light.

Using this neat technique, we are going to run NSOM on individual pristine cross-linked nanofibers on glass and cross-linked nanofibers blend with P3HT amorphous. The combination of topography correlated backscattered light attenuation, wavelength and time resolved polarization would give us a better insight into the internal structure of both cross-linked families. Blending robust crystalline P3ST cross-linked nanofibers and amorphous P3HT chains creates gross amorphous /crystalline interface. Therefore, these complete simultaneous sets of measurements on the blend will provide the opportunity to investigate the exciton generation and migration hypothesis. The current studies suggest that exciton generation occurs in the high-energy sides and migrates to the lower energy regions and polaron recombination behavior that mostly happens in the boundaries.

Utilizing dual probe scans, we are also planning to do some high-resolution photocurrent measurements, in which one probe is used to collect topography information while the second one illuminates the specimen in near field. The interesting target to us for this measurement is a cross-linked nanofiber cast on reduced graphene oxide. The work function of r-GO<sup>92</sup> is located within the P3HT band gap,<sup>114</sup> which implies that it can hybridize with P3HT resulting in charge transfer complex formation. It also increases the charge mobility of P3HT by 20 times in hybrid field effect transistors.<sup>115</sup> By applying an

electromagnetic field, we are going to investigate the cross-linked nf/graphene interface to identify possible changes in the graphene work function and the charge transfer rate.

## REFERENCES

1. Kim, Y., et al., *A strong regioregularity effect in self-organizing conjugated polymer films and high-efficiency polythiophene:fullerene solar cells*. *Nat Mater*, 2006. **5**(3): p. 197-203.
2. Hou, J., et al., *An Easy and Effective Method To Modulate Molecular Energy Level of Poly(3-alkylthiophene) for High-Voc Polymer Solar Cells*. *Macromolecules*, 2009. **42**(23): p. 9217-9219.
3. Köhler, A., J.S. Wilson, and R.H. Friend, *Fluorescence and Phosphorescence in Organic Materials*. *Advanced Materials*, 2002. **14**(10): p. 701-707.
4. Sirringhaus, H., N. Tessler, and R.H. Friend, *Integrated Optoelectronic Devices Based on Conjugated Polymers*. *Science*, 1998. **280**(5370): p. 1741-1744.
5. Carpi, F. and D. De Rossi, *Colours from electroactive polymers: Electrochromic, electroluminescent and laser devices based on organic materials*. *Optics & Laser Technology*, 2006. **38**(4-6): p. 292-305.
6. Na, S.-I., et al., *Fully spray-coated ITO-free organic solar cells for low-cost power generation*. *Solar Energy Materials and Solar Cells*, 2010. **94**(8): p. 1333-1337.
7. Muller, C.D., et al., *Multi-colour organic light-emitting displays by solution processing*. *Nature*, 2003. **421**(6925): p. 829-833.
8. Jørgensen, M., et al., *Stability of Polymer Solar Cells*. *Advanced Materials*, 2012. **24**(5): p. 580-612.

9. Scholes, G.D. and G. Rumbles, *Excitons in nanoscale systems*. Nat Mater, 2006. **5**(9): p. 683-696.
10. Shen, X., V.V. Duzhko, and T.P. Russell, *A Study on the Correlation Between Structure and Hole Transport in Semi-Crystalline Regioregular P3HT*. Advanced Energy Materials, 2013. **3**(2): p. 263-270.
11. O'Carroll, D.M., et al., *Conjugated polymer-based photonic nanostructures*. Polymer Chemistry, 2013. **4**(20): p. 5181-5196.
12. Frenkel, J., *On the Transformation of light into Heat in Solids. I*. Physical Review, 1931. **37**(1): p. 17-44.
13. Liang, W.Y., *Excitons*. Physics Education, 1970. **5**(4): p. 226.
14. Wannier, G.H., *The Structure of Electronic Excitation Levels in Insulating Crystals*. Physical Review, 1937. **52**(3): p. 191-197.
15. Clark, J. and G. Lanzani, *Organic photonics for communications*. Nat Photon, 2010. **4**(7): p. 438-446.
16. Virgili, T., et al., *Ultrafast Intrachain Photoexcitation of Polymeric Semiconductors*. Physical Review Letters, 2005. **94**(11): p. 117402.
17. Hendry, E., et al., *Interchain effects in the ultrafast photophysics of a semiconducting polymer: spectroscopy of thin films and isolated chains in solution*. Physical Review B, 2005. **71**(12): p. 125201.
18. Spano, F.C., *The Spectral Signatures of Frenkel Polarons in H- and J-Aggregates*. Accounts of Chemical Research, 2009. **43**(3): p. 429-439.
19. Mukamel, S., *Principles of Nonlinear Optical Spectroscopy*. Oxford Series on Optical and Imaging Sciences. 1999: Oxford university press.

20. Kasha, M., *Energy Transfer Mechanisms and the Molecular Exciton Model for Molecular Aggregates*. Radiation Research, 2012. **178**(2): p. AV27-AV34.
21. Sariciftci, e.b.N.S., *Primary Photoexcitations in Conjugated Polymers: Molecular Exciton Versus Semiconductor Band Model* 1997.
22. Yamagata, H. and F.C. Spano, *Vibronic coupling in quantum wires: Applications to polydiacetylene*. The Journal of Chemical Physics, 2011. **135**(5): p. -.
23. Spano, F.C., *Excitons in conjugated oligomer aggregates, films, and crystals*. Annual Review of Physical Chemistry, 2006. **57**: p. 217-243.
24. Yamagata, H. and F.C. Spano, *Interplay between intrachain and interchain interactions in semiconducting polymer assemblies: The HJ-aggregate model*. Journal of Chemical Physics, 2012. **136**(18).
25. Philpott, M.R., *Theory of the Coupling of Electronic and Vibrational Excitations in Molecular Crystals and Helical Polymers*. The Journal of Chemical Physics, 1971. **55**(5): p. 2039-2054.
26. Spano, F.C., *Modeling disorder in polymer aggregates: The optical spectroscopy of regioregular poly(3-hexylthiophene) thin films (vol 122, art no 234701, 2005)*. Journal of Chemical Physics, 2005. **126**(15).
27. Spano, F.C., *Absorption in regio-regular poly(3-hexyl)thiophene thin films: Fermi resonances, interband coupling and disorder*. Chemical Physics, 2006. **325**(1): p. 22-35.
28. Noone, K.M., et al., *Photoinduced Charge Transfer and Polaron Dynamics in Polymer and Hybrid Photovoltaic Thin Films: Organic vs Inorganic Acceptors*. Journal of Physical Chemistry C, 2011. **115**(49): p. 24403-24410.

29. Paquin, F., et al., *Charge Separation in Semicrystalline Polymeric Semiconductors by Photoexcitation: Is the Mechanism Intrinsic or Extrinsic?* Physical Review Letters, 2011. **106**(19): p. 197401.
30. Cowan, S.R., et al., *Charge Formation, Recombination, and Sweep-Out Dynamics in Organic Solar Cells.* Advanced Functional Materials, 2012. **22**(6): p. 1116-1128.
31. Seoul, C. and N.-H. Kim, *Polymer light-emitting diodes based on poly(3-hexyl thiophene).* Fibers and Polymers, 2000. **1**(1): p. 25-31.
32. Tanase, C., et al., *Unification of the Hole Transport in Polymeric Field-Effect Transistors and Light-Emitting Diodes.* Physical Review Letters, 2003. **91**(21): p. 216601.
33. Chong, L.-W., et al., *Hole-injection enhancement of top-emissive polymer light-emitting diodes by P3HT/FNAB modification of Ag anode.* Organic Electronics, 2009. **10**(6): p. 1141-1145.
34. Sirringhaus, H., et al., *Two-dimensional charge transport in self-organized, high-mobility conjugated polymers.* Nature, 1999. **401**(6754): p. 685-688.
35. Sirringhaus, H., et al., *High-mobility conjugated polymer field-effect transistors,* in *Advances in Solid State Physics 39*, B. Kramer, Editor. 1999, Springer Berlin Heidelberg. p. 101-110.
36. Chou, C.-C., et al., *Morphology and Field-Effect Transistor Characteristics of Electrospun Nanofibers Prepared From Crystalline Poly(3-hexylthiophene) and Polyacrylate Blends.* Macromolecular Chemistry and Physics, 2013. **214**(7): p. 751-760.

37. Liu, J., R.S. Loewe, and R.D. McCullough, *Employing MALDI-MS on Poly(alkylthiophenes): Analysis of Molecular Weights, Molecular Weight Distributions, End-Group Structures, and End-Group Modifications*. *Macromolecules*, 1999. **32**(18): p. 5777-5785.
38. Yang, H., et al., *Structural transitions of nanocrystalline domains in regioregular poly(3-hexyl thiophene) thin films*. *Journal of Polymer Science Part B: Polymer Physics*, 2007. **45**(11): p. 1303-1312.
39. Brown, P.J., et al., *Effect of interchain interactions on the absorption and emission of poly(3-hexylthiophene)*. *Physical Review B*, 2003. **67**(6).
40. Shrotriya, V., et al., *Absorption spectra modification in poly(3-hexylthiophene):methanofullerene blend thin films*. *Chemical Physics Letters*, 2005. **411**(1-3): p. 138-143.
41. Park, Y.D., et al., *Solubility-Induced Ordered Polythiophene Precursors for High-Performance Organic Thin-Film Transistors*. *Advanced Functional Materials*, 2009. **19**(8): p. 1200-1206.
42. Wu, Z.Y., et al., *Temperature and Molecular Weight Dependent Hierarchical Equilibrium Structures in Semiconducting Poly(3-hexylthiophene)*. *Macromolecules*, 2010. **43**(10): p. 4646-4653.
43. Morfa, A.J., et al., *Optical characterization of pristine poly(3-hexyl thiophene) films*. *Journal of Polymer Science Part B: Polymer Physics*, 2011. **49**(3): p. 186-194.



44. Brinkmann, M., *Structure and morphology control in thin films of regioregular poly(3-hexylthiophene)*. Journal of Polymer Science Part B: Polymer Physics, 2011. **49**(17): p. 1218-1233.
45. Reid, O.G., et al., *The influence of solid-state microstructure on the origin and yield of long-lived photogenerated charge in neat semiconducting polymers*. Journal of Polymer Science Part B: Polymer Physics, 2012. **50**(1): p. 27-37.
46. Yu, Z., et al., *Self-assembly of two-dimensional nanostructures of linear regioregular poly(3-hexylthiophene)*. RSC Advances, 2012. **2**(1): p. 338-343.
47. Scharsich, C., et al., *Control of aggregate formation in poly(3-hexylthiophene) by solvent, molecular weight, and synthetic method*. Journal of Polymer Science Part B: Polymer Physics, 2012. **50**(6): p. 442-453.
48. Kim, D.H., et al., *Single-crystal polythiophene microwires grown by self-assembly*. Advanced Materials, 2006. **18**(6): p. 719- 723.
49. Yasutani, Y., et al., *Unprecedented High Local Charge-carrier Mobility in P3HT Revealed by Direct and Alternating Current Methods*. Chemistry Letters, 2013. **42**(1): p. 19-21.
50. Jiang, X.M., et al., *Spectroscopic studies of photoexcitations in regioregular and regiorandom polythiophene films*. Advanced Functional Materials, 2002. **12**(9): p. 587-597.
51. Ruseckas, A., et al., *Intra- and interchain luminescence in amorphous and semicrystalline films of phenyl-substituted polythiophene*. Journal of Physical Chemistry B, 2001. **105**(32): p. 7624-7631.

52. Labastide, J.A., et al., *Time- and Polarization-Resolved Photoluminescence of Individual Semicrystalline Polythiophene (P3HT) Nanoparticles*. Journal of Physical Chemistry Letters, 2011. **2**(17): p. 2089-2093.
53. Baghgar, M., et al., *Probing Inter- and Intrachain Exciton Coupling in Isolated Poly(3-hexylthiophene) Nanofibers: Effect of Solvation and Regioregularity*. Journal of Physical Chemistry Letters, 2012. **3**(12): p. 1674-1679.
54. Martin, T.P., et al., *Packing Dependent Electronic Coupling in Single Poly(3-hexylthiophene) H- and J-Aggregate Nanofibers*. Journal of Physical Chemistry B, 2013. **117**(16): p. 4478-4487.
55. Nagarjuna, G., et al., *Tuning Aggregation of Poly(3-hexylthiophene) within Nanoparticles*. Acs Nano, 2012. **6**(12): p. 10750-10758.
56. Niles, E.T., et al., *J-Aggregate Behavior in Poly-3-hexylthiophene Nanofibers*. Journal of Physical Chemistry Letters, 2012. **3**(2): p. 259-263.
57. Liu, J.H., et al., *Controlling Poly(3-hexylthiophene) Crystal Dimension: Nanowhiskers and Nanoribbons*. Macromolecules, 2009. **42**(24): p. 9390-9393.
58. Weng On, Y., et al., *Molecular Aggregation States of Imogolite/P3HT Nanofiber Hybrid*. Journal of Physics: Conference Series, 2011. **272**(1): p. 012021.
59. Roehling, J.D., I. Arslan, and A.J. Moule, *Controlling microstructure in poly(3-hexylthiophene) nanofibers*. Journal of Materials Chemistry, 2012. **22**(6): p. 2498-2506.
60. Zhang, R., et al., *Nanostructure dependence of field-effect mobility in regioregular poly(3-hexylthiophene) thin film field effect transistors*. Journal of the American Chemical Society, 2006. **128**(11): p. 3480-3481.

61. Paquin, F., et al., *Two-dimensional spatial coherence of excitons in semicrystalline polymeric semiconductors: Effect of molecular weight*. Physical Review B, 2013. **88**(15): p. 155202 1-14.
62. Singh, K.A., et al., *Dependence of field-effect mobility and contact resistance on nanostructure in regioregular poly(3-hexylthiophene) thin film transistors*. Applied Physics Letters, 2008. **92**(26): p. 263303 1-3.
63. Lim, J.A., et al., *Polymer semiconductor crystals*. Materials Today, 2010. **13**(5): p. 14-24.
64. Brinkmann, M., *Structure and Morphology Control in Thin Films of Regioregular Poly(3-hexylthiophene)*. Journal of Polymer Science Part B-Polymer Physics, 2011. **49**(17): p. 1218-1233.
65. Mena-Osteritz, E., et al., *Two-dimensional crystals of poly(3-alkylthiophene)s: Direct visualization of polymer folds in submolecular resolution*. Angewandte Chemie-International Edition, 2000. **39**(15): p. 2680-2684.
66. Holdcroft, S., *Determination of molecular weights and Mark–Houwink constants for soluble electronically conducting polymers*. Journal of Polymer Science Part B: Polymer Physics, 1991. **29**(13): p. 1585-1588.
67. Labastide, J.A., et al., *Time- and Polarization-Resolved Photoluminescence Decay from Isolated Polythiophene (P3HT) Nanofibers*. Journal of Physical Chemistry C, 2012. **116**(44): p. 23803-23811.
68. Spano, F.C., *The Spectral Signatures of Frenkel Polarons in H- and J-Aggregates*. Accounts of Chemical Research, 2010. **43**(3): p. 429-439.

69. Clark, J., et al., *Role of intermolecular coupling in the photophysics of disordered organic semiconductors: Aggregate emission in regioregular polythiophene*. Physical Review Letters, 2007. **98**(20).
70. Stranks, S.D., et al., *Nanoengineering Coaxial Carbon Nanotube-Dual-Polymer Heterostructures*. Acs Nano, 2012. **6**(7): p. 6058-6066.
71. Ferreira, B., et al., *Excited-State Dynamics and Self-Organization of Poly(3-hexylthiophene) (P3HT) in Solution and Thin Films*. Journal of Physical Chemistry B, 2012. **116**(8): p. 2347-2355.
72. Hammer, B.A.G., et al., *Cross-Linked Conjugated Polymer Fibrils: Robust Nanowires from Functional Polythiophene Diblock Copolymers*. Chemistry of Materials, 2011. **23**(18): p. 4250-4256.
73. Wu, F.I., et al., *Synthesis and characterization of spiro-linked poly(terfluorene): a blue-emitting polymer with controlled conjugated length*. Journal of Materials Chemistry, 2002. **12**(10): p. 2893-2897.
74. Miyanishi, S., K. Tajima, and K. Hashimoto, *Morphological Stabilization of Polymer Photovoltaic Cells by Using Cross-Linkable Poly(3-(5-hexenyl)thiophene)*. Macromolecules, 2009. **42**(5): p. 1610-1618.
75. Kim, H.J., et al., *Solvent-Resistant Organic Transistors and Thermally Stable Organic Photovoltaics Based on Cross-linkable Conjugated Polymers*. Chemistry of Materials, 2011. **24**(1): p. 215-221.
76. Kim, F.S. and S.A. Jenekhe, *Charge Transport in Poly(3-butylthiophene) Nanowires and Their Nanocomposites with an Insulating Polymer*. Macromolecules, 2012. **45**(18): p. 7514-7519.

77. Kim, K., et al., *Nanoscale optical and photoresponsive electrical properties of P3HT and PCBM composite nanowires*. *Organic Electronics*, 2011. **12**(10): p. 1695-1700.
78. Gao, J., et al., *Encapsulation of Poly(3-hexylthiophene) J-Aggregate Nanofibers with an Amphiphilic Block Copolymer*. *Langmuir*, 2012. **28**(47): p. 16401-16407.
79. Parkinson, P., et al., *Role of Ultrafast Torsional Relaxation in the Emission from Polythiophene Aggregates*. *Journal of Physical Chemistry Letters*, 2010. **1**(19): p. 2788-2792.
80. Banerji, N., et al., *Ultrafast Relaxation of the Poly(3-hexylthiophene) Emission Spectrum*. *Journal of Physical Chemistry C*, 2011. **115**(19): p. 9726-9739.
81. Scharber, M.C., et al., *Design Rules for Donors in Bulk-Heterojunction Solar Cells—Towards 10 % Energy-Conversion Efficiency*. *Advanced Materials*, 2006. **18**(6): p. 789-794.
82. Davis, R.J., et al., *Determination of energy level alignment at interfaces of hybrid and organic solar cells under ambient environment*. *Journal of Materials Chemistry*, 2011. **21**(6): p. 1721-1729.
83. Chirvase, D., et al., *Electrical and optical design and characterisation of regioregular poly(3-hexylthiophene-2,5diyl)/fullerene-based heterojunction polymer solar cells*. *Synthetic Metals*, 2003. **138**(1–2): p. 299-304.
84. Valaski, R., et al., *Charge injection and transport in electrochemical films of poly(3-hexylthiophene)*. *Journal of Applied Physics*, 2002. **92**(4): p. 2035-2040.

85. Onoda, M., et al., *Photoinduced charge separation in photovoltaic cell with heterojunction of p- and n-type conjugated polymers*. *Thin Solid Films*, 1998. **331**(1–2): p. 76-81.
86. Tsoi, W.C., et al., *Effect of Crystallization on the Electronic Energy Levels and Thin Film Morphology of P3HT:PCBM Blends*. *Macromolecules*, 2011. **44**(8): p. 2944-2952.
87. Wu, M.-C., et al., *Correlation between nanoscale surface potential and power conversion efficiency of P3HT/TiO<sub>2</sub> nanorod bulk heterojunction photovoltaic devices*. *Nanoscale*, 2010. **2**(8): p. 1448-1454.
88. Xu, T., et al., *Study of polymer/ZnO nanostructure interfaces by Kelvin probe force microscopy*. *Solar Energy Materials and Solar Cells*, 2013. **108**(0): p. 246-251.
89. Liscio, A., V. Palermo, and P. Samorì, *Probing Local Surface Potential of Quasi-One-Dimensional Systems: A KPFM Study of P3HT Nanofibers*. *Advanced Functional Materials*, 2008. **18**(6): p. 907-914.
90. Melitz, W., et al., *Kelvin probe force microscopy and its application*. *Surface Science Reports*, 2011. **66**(1): p. 1-27.
91. Zeng, T.-W., et al., *Kelvin Probe Force Microscopy study on hybrid P3HT:titanium dioxide nanorod materials*. *Chemical Physics Letters*, 2009. **479**(1–3): p. 105-108.
92. Liscio, A., et al., *Charge transport in graphene-polythiophene blends as studied by Kelvin Probe Force Microscopy and transistor characterization*. *Journal of Materials Chemistry*, 2011. **21**(9): p. 2924-2931.

93. Yates, B.W. and A.M. Duffy. *Statistical analysis of the metrological properties of float glass*. 2008.
94. Hu, Z., et al., *Single-Molecule Spectroscopy and AFM Morphology Studies of a Diblock Copolymer Consisting of Poly(3-hexylthiophene) and Fullerene*. *Macromolecular Chemistry and Physics*, 2010. **211**(22): p. 2416-2424.
95. Baghgar, M., et al., *Effect of Polymer Chain Folding on the Transition from H- to J-Aggregate Behavior in P3HT Nanofibers*. *The Journal of Physical Chemistry C*, 2014. **118**(4): p. 2229-2235.
96. Lan, Y.-K. and C.-I. Huang, *A Theoretical Study of the Charge Transfer Behavior of the Highly Regioregular Poly-3-hexylthiophene in the Ordered State*. *The Journal of Physical Chemistry B*, 2008. **112**(47): p. 14857-14862.
97. Samorí, P., et al., *Poly-para-phenylene-ethynylene assemblies for a potential molecular nanowire: an SFM study*. *Optical Materials*, 1998. **9**(1–4): p. 390-393.
98. Strassburg, E., A. Boag, and Y. Rosenwaks, *Reconstruction of electrostatic force microscopy images*. *Review of Scientific Instruments*, 2005. **76**(8): p. -.
99. Machleidt, T., et al., *Deconvolution of Kelvin probe force microscopy measurements—methodology and application*. *Measurement Science and Technology*, 2009. **20**(8): p. 084017.
100. Jie, X., et al., *Microscopic and macroscopic characterization of the charging effects in SiC/Si nanocrystals/SiC sandwiched structures*. *Nanotechnology*, 2014. **25**(5): p. 055703.
101. Yamagata, H., C.M. Pochas, and F.C. Spano, *Designing J- and H-Aggregates through Wave Function Overlap Engineering: Applications to Poly(3-*

- hexylthiophene*). The Journal of Physical Chemistry B, 2012. **116**(49): p. 14494-14503.
102. Ostrowski, D.P., et al., *The Effects of Aggregation on Electronic and Optical Properties of Oligothiophene Particles*. ACS Nano, 2012. **6**(6): p. 5507-5513.
103. Al-Ibrahim, M., et al., *Flexible large area polymer solar cells based on poly(3-hexylthiophene)/fullerene*. Solar Energy Materials and Solar Cells, 2005. **85**(1): p. 13-20.
104. Kim, J.B., et al., *Small-Molecule Thiophene-C60 Dyads As Compatibilizers in Inverted Polymer Solar Cells*. Chemistry of Materials, 2010. **22**(20): p. 5762-5773.
105. Pohl, D.W., W. Denk, and M. Lanz, *Optical Stethoscopy - Image Recording with Resolution  $\lambda/20$* . Applied Physics Letters, 1984. **44**(7): p. 651-653.
106. Harootunian, A., et al., *Near-Field Investigation of Submicrometer Apertures at Optical Wavelengths*. Journal of the Optical Society of America a-Optics Image Science and Vision, 1984. **1**(12): p. 1293-1293.
107. Betzig, E., et al., *Near-Field Scanning Optical Microscopy (Nsm) - Development and Biophysical Applications*. Biophysical Journal, 1986. **49**(1): p. 269-279.
108. Ohtsu, M. and H. Hori, *Near-field nano-optics: from basic principles to nano-fabrication and nano-photonics*. 1999: Plenum Pub Corp.
109. Wang, X., et al., *Probing the Nanoscale Phase Separation and Photophysics Properties of Low-Bandgap Polymer: Fullerene Blend Film by Near-Field Spectroscopic Mapping*. Small, 2011. **7**(19): p. 2793-2800.



110. Szymanski, C., et al., *Single molecule nanoparticles of the conjugated polymer MEH-PPV, preparation and characterization by near-field scanning optical microscopy*. Journal of Physical Chemistry B, 2005. **109**(18): p. 8543-8546.
111. Buratto, S.K., *Probing energy transfer in molecular semiconductor thin films on a nanometer scale using NSOM*. Abstracts of Papers of the American Chemical Society, 2004. **227**: p. U261-U261.
112. Kuehn, S., et al., *High-Resolution Near-Field Optical Investigation of Crystalline Domains in Oligomeric PQT-12 Thin Films*. Advanced Functional Materials, 2011. **21**(5): p. 860-868.
113. Barnes, M.D. and M. Baghar, *Optical probes of chain packing structure and exciton dynamics in polythiophene films, composites, and nanostructures*. Journal of Polymer Science Part B-Polymer Physics, 2012. **50**(15): p. 1121-1129.
114. Yu, D.S., et al., *Fullerene-Grafted Graphene for Efficient Bulk Heterojunction Polymer Photovoltaic Devices*. Journal of Physical Chemistry Letters, 2011. **2**(10): p. 1113-1118.
115. Huang, J., et al., *Polymeric semiconductor/graphene hybrid field-effect transistors*. Organic Electronics, 2011. **12**(9): p. 1471-1476.